UNIVERSITY OF OKLAHOMA

GRADUATE COLLEGE

Purification, Mechanism, and Biochemical Interactions of the Essential Mycolic Acid Transporters MmpL3 from *Mycobacterium tuberculosis,* and CmpL1 from *Corynebacterium glutamicum*.

A DISSERTATION

SUBMITTED TO THE GRADUATE FACULTY

in partial fulfillment of the requirements for the

Degree of

DOCTOR OF PHILOSOPHY

By

Casey Stevens

Norman, Oklahoma

2020

Purification, Mechanism, and Biochemical Interactions of the Essential Mycolic Acid Transporters MmpL3 from *Mycobacterium tuberculosis,* and CmpL1 from *Corynebacterium glutamicum*.

A DISSERTATION APPROVED FOR THE
DEPARTMENT OF CHEMISTRY AND BIOCHEMISTRY

BY THE COMMITTEE CONSISTING OF:

Dr. Helen Zgurskaya, Chair

Dr. Elizabeth Karr

Dr. Valentin Rybenkov

Dr. Robert Cichewicz

Dr. Christina Bourne

Abstract

Chapter 1: Introduction

1.1 – The Corynebacterium-Mycobacterium-Nocardia Family

1.2 – The CMN Family Cell Envelope is Unique Among Bacteria

1.3 – Mycolic Acid Synthesis and Transport

1.4 – MmpL3 As a Novel Therapeutic Target

Chapter 2: Methods

2.1 - Strains and growth conditions

2.2 - Protein purifications

2.3 - MIC assays

2.4 - SPR binding assays

2.5 - BLI binding assays

2.6 - Partial Proteolysis

2.7 - Silver Staining

2.8 – Protein Reconstitution into proteoliposomes and assays.

2.9 - Homology Modelling

Chapter 3: Purification and Functional Characterization of Mycolic Acid Transporters of *Corynebacterium glutamicum* and *Mycobacterium tuberculosis*.

3.1 Introduction

3.2 Results

3.2.1 - Purification of CmpL1

3.2.2 - Purification of MmpL3

3.2.3 – Reconstitution of CmpL1 and MmpL3 into proteoliposomes

3.2.4 – Interaction of AcTre67 with CmpL1 and MmpL3

Chapter 4: Direct interaction and Inhibition of mycolic acid transporters by small molecule compounds.

4.1 Introduction

4.2 Results

4.2.1 – *In Vivo* Activity of Mycolic Acid Inhibitors against CmpL1 and MmpL3.

4.2.2 - Direct Interaction of Inhibitors with Targets

4.2.3 - Inhibition of Proton Transport Activity

4.2.4 – Mechanism of Resistance to MmpL3 Inhibitors

4.2.5 – Conformational Change in MmpL3 (G253E)

Chapter 5: Participating partners, an initial exploration of the MmpL3 Interactome.

5.1 Introduction

5.2 Results

5.2.1 - Purification of suspected interacting partners

5.2.2 – Direct interaction of proteins with MmpL3

Chapter 6: Discussion

References

List of Tables

Table 4.1 - Minimum Inhibitory Concentrations (MIC) of MmpL3 inhibitors in *M. tuberculosis* and *C. glutamicum*.

Table 4.2. Kinetic profiles of compounds interacting with MmpL3 and CmpL1.

Table 4.3 – Resistance profiles of clinically isolated MmpL3 mutants

Table 5.1 – Proteins purified for assessment of interaction with MmpL3.

List of Figures

Figure 1 – Representation of a Gram-positive Cell Wall

Figure 2 - Representation of a Gram-negative Cell Wall

Figure 3 - Representation of a CMN Family Cell Envelope

Figure 4 - Structures of Mycobacterial Mycolic Acids

Figure 5 - Fatty Acid Synthesis (FAS) Pathway for Mycolic Acid Synthesis

Figure 6 - TMM Processing and Export Pathway

Figure 7 - Crystal structure of MmpL3

Figure 8 – Inhibitor binding site of MmpL3 and CmpL1

Figure 3.1 – Expression and Purification of corynebacterial CmpL1

Figure 3.2 – Expression and purification of MmpL3(*Mtb*) from *C. glutamicum*.

Figure 3.3 – Expression and Purification of MmpL3(*Mtb*) from *M. smegmatis*

Figure 3.4 –Representation of a Reconstituted Membrane Transporter.

Figure 3.5 – Protein recovery after reconstitution.

Figure 3.6 – Reconstituted mycolic acid transporter activity at different pH conditions

Figure 3.7 - Substrate analogs for Trehalose monomycolate (TMM)

Figure 3.8 – MmpL3 and CmpL1 proton translocation activity in the presence of a substrate analog AcTre67

Figure 3.9 – Rates of proton transport of MmpL3 and CmpL1 in the presence of a substrate AcTre67

Figure 3.10 - The effect of TMM analogs on the proton transport activity of transporters.

Figure 3.11 – Direct interaction of AcTre67 with MmpL3

Figure 4.1 – Published MmpL3 Inhibitors

Figure 4.2 - Novel indole-2-carboxamide Inhibitors

Figure 4.3 - Binding of MmpL3 inhibitors to MmpL3 and CmpL1

Figure 4.4 - Binding of novel IC compounds to transporters with selective *in vivo* activity against CmpL1

Figure 4.5 - Binding activity of structurally similar compounds to transporters

Figure 4.6- Differential proton transport inhibition in opposite protein orientations

Figure 4.7 - Dose dependent inhibition of proton translocating activities of MmpL3 and CmpL1.

Figure 4.8 – Point mutations in MmpL3 map to the Transmembrane Region

Figure 4.9 – Biolayer Interferometry sensorgrams of inhibitor

interaction with MmpL3 WT and G253E resistant mutant

Figure 4.10 – Proteolytic profiles of MmpL3 WT and G253E

Figure 5.1 - Purification of suspected MmpL3 interactors

Figure 5.2 – Binding interactions of the suspected MmpL3 Interactome

Abstract:

The Corynebacterium – Mycobacterium – Nocardia family (CMN family) are a subset group of actinomycetes which are characterized as acid-fast, Gram-positive species. Many members of the CMN family are causative agents of human disease with *M. tuberculosis*, *M. leprae, C. diptheria,* and *N. asteroides* historically being exceptionally hard to treat pathogens. One of the reasons the CMN family are resistant to treatment is also the defining trait of the family, which is the presence of an outer membrane with a unique composition of peptidoglycan crosslinked to an arabinogalactan matrix which is further crosslinked to mycolic acids forming an effective outer barrier.

This peptidoglycan – arabinogalactan – mycolic acid barrier forms the inner leaflet of the outer membrane, with loosely associated mycolic acids esterified to disaccharide trehalose sugars forming the outer leaflet of the outer membrane. Both of these structural features together form the 'myco-membrane' which is even further complicated by the presence of an outer capsular layer comprised mainly of extended sugar polymers and proteins which are thought to be involved in regulating the hosts' immune response.

The proper biosynthesis of the myco-membrane is essential for the viability of CMN family pathogens, and the unique physiology of the myco-membrane has made it a primary target for pharmacological therapeutics. In addition to targeting peptidoglycan, the treatment of CMN family pathogens can also include the disruption of arabinogalactan polymerization and the synthesis of fatty acids used in the construction of the more complicated mycolic acids.

Mycolic acids are long-chain saturated fatty acids unique to the CMN family and are found exclusively in the outer myco-membrane. Significant efforts have gone into documenting the biosynthetic pathway of mycolic acid, where it was revealed that the catalytic steps necessary to form these long-chain fatty acids are completed inside the bacterial cell.

This raised the question of how these mycolic acids cross the cell membrane in order to be incorporated in the outer membrane. In *M. tuberculosis* it was shown that mycolic acids could not translocate to the outer leaflet of the inner membrane without the function of the essential membrane transporter MmpL3. The role of MmpL3 as a mycolic acid transporter has since been validated, and MmpL3 has been pursued as a novel pharmacological target. Despite the significance of this discovery, the exact mechanism by which MmpL3 transports mycolic acids across the cell membrane had not yet been described.

The focus of this thesis is on the mechanistic function of the essential mycolic acid membrane transporters CmpL1 from *C. glutamicum* and MmpL3 from *M. tuberculosis*, their interactions with inhibitors, and the discovery of novel protein-MmpL3 interactions. To begin our study, we undertook the purification of MmpL3 from *M. tuberculosis* and CmpL1 from *C. glutamicum*, and reconstituted them into functional proteoliposomes. Our results from this experiment demonstrate that the mycolic acid transporters facilitate H^+ flux across the membrane which is stimulated in the presence of a substrate analog.

As MmpL3 is a significant therapeutic target, several MmpL3 inhibitors have been developed and are in clinical trials. Therefore, we next moved to determine whether these inhibitors directly interact with MmpL3, and if they carry out their function through the inhibition of the observed H^+ transport. We utilized a Surface Plasmon Resonance (SPR) assay to successfully determine the direct interaction of a variety of pharmacophores, and we report the kinetic rates of the interactions. Continuing the study of mycolic acid transport inhibition, we pursued a set of novel indole-2-carboxamide (IC) compounds which had both direct interaction and good activity in minimum inhibitory concentration (MIC) assays against *M. tuberculosis* MmpL3 and *C. glutamicum* CmpL1. We utilized these IC inhibitors in the proteoliposome assays and report our

results that the inhibition of mycolic acid transport is due to the inhibition of H^+ flux across the membrane.

MmpL3 carries out the essential function of transporting mycolic acids across the plasma membrane of the bacterial cell. For proper cell wall biogenesis, the timing and incorporation of mycolic acid into the nascent cell wall would need to be coordinated with other biosynthetic machinery. We hypothesized that there would need to be other proteins associated to MmpL3. To test this hypothesis, we identified potential protein interactions via a bacterial two-hybrid screen of the entire *Mtb* proteome with MmpL3. Potential interacting proteins were independently purified and assayed for direct interaction with MmpL3 using SPR, and we report our results confirming high affinity interactions with several proteins. This significant result provided the first description of the MmpL3 interactome.

CHAPTER 1: INTRODUCTION

This chapter introduces the Corynebacterium-Mycobacterium-Nocardia (CMN) family of human pathogens, and the difficulty of treating infections caused by this family in the context of their unique outer membrane when compared to other bacterial membranes.

1.1 – The Corynebacterium-Mycobacterium-Nocardia Family

The actinomycetes are a large and diverse phylum of Gram-positive prokaryote species which can be either aquatic or terrestrial[1]. Contained in this phylum are species which stain acid-fast due to the presence of a complex outer membrane comprised of peptidoglycan – arabinogalactan – and mycolic acids[2]. Members which contain this conserved unique structural feature are the Corynebacterium, Mycobacterium, and Nocardia species and thus are grouped into the Corynebacterium-Mycobacterium-Nocardia (CMN) Family[3].

Mycobacterium tuberculosis (*Mtb*) is the leading source for infectious disease worldwide, with an estimated one-third of the global population carrying the tuberculosis causing pathogen[4]. *M. tuberculosis* is an aerobic rod-shaped and acid-fast Gram-positive bacterium, and infection with *Mtb* predominately occurs due to inhalation of aerosolized droplets in the air which have been expelled from an afflicted patient [5]. Although infection can occur in other bodily tissues, most *Mtb* infections occur in the lungs are diagnosed with the characteristic presentation of granuloma formation[6,7]. Granuloma formation begins during infection, as *Mtb* bacilli which are phagocytosed by macrophages prevent lysosomal fusion to the encapsulating phagosome[8-10]; proliferating inside the phagosome until escaping into the macrophage[10]. Once free inside the macrophage *Mtb* secretes tuberculosis necrotizing toxin (TNT) which induces necroptosis by way of NAD^+ hydrolysis, effecting the bacilli's

escape[11]. During this process, uninfected host macrophages and dendritic cells surround the infected macrophages and are stimulated by CD4 T-helper cells [12] creating a ball around the infecting bacteria which forms the resultant granuloma [13]. In the majority of cases granuloma formation is stable and patients can be asymptomatic for decades; for reasons still not fully understood, approximately ten percent of these 'latent' TB infections become active TB disease and present with the full suite of symptoms [14,15]. Approximately 50% of active MDR-TB cases result in patient mortality[4].

M. tuberculosis is the most well-known and studied species from the CMN family, however there are many significant human pathogens belonging to this group. *Mycobacterium leprae* is the causative agent for leprosy, a slow-growing infection of the skin, nerves, eyes, and extremities [16]. Nervous system infection of *M. leprae* results in the complete loss of sensation of the affected nerves, which further leads to extremity loss due to unfelt injuries and infections[17]. *M. leprae* is among the slowest growing pathogens in the CMN family, with symptoms commonly not presenting until a year post infection, and some patients not developing symptoms for twenty or more years [18]. *Mycobacterium kansasii* and *Mycobacterium abscessus* are both considered Non-Tubercular Mycobacterial (NTM) infections, can establish infection in any bodily organ, and are extensively resistant to antibiotics and disinfectants[19,20]. These traits have led to an increase in nosocomial infections in immunocompromised patients, and currently NTM are considered an emerging threat [21].

Nocardia asteroides (among other Nocardia species) afflicts the host with nocardiosis, an infection typically affecting the lungs and skin, however once the infection is established and without proper care, the infection disseminates and can spread to the brain and spinal cord [22]. Once the neural tissue becomes infected, brain abscesses form and patient mortality rises to approximately 38% which additionally increases to over 60% in immunocompromised patients[23,24].

Corynebacterium diphtheria is the disease-causing agent of diphtheria, an infection that begins in the throat before going on to induce myocarditis, nerve paralysis, and excessive bleeding through the production of diphtheria toxin in infected patients [25]. Diphtheria, even with proper medical care has a high morbidity rate of up to 17% , prompting the development of a diphtheria vaccine[26] which is highly effective against *C. diphtheria*; however, recently *Corynebacterium ulcerans* has been shown to also produce diphtheria toxin in human infections making it another reservoir of human disease[3,27]. The disease burden created by members of the CMN family is extreme[28], with most requiring twelve month or longer combination therapy to clear the infections, to variable success rates[29].

1.2 – The CMN Family Cell Envelope is Unique Among Bacteria.

The bacterial cell wall is a defining phenotype of different species and functions as the first line of defense against environmental fluctuations and antibacterial compounds[30]. The principle taxonomic technique for the identification of bacterial species is the Gram stain [31], in which the bacterial population under test is separated into two groups based on the ability to retain different dyes. In a Gram-positive organism **(Figure 1)**, there is a thick layer (20-80 nm)[32] of peptidoglycan which readily retains the crystal violet principle dye of the Gram stain, whereas in a Gram-negative organism this crystal violet is not retained in the much thinner peptidoglycan (4-8 nm)[30,33] and is subsequently counterstained with a secondary dye. Peptidoglycan (PG) is a barrier formed on the outer surface of the cell consisting of sugars and short peptides. The main component of the PG cell wall is the long-chain alternating polymer of N-acetylglucosamine and N-acetylmuramic acid which runs along the long circumference of the cell[34]. These long sugar chains are then cross-linked via a transpeptidase reaction by short well-defined peptides [35], and once

the NAG-NAM polymer strands have been crosslinked this imparts strength and rigidity as multiple layers are stacked [36]. The second major component of the Gram-positive cell wall are the teichoic acids, which are polymer chains of either polyribitol phosphate or polyglycerol phosphate[37] and can be found anchored to either the N-acetylmuramic acid residues of the PG layer or to an integral plasma membrane lipid[38]. These teichoic acids impart significant negative charge to the cell wall and thus bind cations, and are involved in cation homeostasis among other, species dependent functions[39].

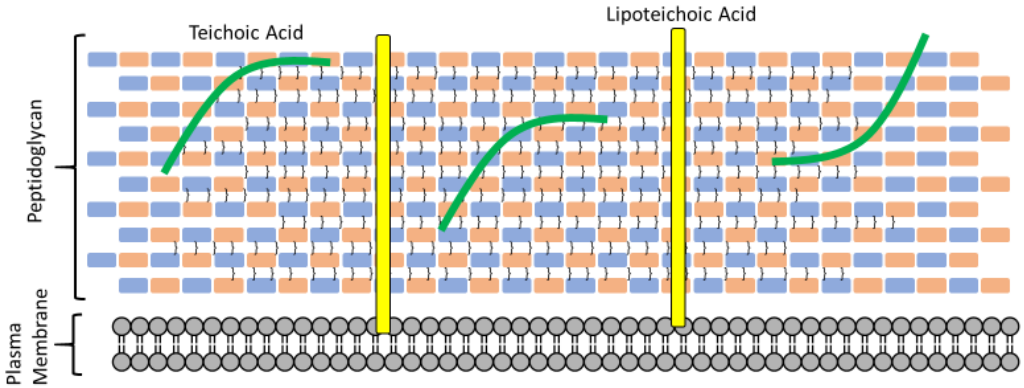

Figure 1 – Representation of a Gram-positive Cell Wall

Cartoon schematic of a Gram-positive bacterial cell wall. A thick peptidoglycan layer (Blue / Orange bricks) are crosslinked via a transpeptidase reaction (Black links) to impart rigidity. Teichoic acids (Green) and lipoteichoic acids (Yellow) provide structural support and negative ionic charge.

The Gram-negative cell wall **(Figure 2)** possesses a similar plasma membrane which is reinforced by a PG layer; however it is not as substantial with a thickness of approximately 10% of a Gram-positive species[33]. Instead the defining trait of a Gram-negative bacteria is the presence of an outer membrane which fully encapsulates the cell and partitions off a functional periplasm[40]. The Gram-negative outer membrane is asymmetric, with the inner leaflet consisting of phospholipids and the outer leaflet of the outer membrane composed of lipopolysaccharide (LPS)[41]. Proteins present in the outer membrane are predominately porins to facilitate nutrient uptake[42,43], or beta-barrel channels which function as components of the Resistance-Nodulation-Division (RND) class of tripartite efflux pump assemblies[44,45]. RND efflux pumps are tripartite complexes consisting of: the RND substrate:H^+ antiporter located spanning the plasma membrane, an outer membrane channel through which substrates are pumped out of the cell, and a membrane fusion protein which connects the RND pump to the outer membrane pore[46]. This tripartite assembly is unique to Gram-negative bacteria and functionally allows the active efflux of toxic compounds in the periplasm back out of the cell[47]. The combined effect of the outer membrane permeability barrier with the active efflux of drugs makes the Gram-negative bacteria much more resistant to therapeutic intervention as compared to Gram-positive species [48,49].

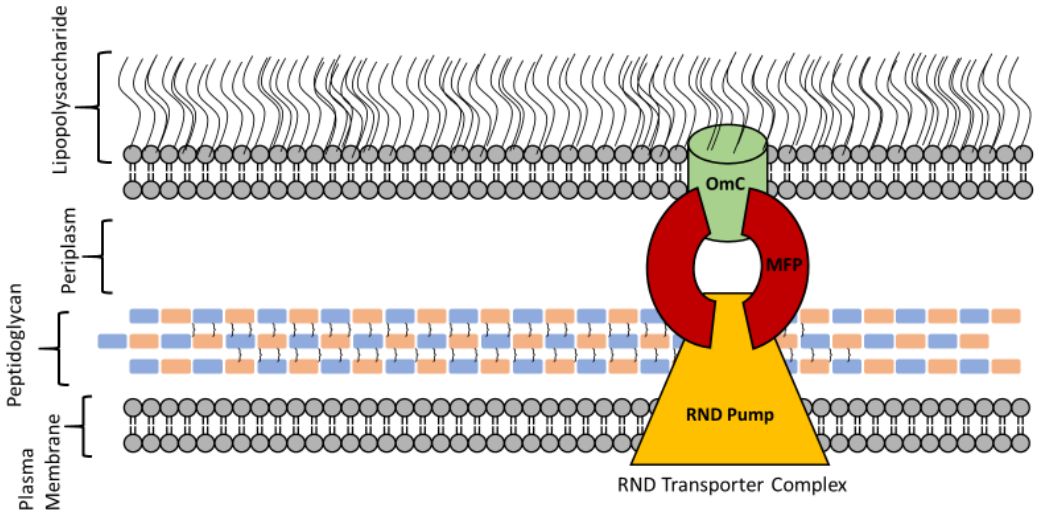

Figure 2 – Representation of a Gram-negative Cell Wall

A cartoon representation of a typical Gram-negative cell wall. A thinner layer of peptidoglycan (Blue / Orange bricks) is found as compared to Gram-positive bacteria. An asymmetric outer membrane encapsulates the cell, with the inner leaflet formed of phospholipids and the outer leaflet formed of lipopolysaccharide (Grey strands). Also illustrated is an assembled RND tripartite assembly, the RND pump (Gold) is connected to the Outer membrane Channel (Green) via a Membrane Fusion Protein (Red).

The CMN family are classified as acid-fast Gram-positive species, however they are unique in that they have an asymmetric outer membrane surrounding their peptidoglycan cell wall[50]. This structural feature, which is visualized under microscopy as a thick, waxy outer myco-membrane[51] is what characterizes these bacteria as some of the most difficult to treat pathogens. Due to its extremely hydrophobic nature it is thus impermeable to polar and ionic solutes, and has a significantly lower hit rate for the discovery of novel antibiotic compounds[45]. The myco-membrane origin starts at the cell membrane, covalently coupled to a layer of peptidoglycan which differs in significant ways from traditional Gram-positive pathogens[52] (**Figure 3**). PG from *M. tuberculosis* consists of alternating units N-

acetylmuramic acid and N-glycolylmuramic acid[53,54], and the presence of this glycolyl modification has been shown to increase resistance to lysozyme activity[55]. The peptide crosslinking in mycobacterial PG is also significantly more robust, with 20-30% [56] more observed crosslinks when compared to *E. coli* [57]. On the PG layer an alternating matrix of arabinose-galactose (AG) units are crosslinked[58] by the activity of the LytR-CpsA-Psr (LCP) family of proteins. In *C. glutamicum* LcpA and LcpB carry out this reaction with redundant activity, and the double knockdown presenting severe cell wall defects [59]. The *M. tuberculosis* analogs CpsA1 and CpsA2 were also shown to have overlapping activity, where double deletions were not able to generate viable cells [50], and the phosphotransferase Lcp1 also demonstrated the ability to attach AG to the PG matrix in cell-free assays [60].

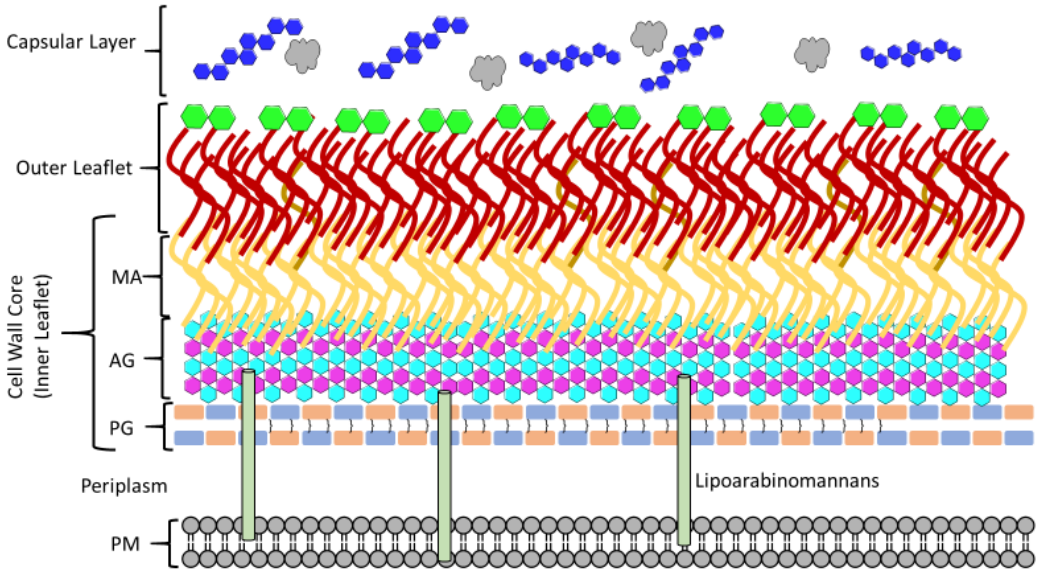

Figure 3 – Representation of a CMN Family Cell Envelope

Cartoon representation of a typical CMN family cell envelope. A periplasm is found exterior to the plasma membrane with the cell wall core tethered to plasma membrane by lipoarabinomannans (Green barrels), and consists of peptidoglycan (PG – Blue / Orange bricks) linked to

arabinogalactan (AG – Purple / Cyan hexagons) and covalently attached mycolic acids (Yellow lines). This forms the inner leaflet of the outer myco-membrane, with the outer leaflet formed of loosely associated mycolic acids (Green hexagons with Red lines). The external capsular layer consists primarily of glucans (Grey cloud) and arabinomannans (Blue hexagons).

To the distal arabinogalactan (AG) layer mycolic acids, long-chain saturated lipids, are esterified with the hydrophobic tails extending away from the cell forming the inner leaflet of the outer myco-membrane[61]. An asymmetric outer leaflet is composed of free trehalose mycolates, the main component being trehalose dimycolate (TDM)[62] (**Figure 4)**. TDM is formed from two molecules of trehalose monomycolate (TMM) by extracellular Antigen 85 (Ag85) enzymes catalyzing the transfer of one mycolic acid from one TMM onto the trehalose of a second TMM releasing a free trehalose disaccharide[63,64]. TMM, though a smaller component of the outer membranes outer leaflet, is the major building block of the outer myco-membrane; it is the source of the mycolic acids which are esterified to the arabinogalactan matrix as well as being consumed to form TDM in the outer leaflet of the outer membrane[62]. Curiously, this extremely large hydrophobic lipid is synthesized inside the cell and must then be transported across the cell membrane so it can be utilized in cell wall synthesis[65].

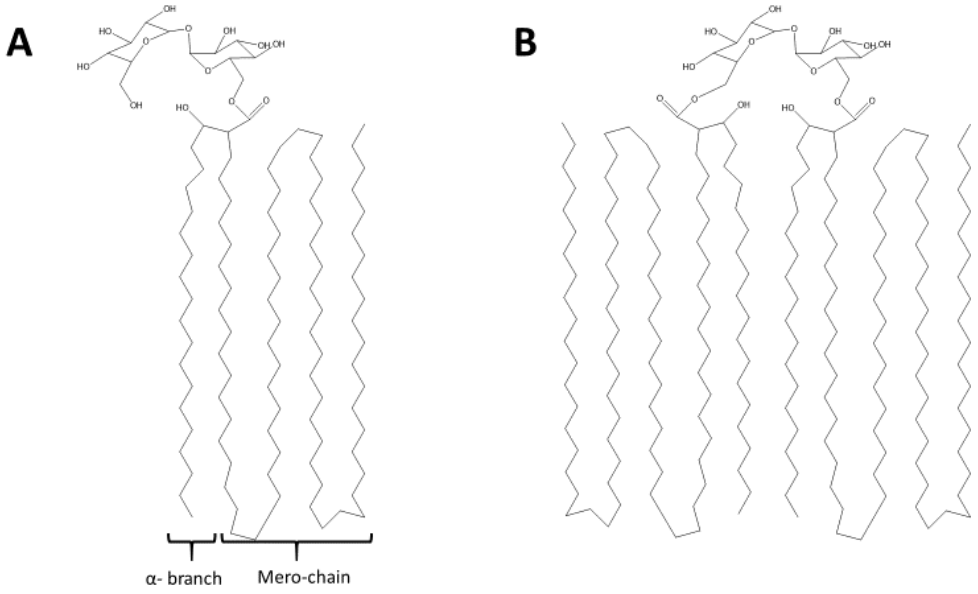

Figure 4 – Structures of Mycobacterial Mycolic Acids

A) Structure of Trehalose Mono-Mycolate (TMM) with indicated α- branch and mero-chain of the mature mycolate. **B)** Structure of Trehalose Dimycolate (TDM), with two mycolates coupled to one trehalose sugar.

Located distal to the outer leaflet of the outer myco-membrane is the loosely bound 'capsular layer' which is comprised mostly of sugars and proteins with the main components being α-D-glucan and arabinomannan[66,67]. This sugary capsule layer has been implicated in the regulation of the host immune response to infection, with the lipoarabinomannan being proposed as an immune system evasion mechanism via its ability to prevent phagolysosomal fusion [8]. The outer leaflet and capsular layer also contains many complex lipid species, phthiocerol dimycocerosates (PDIM), lipooligosaccharides (LOS), and phenolic glycolipids (PGL) which have all been shown to have roles in transmission or evasion [68,69]. In the extremely virulent clinical strain of *Mtb* HN878 [70], PGL overexpression led to the reduction of pro-inflammatory cytokines, whereas loss of PGL demonstrated a clear loss of virulence [71]. The abundance of LOS in the capsular layer affects hydrophobicity of the membrane, with less observed LOS in more evolved mycobacterial

species such as *Mtb* leading to an increased hydrophobic membrane and presumably increased aerosol infectivity [72]. PDIMs are major virulence factors in mycobacteria and have been implicated in a variety of functions. Early in establishing the infection, cell surface PDIMs recruit additional macrophages to the site of infection and shield the bacilli from the immune system by masking other pathogen associated molecular patterns (PAMPs) on the *Mtb* surface [73]. Shielded from the immune system, the PDIMs protect Mtb from reactive nitrogen species which would otherwise be released by the macrophage, and lower the host release of tumor necrosis factor (TNF-α) and interleukin 6 (IL-6) [74]. The permeability of the mycomembrane is also influenced by the presence of PDIMs, as mutants with impaired PDIM synthesis show increased uptake of the negatively-charged probe chenodeoxycholate, as well as increased susceptibility to sodium dodecyl sulfate (SDS) [75].

The low permeability of the myco-membrane would also seem to necessitate the use of porins or other outer membrane channels to assist in nutrient uptake, however very little is known about these postulated proteins. Recently, proteins of the proline-proline-glutamate family (PPE) have been identified in the outer membrane of *M. tuberculosis* which facilitate the acquisition of essential nutrients; PPE36 and PPE62 demonstrate the ability to bind heme and represent one of the pathways for iron acquisition by *M. tuberculosis*[76]. Additionally, deletion of PPE51 in *M. tuberculosis* has resulted in mutants unable to grow on propionamide, glycerol, and glucose indicating its involvement in the uptake of these small nutrients[77].

The most well-documented of mycobacterial porins, MspA from *M. smegmatis*, has a unique goblet shape wherein the large open ‘lip’ of the goblet is oriented away from the cell, and the ‘stem’ of the goblet bottlenecks down to a size exclusion limit of 28 Å [78-81]. This open pore size is more restrictive than that of other outer membrane pores from Gram-negative bacteria, like TolC[82,83] and FhuA[84-86] which have openings of 35

Å and 4.5 nm respectively . There is no known MspA homolog in *M. tuberculosis*, however it does contain one confirmed outer membrane porin, an OmpA-like outer membrane channel which has not been shown to be essential for growth[87], and whose role is still being investigated.

1.3 – Mycolic Acid Synthesis and Transport

As the namesake of the CMN family outer myco-membrane, mycolic acids have a unique and essential pathway for their biosynthesis and incorporation. The overall size of the mycolic acid tail depends on the species within the CMN family; corynebacteria possess the shortest tails of 22-36 total carbons, nocardia species containing 46-60 carbons, and mycobacteria exhibiting the longest tails of 60-90 carbons in length[88]. This extensive lipid tail is synthesized in two parts, an alpha branch of 24-26 carbons, and the mero-chain which varies from 48-62 carbons (**Figure 5**)[89]. In *M. tuberculosis*, mycolic acid biosynthesis begins with Rv2524, a fatty acid synthase I (FAS I) enzyme containing the seven catalytic domains necessary for 'eukaryotic-like' fatty acid synthesis[90]. Two different products result from the FAS I enzyme, a 24-26 carbon acyl chain which undergoes carboxylation by AccD4 forming the alpha mycolic branch[91], and a 16-18 carbon acyl tail which is fed into a FAS II system where the carbon tail is extended to 48-62 carbons. Initiation of the FAS II system requires the 16-18 carbon product of FAS I be activated by its addition to a malonyl group harbored by an acyl carrier protein (ACP)[92,93]. In contrast to the FAS I cycle, the FAS II system consists of discrete enzymes which catalyze each step of the elongation cycle: the activated acyl-ACP is reduced by MabA, which is then dehydrated by HadB and reduced by InhA, and then finally extended by two carbons via the addition of malonyl-ACP by KasA[94-97]. Once the nascent mero-chain reaches sufficient length elongation ceases and the mero-chain is activated by the transfer of an adenyl monophosphate (AMP) by Fad32[98], which then undergoes a

Claisen condensation with the carboxylated 24-26 carbon alpha branch via polyketide synthase 13 (pks13)[99,100] **(Figure 5)**.

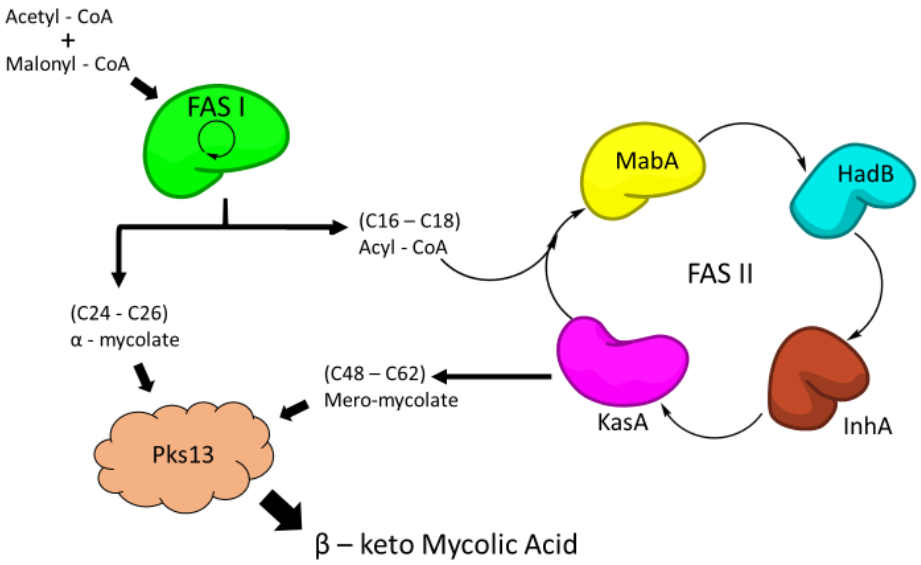

Figure 5 – Fatty Acid Synthesis (FAS) Pathway for Mycolic Acid Synthesis

Acetyl-CoA and Malonyl-CoA feed into the multi-domain FAS I (Green) and the nascent fatty acid undergoes multiple rounds of elongation. Two main products result from FAS I, the C24-C26 α-mycolate branch and a C16-C18 acyl chain which feeds into the multi-protein FAS II Complex. Elongation by catalytic cycles of MabA (Yellow), HadB (Cyan), InhA (Brown), and KasA (Pink) continue until the complete mero-mycolate chain is formed. Pks13 (Salmon) catalyzes a condensation of the α-mycolate and mero-mycolate to form the immature β-keto mycolic acid.

Trehalose-6-phosphate is also transferred by pks13 to the newly formed β-keto mycolic acid[101], which is then reduced by corynebacterial mycolate reductase A (CmrA) forming the mature trehalose mono-mycolate (TMM)[102,103]. Though in the final mature form, TMM has been shown to accumulate in the inner leaflet of the inner membrane unless the hydroxyl group on the mycolic motif is acetylated, which is carried out by

Trehalose mono-mycolate acetyl transferase (TmaT)[104]. Very recently a methyltransferase (MtrP) was discovered[105] in the same genetic locus as TmaT, which when deleted also causes the accumulation on TMM in the inner leaflet of the plasma membrane, and whose function is shown to be required for regulation of TmaT. Acetylation of TMM is then followed by the transport of the mycolic acid to the periplasmic face of the cell by way of the essential Mycobacterial membrane protein large 3 (MmpL3)[65,106-108] **(Figure 6)**.

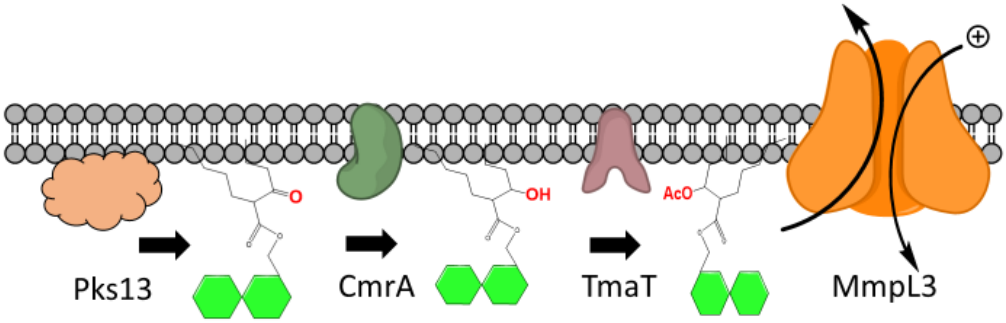

Figure 6 – TMM Processing and Export Pathway
The immature β-keto mycolic acid formed by Pks13 (Salmon) is reduced on the mycolic motif by CmrA (Dark Green) before being acetylated by TmaT (Rose) and then exported to the periplasm by MmpL3 (Orange).

Accumulation of TMM in the inner leaflet of the cytoplasmic membrane is also observed in cells where MmpL3 is depleted, indicating that the mycolic acid efflux is carried out only by MmpL3 which explains its essentiality[109]. Once in the periplasm, the mycolic acids must reach their site of incorporation on the distal ends of the arabinogalactan matrix, where the TMM is transferred to arabinogalactan or combined into TDM. Exactly how the extremely hydrophobic mycolic acids traverse the periplasmic space remains unknown, but upon reaching their destination they are utilized by different isoforms of the secreted antigen 85 (Ag85 A/B/C) complex, which function as mycolyl transferases. Each isoform of Ag85 is capable of catalyzing either the transfer of mycolate to

arabinogalactan or the creation of TDM, but the substrate specificities and transfer efficiencies of each differ between homologs[63,64].

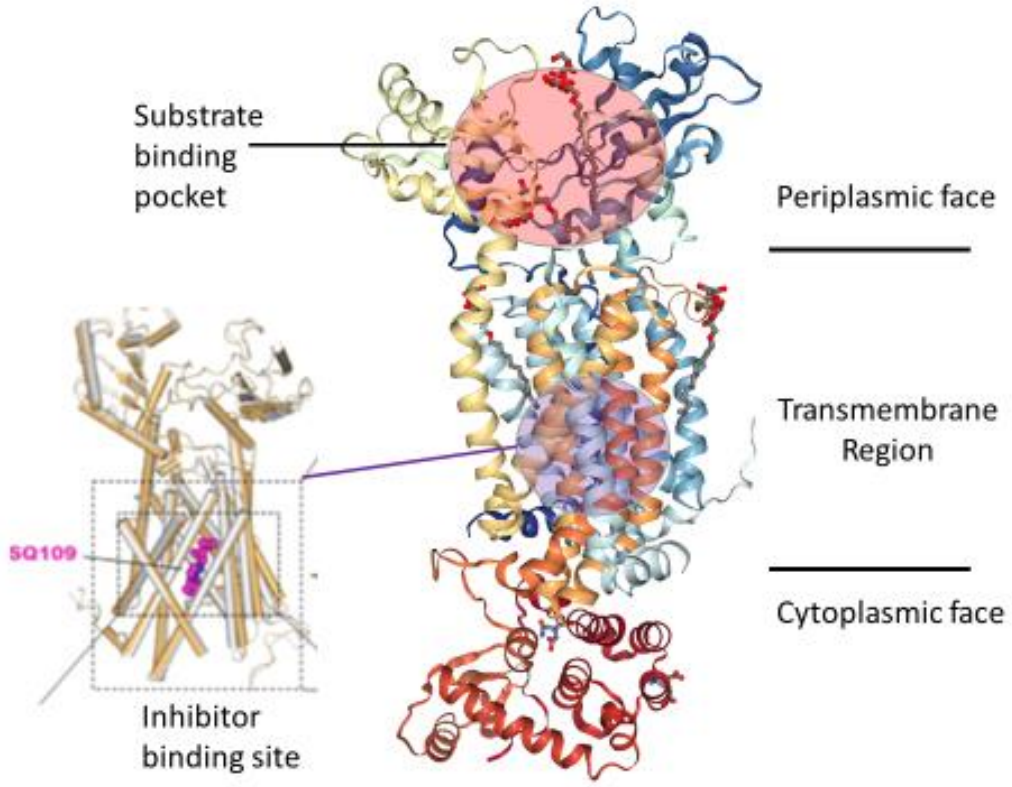

Figure 7 – Crystal structure of MmpL3

Crystal structure of *M. smegmatis* MmpL3. Three domains are visible in the structure, a periplasmic face, transmembrane region, and cytoplasmic face. The transmembrane region consists of twelve transmembrane spanning (TMS) alpha helices located in the center of the structure. The crystal structure was also obtained in the presence of inhibitor SQ109 bound (pink spheres) visualized in the cutaway image. 6-n-dodecyl-α, α-trehalose (6-DDTre) detergent molecules bound to the structure in a suspected substrate binding site are visualized as grey sticks, and are found lateral to the TMS as well as occupying a hydrophobic pocket in the periplasmic domain.

(PDB: 6AJF, Zhang et al. Crystal Structures of Membrane Transporter MmpL3, an Anti-TB Drug Target. (2019) *Cell* **176**: 636-648)

1.4 – MmpL3 As a Novel Therapeutic Target

Over the past half century, the frontline medications available for the treatment of tuberculosis have not significantly varied from the standard HRZE regimen established in the 1960's. Current treatment consists of two phases, a two month intensive phase requiring daily dosage of isoniazid (H), rifampin (R), pyrazinamide (Z), and ethambutol (E), followed by a four month continuation phase of daily isoniazid and rifampin[110]. This six-month treatment duration is effective at clearing *Mtb* infections assuming full drug susceptibility, however high levels of resistance to both isoniazid and rifampin have been observed and these multidrug (MDR) resistant clinical isolates require more extensive treatment durations, sometimes in excess of 24 months[4]. Combination therapy of drugs targeting different metabolic pathways is required due to the constant frequency of spontaneous mutation encountered in *M. tuberculosis*[111].

The unique biosynthesis of the myco-membrane is rich in essential enzymes, and many of the frontline drugs accordingly target aspects of cell wall biosynthesis. Isoniazid was shown to inhibit InhA[112,113], part of the catalytic elongation cycle of the FAS II system, while ethambutol inhibits the proper synthesis of cell wall arabinogalactan which then impedes the incorporation of mycolic acid into the outer membrane[114,115]. Pyrazinamide is a neutral prodrug which can penetrate the hydrophobic membrane where it is activated by mycobacterial pyrazinamidase into pyrazinoic acid[116]. Importantly, pyrazinamide shows little activity against actively growing cells, instead performing its sterilizing activity on slow growing or metabolically inactive persistor cells[117,118]. Rifampin is a broad-spectrum antibiotic which performs its bactericidal function through the inhibition of RNA polymerase[119]; point mutations in RNA polymerase have been shown to lead to high levels of resistance to rifampin, which is a principle diagnostic phenotype for MDR-TB[120].

The emergence of multidrug-resistant (MDR) and extensively drug-resistant (XDR) TB, along with the rising prevalence of extremely resistant NTM infections[19,20] has prompted the need to develop new pharmaceutical countermeasures and discover new druggable targets in the CMN family[121]. MmpL3 has been identified as both a druggable and novel therapeutic target[122], validated by both in-vitro studies[108,123,124], and in-vivo mouse infection models[125]. Not surprisingly, significant efforts have been focused on finding small-molecule inhibitors which selectively inhibit this unique mycobacterial target[126] as treatment options for mycobacterial pathogens are extremely limited[127].

Screening large compound libraries for active chemical compounds in *Mtb* identified several hits acting on MmpL3, however their specificity and mechanism of action remain unclear. The ethylenediamine SQ109[128,129] was identified as an inhibitor of MmpL3 based on observed cell wall defects and spontaneous resistant mutants[130], and has since completed a Phase 2b clinical trial where it was demonstrated safety and efficacy in combination for the treatment of MDR-TB[131]. The adamantyl urea compound AU1235 was identified during random library screening to have potency against *Mtb*, and the cell wall mycolate defects observed due to AU1235 treatment were used to initially determine the function of MmpL3 as the mycolic acid transporter in mycobacteria[123,126,132]. A novel pyrrole derivative, BM212 was shown to have good antitubercular activity, and surprisingly even better potency against NTM infections[133,134].

Membrane transporters of the Resistance-Nodulation-Division (RND) superfamily are efflux pumps which recognize a wide variety of substrates and provide significant antibiotic resistance in Gram-negative bacteria. They possess twelve transmembrane spanning alpha helices, with protruding periplasmic loops located between helices 1 & 2 and 7 & 8, and can function monomerically or in multimeric complexes. In Gram-negative bacteria, the RND transporter can function as part of a tripartite complex (see **Figure 2** above) where the RND pump is located in the

plasma membrane, an outer membrane channel is located in the asymmetric outer membrane, and a membrane fusion protein connects the RND to the outer membrane channel. When the RND complex is assembled, it carries out the efflux of substrates captured from the periplasm or plasma membrane and pumps them through the outer membrane channel and out of the bacterial cell [135].

The pumping mechanism of the RND transporter is achieved through the cycling of three conformations of each protomer: the initial loose (L) conformation allows potential substrates access to the vestibule inside the protomer where the binding site is not fully accessible yet, then the internal binding site expands allowing the substrates to bind tightly (T) to the protomer after which the vestibule closes off (O) and the substrate is extruded though the central channel and out of the cell through the outer membrane channel [136,137]. Energy to drive these conformational changes derives from a proton-antiport mechanism along a highly conserved salt bridge along the transmembrane helix 4 and 10 interface[138]. In the most studied RND transporter, AcrB from *Escherichia coli*, this salt bridge consists of the highly conserved functional residues D407, D408, and K940 which were identified as the protonation sites necessary for proton transport [138,139]. In both the loose (L) and tight (T) protomer conformations, the positively charged K940 residue is stabilized between the two negative residues D407 and D408 which prevents their protonation. For substrate extrusion in the open (O) conformation, substrate binding causes a rotational shift (14^{o} total) in transmembrane helix 10 moving the K940 residue which is then stabilized by another conserved essential residue T978, allowing the sequential protonation of the two aspartate residues [140]. This model presents a reasonable H^{+}:substrate anti-port mechanism through which substrate binding signals are coupled to proton transport, and mutagenesis studies on these essential residues have resulted in the inactivation of the transporter [138].

The crystal structure of a C-terminally truncated MmpL3 from *M. smegmatis* (**Figure 7**)[141] revealed that MmpL3 has twelve transmembrane helices with two periplasmic loops in a similar orientation as that found in a single protomer of a typical Gram-negative RND efflux pump. Earlier structural studies of MmpL3 suggested a homotrimer quaternary structure with central hydrophobic vestibule and an access pore located between protein subunits based on negative-EM staining and homology modelling [142]. It was observed that 6-n-dodecyl-α, α-trehalose (6DDTre), a mimic for the native TMM substrate, was found stabilized by hydrogen bonds to a hydrophilic opening located on the periplasmic face of the protein. In agreement with the classification of MmpL3 as an RND transporter and in comparison with AcrB, a highly conserved pair of Asp-Tyr residues were observed in the center of the transmembrane region along helix 4 and helix 10, and are believed to form the proton translocation pathway [141]. As an RND transporter, it is expected that MmpL3 undergoes a conformational change cycle similar to the LTO conformations observed with AcrB, however this is currently unknown.

In this same work, crystal structures of MmpL3 in complex with inhibitors SQ109 and AU1235 were obtained which revealed that the inhibitors bound directly between these Asp-Tyr pairs **(Figure 8)**, with the nitrogen atoms on the inhibitor backbone coordinating to the aspartate residues in the proton transport pathway. This inhibitor binding would prohibit any H^+ transport through the protein, and therefore inhibit a H^+:substrate anti-port mechanism. Mycolic acid transport is highly conserved in members of the CMN family, with the principle mycolic acid transporter of corynebacteria being CmpL1[142,143]. The observed H^+ translocation path in the MmpL3 crystal structure is also present in a homology model of CmpL1 **(Figure 8)** with a high degree of similarity.

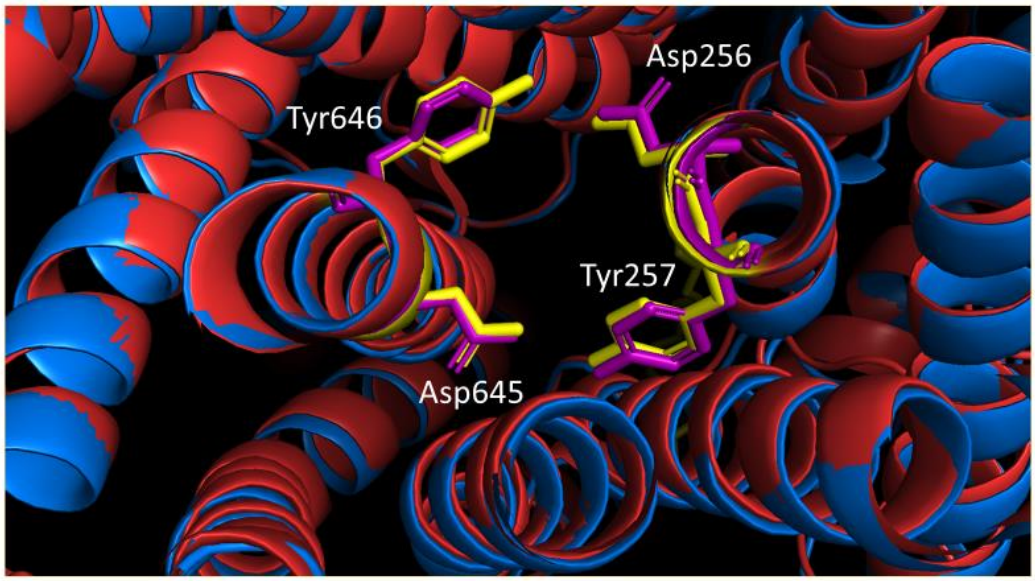

Figure 8 – Inhibitor binding site of MmpL3 and CmpL1
The crystal structure of *M. smegmatis* MmpL3 (Red ribbon) with the proton transport Tyr-Asp pairs visualized as yellow sticks. A homology model of CmpL1 (Blue ribbon) was overlaid with the Tyr-Asp residues visualized as purple sticks.

Despite substantial progress in understanding the essential transport of mycolic acids, the exact mechanism by which the transporters recognize and transports TMM is still elusive. Due to the intrinsic complexity of the CMN family outer membrane, assessing direct interaction of inhibitor compounds with membrane proteins is a challenge, and thus far, the development of *Mtb* MmpL3 inhibitors has been based on screening for active compounds and then generating spontaneous mutants to identify drug targets. The current MmpL3 inhibitors being developed for clinical trials (AU1235, SQ109, BM212) all have divergent chemical scaffolds, yet isolated MmpL3 point mutants can convey resistance to multiple different pharmacophores. Additionally, the conserved inhibitor binding site between distant relatives in the CMN family suggests the possibility of broad-spectrum mycolic acid transport

inhibition. The result chapters reported in this dissertation reflect our work to address these outstanding questions and advance the development of anti-CMN family therapeutics.

Chapter 2 - Methods

2.1 - Strains and growth conditions

E. coli Rosetta (DE3) and *E. coli* C43 (DE3) cells were grown at 37 °C with shaking in LB broth. The avirulent strain *M. tuberculosis* H37Rv mc^2 6206 (Δ*panCD* Δ*leuCD*) was grown at 37 °C in Middlebrook 7H9-OADC, 0.05 % tyloxapol supplemented with 0.2 % casamino acids, 48 µg/mL pantothenate and 50 µg/mL L-leucine. *M. smegmatis* mc^2 155 was grown at 30 ^{0}C in Middlebrook 7H9 broth+10 % ADC supplement with 0.05 % Tween 80 with shaking. *C. glutamicum* strains: ATCC 13032 (WT), LY108 (*ΔCmpL1 ΔCmpL2 ΔCmpL3*), LY109 (*ΔCmpL2 ΔCmpL3 ΔCmpL4*)[143] were grown at 30 ^{0}C in 2xTY media with shaking. For *M. smegmatis*, hygromycin B (50 μg/ml) and kanamycin (25 μg/ml) and for *C. glutamicum* kanamycin (25 μg/ml) were used as selection markers. For *E. coli* kanamycin (50 μg/ml) and ampicillin (100 μg/ml) were used.

2.2 - Protein purifications

MmpL3 Purification

Mtb MmpL3 was purified as follows. *M. smegmatis ⊿MmpL3* cells harboring pMVGH1:MmpL3(tb) were inoculated into the 7H9-ADC medium supplemented with 0.2 % glycerol, 0.05 % Tween-80, 25 μg/mL kanamycin, 50 μg /mL hygromycin B, and incubated for 48 hours at 30 ^{0}C with shaking. The cell pellet from 1 liter culture was resuspended in 20 mL of TM Buffer (10 mM Tris-HCl (pH 8.0), 1 mM $MgCl_2$) with 100 μg /mL DNase I and 1.0 mM PMSF, and cells were broken with 3-4 passes through French Press (20,000 psi). Unbroken cells were removed via centrifugation at 16,000 x g, and membranes were collected by ultracentrifugation at 185,000 x g, at 4 ^{0}C for 1 hour. The membrane pellets were solubilized 4-12 hours at 4 ^{0}C in TS Buffer (20 mM Tris-HCl (pH 8.0), 150 mM NaCl, 2 % Triton X-100). Insoluble material was removed via ultracentrifugation at 185,000 x g, 4 ^{0}C for 1 hour,

supernatant was collected and NaCl concentration was increased to 200 mM (final). The sample was then passed through a HiTrap Q-FF (5 mL - GE Healthcare) anion exchange column at a flowrate of 0.5 mL/min. Flow-through was collected and adjusted to 400 mM NaCl and 10 mM imidazole (final concentrations) and loaded onto His-Bind affinity resin (Novagen). Column was washed two times with ten column volumes of TW Buffer (20 mM Tris-HCl (pH 8.0), 400 mM NaCl, 20 mM imidazole, 0.2 % Triton X-100), and then the column was washed two times with 10 column volumes of HW Buffer (20 mM HEPES-KOH (pH 8.0), 400 mM NaCl, 20 mM imidazole, 0.2 % Triton X-100). MmpL3 was then eluted in six fractions with 0.5 CV of HE Buffer (20 mM HEPES-KOH (pH 8.0), 400 mM NaCl, 500 mM imidazole, 0.2 % Triton X-100).

CmpL1 Purification

C. glutamicum CmpL1 was purified as follows. 2xTY media (16 g tryptone, 10 g yeast extract, 5 g NaCl per liter) was inoculated with LY108[143] harboring pAN6:CmpL1 overnight at 30 ^{o}C with shaking. The cells were sub-cultured 1:100 in fresh 2xTY media for two hours then induced via addition of 0.1 mM IPTG for an additional 2 hours at 30 ^{o}C with shaking. Each 1 L pellet was resuspended in 20 mL of TM Buffer (10 mM Tris-HCl pH 8.0, 1 mM $MgCl_2$) with 100 μg/mL DNase I and 1.0 mM PMSF, and cells were broken with 3-4 passes through French press. Unbroken cells were removed via centrifugation at 16,000 x g, and membranes were collected by ultracentrifugation at 185,000 x g, 4 ^{0}C for 1 hour. The membrane pellets were solubilized 4-12 hours at 4 ^{0}C in TS Buffer (10 mM Tris-HCl pH 8.0, 150 mM NaCl, 2 % Triton X-100). Insoluble material was removed via ultracentrifugation at 185,000 x g, 4 ^{0}C for 1 hour, supernatant was collected and flowed through a StrepTactin II (GE) column pre-equilibrated with TS buffer. The column was washed with TS buffer and protein was eluted in TE buffer (10 mM Tris-HCL pH 8.0, 150 mM NaCl, 0.2 % Triton X-100, 2.5 mM desthiobiotin).

CrgA and Pks13 Purification

M. tuberculosis CrgA (Rv0011c) and Pks13 (Rv3800c)) were purified as follows: 5 mL of *E. coli Rosetta* (BL21) cells harboring pET29a::*crgA* or pET26b::*pks13* were grown in LB broth plus 25 μg/mL kanamycin overnight at 37 ^{o}C. Cells were sub-cultured 1:100 in fresh LB broth plus kanamycin and grown to OD_{600} 0.6-0.8, and then induced with 0.1 mM IPTG for 4 hours at 37 ^{o}C. Cells were harvested by centrifugation at 16,000 x g for 20min, then resuspended in lysis buffer (50 mM Tris-HCl pH 8.0, 5 mM EDTA, 1 mM PMSF) and broken via sonication. Unbroken cells were removed with centrifugation at 16,000 x g, and then membranes were collected by ultracentrifugation at 185,000 x g at 4^{o}C for 1 hour. Membranes were solubilized with HS buffer (20 mM HEPES-KOH pH 7.4, 150 mM NaCl, 2 % Triton X-100) overnight at 4 ^{o}C with stirring. Insoluble material was removed by ultracentrifugation at 185,000 x g at 4 ^{o}C for 1 hour. Soluble sample were then loaded onto HIS bind resin and washed extensively with HW buffer (20 mM HEPES-KOH pH 7.4, 150 mM NaCl, 0.2 % Triton X-100, + [20 column volumes of 20 mM imidazole then 6 column volumes of 50 mM imidazole]), before final elution with HW + 500 mM imidazole.

Rv0207c and LprC Purification

M. tuberculosis Rv0207c and LprC (Rv1275) were purified as follows. 5 mL of *E. coli* Rosetta (BL21) cells harboring pET29a::*rv0207c*, or *E. coli* (C43) cells harboring pET14b::*lprC*, were grown in LB broth plus (25 μg/mL kanamycin or 100 μg/mL ampicillin respectively) overnight at 37 ^{o}C. Cells were sub-cultured 1:100 in fresh LB broth plus appropriate antibiotic, and grown to OD_{600} 0.6-0.8, and then induced with 0.1 mM IPTG overnight at 16 ^{o}C. Cells were harvested by centrifugation at 16,000 x g for 20 min, then resuspended in lysis buffer (50 mM Tris-HCl pH 8.0, 5 mM EDTA, 1 mM PMSF) and broken via sonication. Unbroken cells were removed with centrifugation at 16,000 x g, and then membranes were collected by

ultracentrifugation at 185,000 x g at 4^{o}C for 1 hour. Membranes were solubilized with HS buffer (20 mM HEPES-KOH pH 7.4, 150 mM NaCl, 2 % Triton X-100) overnight at 4 ^{o}C with stirring. Insoluble material was removed by ultracentrifugation at 185,000 x g at 4 ^{o}C for 1 hour. Soluble samples were passed through a SP-HP cation-exchange column (GE Healthcare), and flow-through was spiked to 20 mM imidazole and 200 mM NaCl (final concentrations) before loading onto HIS-bind resin. The column was washed extensively with HW buffer (20 mM HEPES-KOH (pH 7.4), 150 mM NaCl, 0.2 % Triton X-100, + [20 column volumes of 20 mM imidazole then 6 column volumes of 50 mM imidazole]), before elution with HW buffer + 500 mM imidazole.

MviN Purification

M. tuberculosis MviN (Rv3910) was purified as detailed above for Pks13; with the only differences as follows: *E. coli* (C43) cells harboring pET29a::*mviN* were utilized, and cells were induced with 0.1 mM IPTG overnight at 37 ^{o}C.

AftD and Antigen 85

In addition to our five purified proteins (above), we also acquired the Mtb arabinosyl-transferase AftD which was purified by a collaborative research group of Filippo Marica (Columbia University, New York, NY). The antigen 85 complex of secreted mycolic acid transferases was available commercially (BEI).

2.3 - MIC assays

Minimal inhibitory concentration (MIC) of compounds were determined as detailed previously[126] for *M. tuberculosis*. *C. glutamicum* minimal inhibitory concentrations were obtained by serial two-fold dilution on 96-well plates which were incubated at 30 ^{0}C and analyzed visually for growth after 48 hours[143].

2.4 - SPR binding assays

A purified protein was amine-crosslinked to a flowcell of a CM5 Series S chip (GE Healthcare) which was activated with 0.05 M N-hydroxysuccinimide and 0.2 M N-ethyl-N-(3-diethylaminopropyl)carbodiimide (BIAcore). After immobilization, the remaining unreacted groups were quenched by the injection of 0.5 M ethanolamine HCl (pH 8.0). The immobilized baseline measurement and final binding assays were performed in running buffer containing: 25 mM HEPES-KOH (pH 7.0), 150 mM NaCl, 0.2 % Triton X-100, and 5 % DMSO. A second flowcell (to serve as a reference subtraction), was prepared in exactly the same manner, omitting protein during the immobilization step. A two-fold concentration series of inhibitors were prepared and injected sequentially in order of increasing concentration with a flowrate of 30 μL/min, the injection phase lasting 30 sec (association) followed by a 60 sec collection of running buffer (disassociation). Sensorgram results were normalized to the initial blank injection which contained only running buffer, and then the reference flowcell sensorgram was subtracted from the protein sensorgram. Data was analyzed and fitted globally to 1:1 and Two-State binding models.

Kinetic Binding Models

$$A + B \underset{k_{d1}}{\overset{k_{a1}}{\rightleftharpoons}} AB \qquad \text{(1 : 1 Binding)}$$

$$A + B \underset{k_{d1}}{\overset{k_{a1}}{\rightleftharpoons}} AB^* \underset{k_{d2}}{\overset{k_{a2}}{\rightleftharpoons}} AB \qquad \text{(Two-State Binding)}$$

For protein-protein binding interactions, injected proteins were concentrated to 10 μM concentration, then a 2-fold dilution series was made with injections happening sequentially and in order of increasing concentration. SPR Assay Buffer was 20 mM HEPES-KOH (pH 7.4), 150 mM NaCl, and 0.2 % Triton X-100, and proteins were injected at 10 μL/min for 30 seconds and then allowed to disassociate for an additional

180 seconds. Data was collected at 10 Hz at 20 °C, and all global data fits were made with a 1:1 binding model. SPR experiments were carried out using a Biacore T200 instrument of the Oklahoma Medical Research Foundation Biacore Facility, which is funded by the Shared Instrumentation Grant S10 OD025014.

$$R_{Max} = R_{Ligand} \times \text{Binding Valency} \times \left[\frac{MW_{Analyte}}{MW_{Ligand}}\right]$$

Calculation of Maximum Response for SPR

Formula for the calculation of the expected maximal response for a given Ligand:Analyte binding interaction during Surface Plasmon Resonance. R_{Max} is the expected maximal response, R_{Ligand} is the amount of immobilized protein on the flow-cell surface, Binding Valency is the number of binding sites on the Ligand for each Analyte, and the final term is the ratio of molecular weights of the analyte/ligand.

2.5 - BLI binding assays

Biolayer Interferometry (BLI) was performed using AR2G sensors loaded with purified MmpL3(tb) on an Octet RED96 instrument (ForteBIO). Sensors were hydrated for 1 hour and then activated for 600 seconds with 20 mM 1-ethyl-3-(-3-dimethylaminopropyl) carbodiimide hydrochloride (EDC) and 10 mM Sulfo-N-hydroxysuccinimide (Sulfo-NHS) (AR2G Reagent Kit, ForteBIO). Activated sensors were loaded in wells containing the purified protein in sodium acetate buffer pH 4.0, then quenched for 500 seconds in ethanolamine pH 8.0, and finally returned to assay buffer (20 mM HEPES-KOH pH 8.0, 150 mM NaCl, 0.2% Triton X-100). A second set of sensors, devoid of MmpL3(tb) protein, were activated as above and then quenched to serve as an empty sensor control for double-

subtraction data processing (see second reference below). BLI binding assays were performed as follows: After sensor equilibration for 250 seconds, a baseline was established in assay buffer for 60 seconds. Increasing two-fold dilutions of compounds were scanned for interaction with the proteins by first dipping into compound wells for 30 seconds, then returning to the baseline well and monitoring dissociation for 60 seconds. Sensors were dipped into fresh assay buffer and allowed to equilibrate for 250 seconds between binding assay steps. Sensors were oriented so that a protein-loaded sensor was always dipped into fresh assay buffer while the other protein-loaded sensors were incubated with the test compounds (first reference). The entire assay was repeated with a set of sensors devoid of protein using the same compound plate after the assays with loaded sensors were complete (second reference). All assay steps were performed in the Octet RED96 instrument at 25 ^{o}C under agitation (500 rpm). Assay development and data acquisition was performed using the BLI Acquisition Software 9.0.0.37 (ForteBIO). Data were processed and binding curves were globally fit using the BLI Analysis Software 9.0.0.12 (ForteBIO) to 1:1 and Two-State binding models.

2.6 - Partial Proteolysis

Proteolysis of *M. tuberculosis* MmpL3 / MmpL3(G253E) was carried as follows. Purified protein was diluted in assay buffer (20 mM HEPES-KOH (pH 8.0), 150 mM NaCl, 0.2 % Triton X-100) to a final concentration of 100 nM. Compounds were added to the protein samples to a final concentration of 200 μM (solubility permitting) at 5 % DMSO and allowed to incubate for 5 min at room temperature before the addition of trypsin. A ten-fold trypsin gradient was performed for all tested compounds, and the digest was carried out for 30 min at 37 ^{o}C.

2.7 - Silver Staining

Samples were separated via SDS-PAGE and visualized with silver-staining as follows: SDS-PAGE gels were fixed for one hour at room temperature in 40 % methanol with 0.15 % formaldehyde. Gels were rinsed twice with water for five minutes, and then incubated for one minute in 1.25 mM sodium thiosulfate solution. After two brief 20 second rinses with water, gels were incubated for 10 minutes in 0.1 % silver nitrate. Lastly, gels were rinsed once with water for 20 seconds then developed (3 % sodium carbonate, 250 μM sodium thiosulfate, 0.075 % formaldehyde) until bands appeared, and the reaction was quenched by the addition of 2.3 M citric acid.

2.8 – Protein reconstitution into proteoliposomes and assays.

Reconstitution of MmpL3 was carried out as previously described[144] with modifications as follows. *E. coli* polar lipids (Avanti) were dissolved in chloroform and dried under vacuum overnight. Prior to reconstitution, lipids were resuspended in reconstitution buffer (25 mM HEPES-KOH (pH 7.0), 1 mM DTT, 100 mM KCl) to a concentration of 20 mg/ml and sonicated briefly (Branson 1510 water-bath sonicator). 50 μL of purified MmpL3 (350 μg/mL) was mixed with 4 mg of dispersed lipids, and the volume was adjusted to 500 μl via addition of reconstitution buffer + 1.1 % β-OG[145]. Sample was incubated at room temperature for 10 minutes, then diluted slowly to 35 ml with prechilled reconstitution buffer and allowed to dialyze for 1 hour at 4 ^{0}C with stirring against reconstitution buffer + SM-2 BioBeads (2 g/L)[146]. The sample was then ultra-centrifuged at 162,000 x g for 90 min, and the resulting pellet was resuspended in 200 μL of reconstitution buffer. Pyranine was added to the sample at a final concentration of 2 mM, and the sample was extruded first through a 400

nm, then a 200 nm pore (Avanti Mini Extruder). Sample was then diluted to 2.5 mL with reconstitution buffer and passed through a PD-10 gel filtration column (GE Life Sciences) to remove untrapped pyranine. Control vesicles devoid of MmpL3 were prepared in parallel by the addition of reconstitution buffer in lieu of protein. For reconstitution assays with substrate analogs, 50 nM substrate was incubated with vesicles for five minutes prior to their addition to buffers, and data collection began immediately, and unless otherwise indicated inhibitor concentration in the 96-well plate was 50 nM.

2.9 - Homology Modelling

The crystal structure of MmpL3 (PDB: 6ajf) was identified by the SWISS-MODEL workspace as the closest match for the CmpL1 primary sequence. A homology model for CmpL1 was generated based on the crystal structure of MmpL3, with a GMQE of 0.72 and a QMEAN of -1.80. The homology model of CmpL1, along with the crystal structure of MmpL3 were aligned and investigated using PYMOL.

Chapter 3 - Purification and Functional Characterization of Mycolic Acid Transporters of *Corynebacterium glutamicum* and *Mycobacterium tuberculosis*.

3.1 Introduction

Tuberculosis is the leading cause of infectious disease still afflicting a major percentage of the world, yet it is but one of many difficult to treat infections caused by the CMN family. To effectively combat these diseases we require additional, and more effective treatment options. An extensive search for new therapeutic targets against *M. tuberculosis* (*Mtb*) revealed that the essential membrane protein MmpL3 performed a unique role in the membrane assembly of mycobacteria, namely the transport of mature mycolic acids across the cellular membrane. Despite being highly conserved across mycolic acid containing species, a gap in the basic understanding of the mechanistic function of MmpL3-like proteins presents many challenges for therapeutic development. The physiological function of MmpL3 as the exporter of mycolic acids is well established. In these studies, we sought to reveal the biochemical mechanism by which MmpL3 transports mycolic acids. Purification of membrane proteins presents its own challenges, which are further complicated in mycobacterial cells by the abnormally impermeable outer myco-membrane. To begin our study on the mechanism of mycolic acid transport, we purified the full-length CmpL1 from *C. glutamicum* and MmpL3 from *M. tuberculosis.* After purification was achieved, we assayed the proteins for function which was accomplished by the biochemical reconstitution into proteoliposomes. Upon successful reconstitution we were able to assess the proteins for their ability to facilitate H^+ movement in the presence of substrate analogs. Here we report our results on the purification of CmpL1 and MmpL3, and successful incorporation of both into proteoliposomes. Our results with the

reconstitution of these proteins revealed the first mechanistic insight into their function as H^+-dependent RND transporters.

3.2 Results

3.2.1 Purification of CmpL1

Corynebacteria possess the shortest length mycolic acids in the CMN family and accordingly have some of the simplest outer membranes to work with for the isolation of membrane components. *C. glutamicum* was chosen for the wealth of knowledge available due to its use commercially in the production of amino acids[147], as well as its physiological similarity to pathogenic agents *C. diphtheria* and *C. ulcerans.* In *C. glutamicum,* CmpL1 is the MmpL3 analog and belongs to the Resistance-Nodulation-Division (RND) superfamily of membrane transporters[143]. As such, CmpL1 is an 83 kDa integral membrane protein possessing twelve transmembrane helices, with large periplasmic loops between helices 1 and 2, and 7 and 8. Negative-staining electron microscopy studies showed that CmpL1 exhibits a homo-trimeric quaternary structure [142]. Based on homology with other RND transporters, we hypothesized that this transporter excretes mycolic acids via a H^+-coupled anti-port mechanism.

For the purification of CmpL1 we utilized wild type *C. glutamicum* ATCC 13032 strain harboring a corynebacterial expression vector pAN6 carrying a copy of *cmpL1* gene encoding a modified version of CmpL1 containing a C-terminal eight amino acid strep-tag[148]. Expression of CmpL1 from the pAN6 vector was under the control of the lac promoter and induced by the addition of isopropyl β-d-1-thiogalactopyranoside (IPTG, Sigma). The expression of CmpL1 was confirmed by isolating the membranes and quantifying total membrane protein via a Bradford assay. After quantification, total membrane protein was normalized to 16 μg per lane and analyzed by a 12% SDS-PAGE. Protein was visualized by immunoblotting using a monoclonal anti-strep antibody, and

overexpression was observed as increased band intensity in the induced membranes, the results of which are shown in **Figure 3.1A.**

Once expression was confirmed, we continued the purification process, optimizing conditions for membrane solubilization and protein stability. Further optimization of the growth and induction conditions did little to increase the eventual yield of CmpL1, so we opted to scale-up our culture conditions instead, which resulted in a yield of 0.5 mg/L of CmpL1 of cultured cells **(Figure 3.1B)**.

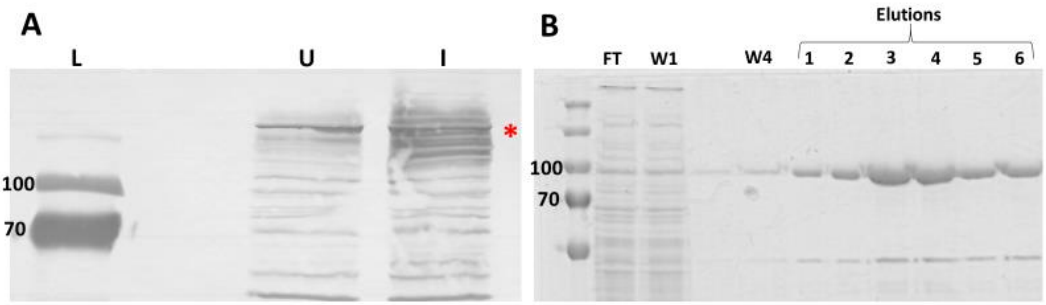

Figure 3.1 – Expression and Purification of corynebacterial CmpL1. **A)** Total membrane fractions of *C. glutamicum* were isolated from cells induced for the expression of CmpL1 with 0.1mM IPTG Samples were loaded at 16 μg per lane on a 12% SDS-PAGE gel and visualized using anti-strep tag immunoblotting. '**L**' is PageRuler Plus molecular weight marker, '**U**' is the uninduced cells, '**I**' are the induced cells. Molecular weight standards are indicated for 70 kDa and 100 kDa. Red asterisk indicates band for CmpL1. **B)** 10% SDS-PAGE of affinity purified CmpL1 stained with Coomassie blue. Molecular weight standards are indicated for 70 kDa and 100 kDa. FT: flow-through from Strep affinity column of solubilized membrane fraction, W1/W4 indicate wash fractions from Strep affinity column, Elutions (1-6) indicate sequential 0.5CV elution fractions containing 2.5mM desthiobiotin.

3.2.2 Purification of MmpL3

Mycolic acids of mycobacteria are among the longest of the CMN family, with the mero-chain often reaching approximately 80 saturated carbons in length, and when incorporated into the outer myco-membrane this creates a barrier of extreme impermeability. These extremely unusual lipid species are synthesized inside the mycobacterial cell before their transport across the plasma membrane through the action of Mycobacterial membrane protein large 3 (MmpL3). Similar in architecture to CmpL1, MmpL3 is also a large 100.3 kDa integral membrane protein of the RND class superfamily of transporters, with twelve transmembrane helices and protruding periplasmic loops between helices 1 & 2 and 7 & 8.

For the purification of MmpL3, we initially sought to keep our expression systems identical to the conditions used for CmpL1. We anticipated being able to use a recombinant corynebacterial expression system for MmpL3 due to the similar physiology and membrane structure shared between members of the CMN family. Therefore, we utilized *C. glutamicum* LY108 (ΔCmpL1) harboring the pAN-6 expression vector carrying the full length MmpL3 gene from *M. tuberculosis* with a C-terminal strep tag. Proceeding from the previously established protocol for CmpL1, we confirmed weak expression of MmpL3 in the intact membrane fraction through separation by SDS-PAGE and western blotting (**Figure 3.2A**). We encountered problems when isolating MmpL3 from the corynebacterial membranes. SDS-PAGE analyses followed by immunoblotting showed severe MmpL3(tb) protein degradation (**Figure 3.2B**). Numerous optimization attempts were made to control this breakdown by varying the temperature of growth and assay conditions, as well as the addition of commercially available protease inhibitors. Despite these attempts, we were never successful in expressing intact MmpL3 in an appreciable yield from a corynebacterial host. Whether this was caused due to protein

misfolding in the recombinant system or proteolytic cleavage was ultimately never determined.

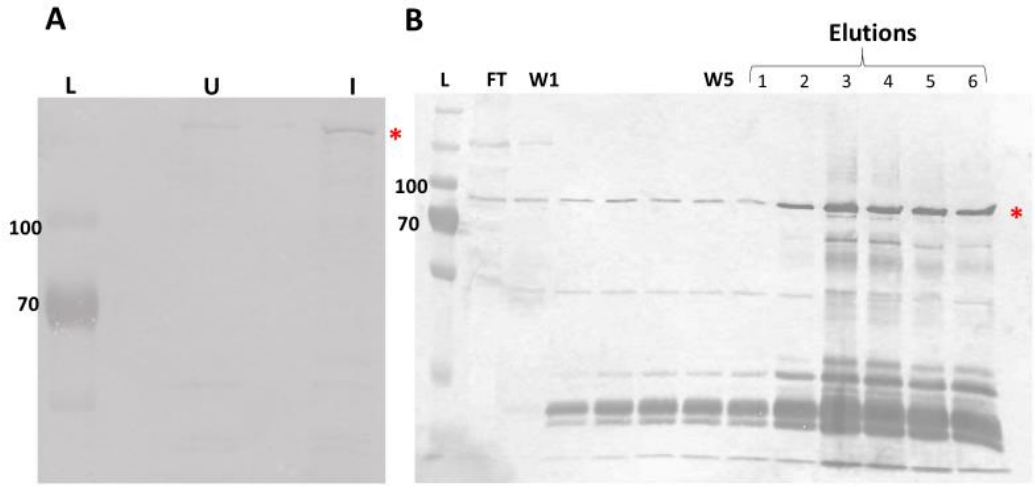

Figure 3.2 – Expression and purification of MmpL3(*Mtb*) from *C. glutamicum*.

A) Total membranes of *C. glutamicum* induced expression of MmpL3 with 0.1mM IPTG, loaded at 16 μg per lane on a 10% SDS-PAGE gel and visualized using anti-strep tag immunoblotting. '**L**' is PageRuler Plus molecular weight marker, '**U**' is the uninduced cells, '**I**' are the induced cells. Molecular weight standards are indicated for 70 kDa and 100 kDa. Red asterisk indicates band for MmpL3. **B)** 12% SDS-PAGE of affinity purified MmpL3 stained with Coomassie blue. Molecular weight standards are indicated for 70 kDa and 100 kDa. FT: flow-through from Strep affinity column of solubilized membrane fraction, W1/W5 indicate wash fractions from Strep affinity column, Elutions (1-6) indicate sequential 0.5CV elution fractions containing 2.5mM desthiobiotin.

To achieve the purification of MmpL3, we changed our expression host from *C. glutamicum* to *M. smegmatis (Msmeg)*, which is more physiologically similar to *M. tuberculosis (Mtb)*. Knockout strains of *Msmeg* MmpL3 were shown to be viable when expressing a recombinant MmpL3(*Mtb*) .[142] This result demonstrated that *Mtb* MmpL3 expressed in *Msmeg* is still intact and functional. Thus, our new expression system became *M. smegmatis*(Δ*mmpL3*) harboring the mycobacterial expression vector pMVGH1 carrying MmpL3(*Mtb*) with an 8x histidine tag on the C-terminus under the control of the *hsp*60 promoter. Immunoblot probing against the histidine tag confirmed protein expression and integrity, showing very little protein cleavage (**Figure 3.3A**). These results confirmed that the protein was more stably expressed in the mycobacterial system, and full purification of MmpL3(*Mtb*) was achieved with a final yield of 200 μg of MmpL3 per liter of cultured cells (**Figure 3.3B**).

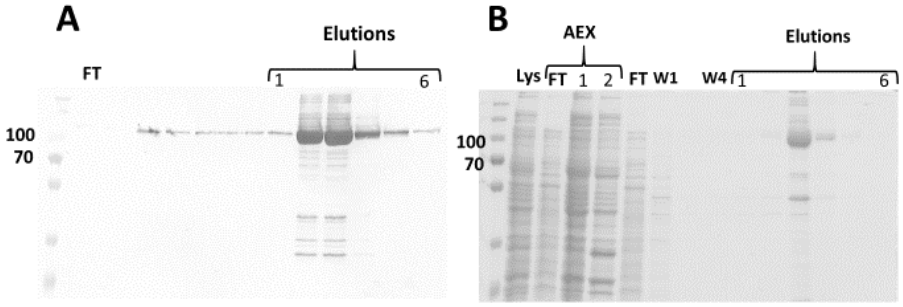

Figure 3.3 – Expression and Purification of MmpL3(*Mtb*) from *M. smegmatis*.

A) Anti-His immunoblot of MmpL3(*Mtb*) protein purified by His-bind affinity chromatography and analyzed by 12% SDS-PAGE. FT: flow-through from His-bind affinity column, Elutions (1-6) indicate sequential 0.5 CV fractions containing 500mM imidazole. Molecular weight standards are indicated for 70 kDa and 100 kDa. **B)** 12% SDS-PAGE of purified MmpL3 stained with Coomassie blue. Lys: membrane fraction solubilized with 2% Triton X-100, AEX-FT: flow-through from Q-Sepharose anion exchange column, AEX-1:

wash fraction from Q-Sepharose column containing 400mM NaCl, AEX-2: wash fraction from Q-Sepharose column containing 1M NaCl. FT: fraction 'AEX-FT' after passage through His-bind affinity column, W1/W4: sequential 10 CV wash fractions containing 20mM imidazole, Elutions (1-6): sequential 0.5CV fractions containing 400mM imidazole.

Section 3.2.3 – Reconstitution of CmpL1 and MmpL3 into proteoliposomes

In order to isolate and study the function of integral membrane proteins, they must first be liberated from the cell membrane and stabilized in an aqueous solution to allow biochemical assay. Traditionally this is accomplished by the use of a detergent or surfactant molecule in excess above the critical micellar concentration (CMC), which allows the solubilization of membrane components into detergent micelles. While useful for such applications as Surface Plasmon Resonance[149], for the study of membrane transporter activity this becomes problematic as there is no defining membrane compartments through which to assess movement of substrates. In these situations, it becomes necessary to reconstitute the protein into a lipid vesicle. Once the membrane proteins are incorporated back into lipids, the resultant proteoliposomes can then be subjected to tests for mechanistic function[144-146]. As MmpL3 and CmpL1 are members of the RND superfamily of membrane transporters, they are believed to function through H^+-coupled transport of their substrates[44,126,141,142]. In order to test this hypothesis, we reconstituted both MmpL3 and CmpL1 into proteoliposomes and assayed their activity in the presence of a H^+ gradient and tested them with a suspected substrate analog.

Protein reconstitution followed the protocol detailed in Methods. Briefly, a purified protein was mixed with *E. coli* polar lipids (Avanti) and reconstitution buffer containing 1.1% β-OG and allowed to mix briefly. The mix was then diluted 40-fold and then dialyzed against buffer without

detergent and containing SM2 Bio-Beads[150] (Bio-Rad) to remove any residual detergent molecules, then proteoliposomes were collected via ultracentrifugation. To monitor proton translocation, we used pyranine[151,152]. Pyranine is a pH sensitive fluorescent probe which demonstrates signal quenching upon acidification, and which also cannot passively diffuse across lipid bilayers allowing it to remain trapped in the proteoliposomes and function as a monitor for H^+ flux across our vesicle membranes, shown in **Figure 3.4**. Pyranine (Sigma) was added to reconstituted proteoliposomes, and the samples were passed through the polycarbonate membrane of a Mini-Extruder (Avanti) to a final diameter of 200nm. To remove any residual exterior pyranine, proteoliposomes were applied onto a PD-10 (GE Healthcare) desalting column, which traps small molecular weight solutes. Control 'empty' vesicles not containing protein were prepared in parallel, omitting protein from the reconstitution buffer.

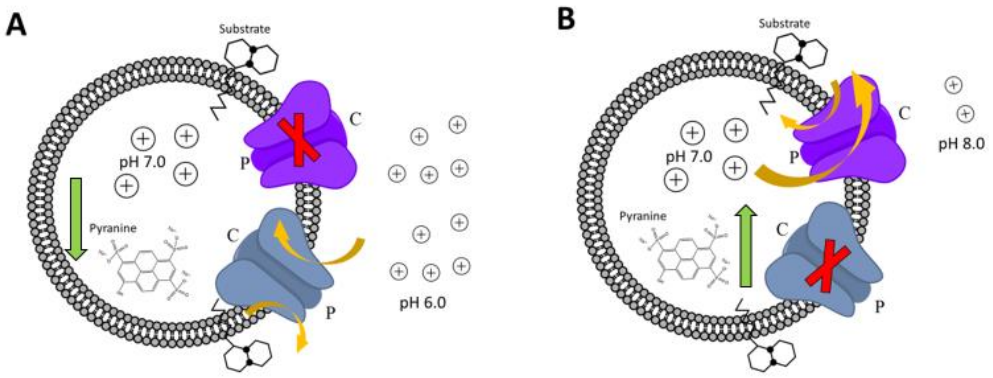

Figure 3.4 –Representation of a Reconstituted Membrane Transporter.

A cartoon schematic of our testing conditions for the activity of mycolic acid transporters. Once trapped in the vesicle, pyranine is unable to diffuse out across the lipid membrane and serves as a fluorescent reporter for an internal pH change. Shown in **A** and **B** are the two orientations proteins can adopt during proteoliposome formation.

First, we assessed the successful reconstitution of protein into proteoliposomes in order to ensure that we are not measuring any H^+ flux due to semi-permeable lipid bilayer. To achieve this, a set of parallel reconstitutions were performed with MmpL3, wherein we varied the amount of protein used during reconstitution and likewise we expected to recover protein from the proteoliposomes in a concentration dependent manner. As shown in **Figure 3.5**, we do not observe any protein in our empty control vesicles, while we observe a clear concentration dependent recovery of protein observed in the parallel reconstitutions. This result demonstrated that MmpL3 is reproducibly trapped in the lipid vesicles during reconstitution, and the subsequent data we acquire can be attributed to the activity of the protein in the lipid membranes.

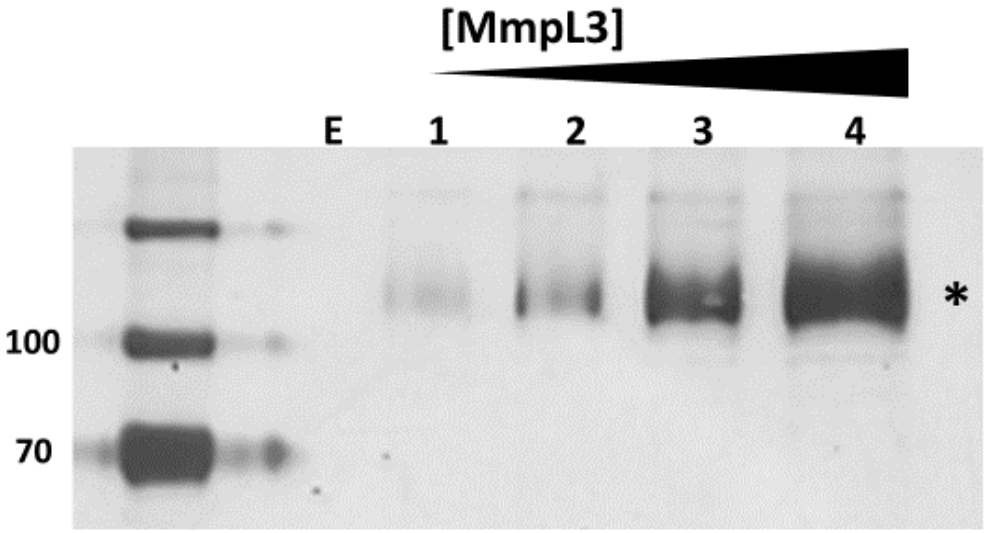

Figure 3.5 – Protein recovery after reconstitution.
Reconstitution experiments **E, 1 – 4** were carried out in parallel with increasing concentrations of MmpL3, where **E:** no protein control, **1:** 2µg MmpL3, **2:** 4µg MmpL3, **3:** 8µg MmpL3, and **4:** 16 µg MmpL3. Equal volumes (12 µL) of reconstituted liposomes were loaded onto 10% SDS-PAGE and separated by electrophoresis before visualization by silver-

staining. Molecular weight standards are indicated for 70 kDa and 100 kDa. Reconstituted MmpL3 indicated by the band at the asterisk.

Next, we sought to assay whether there was H^+ flux through the mycolic acid transporters in the presence of a H^+ gradient, which was achieved by monitoring the pyranine fluorescence over a five-minute period. As pyranine is trapped in the lumen of the vesicles, when we incubate the vesicles in buffer with a differing extravesicular pH, any H^+ movement into the vesicles will quench the fluorescent signal, and likewise H^+ flux out of the vesicles will result in increased fluorescent signal.

When protein-free vesicles with entrapped pyranine were pre-equilibrated in the pH 7.0 buffer, and then diluted into the pH 6.0 buffer or the pH 8.0 buffer, the pyranine fluorescence (therefore intravesicular pH) did not change significantly during the five minute experiment, suggesting that spontaneous leakage of H^+ in the reconstituted vesicles was negligible (**Figure 3.6A**).

MmpL3-containing vesicles reported no H^+ movement at the neutral pH, while reporting H^+ influx in the acidic conditions, and a comparable level of H^+ efflux when the extravesicular buffer was alkaline (**Figure 3.6B**). CmpL1 showed a similar H^+ influx to MmpL3 under acidic conditions, yet differed by also reporting a slight influx at neutral pH and surprisingly no movement of H^+ at alkaline conditions (**Figure 3.6C**).

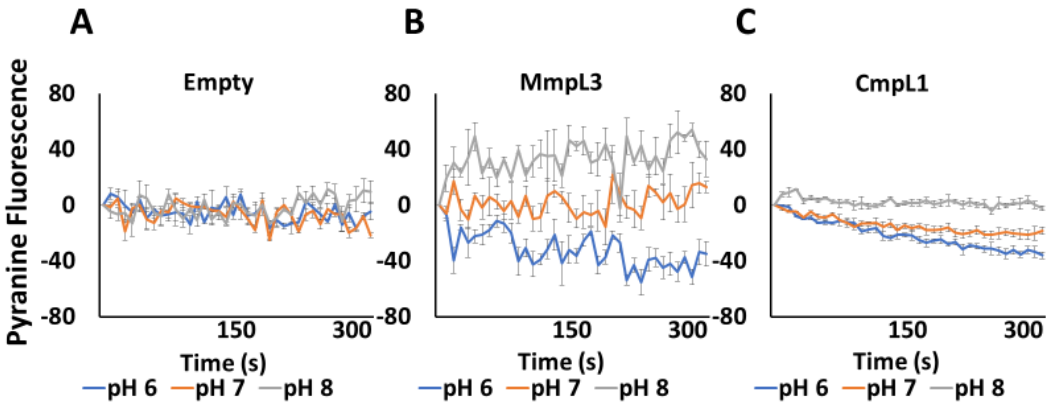

Figure 3.6 – Reconstituted mycolic acid transporter activity at different pH conditions.

A) Control vesicles with protein omitted during reconstitution show no change in fluorescence, indicating vesicles are formed with tight lipid packing and are not permeable to H^+. **B)** Reconstituted MmpL3 vesicles show H^+ flux in the direction of the gradient. **C)** Reconstituted CmpL1 vesicles show different H^+ flux behavior. Pyranine excitation was at 455 nm and emission was measured at 509 nm for five minutes at 25°C. Grey Line: alkaline pH 8.0, Orange Line: neutral pH 7.0, Blue Line: acidic pH 6.0. Error bars are standard deviations (n = 3).

It was observed in the crystal structure published of MmpL3[141] that there were molecules of 6-n-dodecyl-α, α-trehalose (6-DDTre) bound in a hydrophobic pocket in the periplasmic domain which could potentially function as an exit site during mycolic acid transport. To begin exploring potential substrate activities of MmpL3, we attempted to mimic the native substrate Trehalose Mono-Mycolate (TMM) with compound **AcTre67 (Figure 3.7)**, which possesses a palmitic acid esterified to a trehalose head group. For this assay we incubated the proteoliposomes with **AcTre67** prior to their addition to the differing pH buffers and monitored the fluorescence. When a substrate analog **AcTre67 (Figure 3.8A**) containing a trehalose headgroup acylated with a 16-carbon long tail was

added to the vesicles at the three different external pH, the lipid bilayer did not show significant changes in leakiness when compared to vesicles in the absence of the **AcTre67** (**Figure 3.6A**). **AcTre67** (0.05 μM) did not affect fluorescence when added directly to a solution of pyranine. The same results were obtained for other substrate mimetics of the MmpL3/CmpL1 pumps containing C4 (**AcTre246**), C10 (**AcTre243**), C12 (**AcTre244**), and C14 (**AcTre245**) hydrocarbon chains **(Figure 3.7)**.

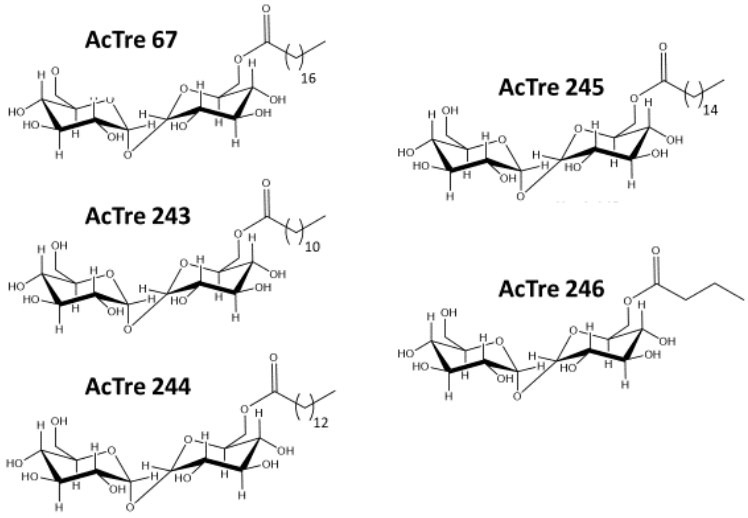

Figure 3.7 – Substrate analogs for Trehalose monomycolate (TMM) Substrate analogs for TMM were generated by the esterification of fatty acids with varying length acyl tails to trehalose disaccharides.

MmpL3-containing proteoliposomes exhibited no significant H^+ movement when mixed with the buffer at the neutral pH. However, the fluorescence of entrapped pyranine either increased or decreased when proteoliposomes were added into the pH 8.0 or the pH 6.0 buffer, respectively **(Figure 3.6B**), suggesting that in the presence of ΔpH, the reconstituted MmpL3 facilitates fluxes of H^+ across the membrane.

Importantly, this transport of H^+ was stimulated in the presence of the substrate **AcTre67**, as seen from the increased rates of pyranine fluorescence changes **(Figure 3.8B).**

In the early stages of proteoliposome formation the detergent-lipid-protein mixture is diluted well below the CMC of the β-octyl-glycoside detergent, which is used to promote the spontaneous aggregation of the lipids into vesicles where the protein is stabilized by, and then trapped in, the lipid bilayer as the detergent is diluted out. Lacking other forces guiding the vesicular formation, protein orientation in the final vesicles would be mostly sterically controlled, and a mixture of the two protein orientations can be expected. Working with the hypothesis that MmpL3 functions as a lipid-H^+ anti-porter, these observed results indicate that MmpL3 stably inserted into our lipid vesicles in both orientations and can function as a H^+ pump in each direction. The rates of fluorescence changes were comparable in the pH 6.0 and pH 8.0 buffers, which is also consistent with a random orientation of the protein in proteoliposomes and suggests MmpL3 in both orientations is functional after reconstitution into proteoliposomes.

Since **AcTre67** is expected to intercalate only into the outer leaflet phospholipid bilayer of the proteoliposomes, and its spontaneous flip-flop is expected to be very slow due to the presence of the trehalose headgroup, it is likely that the substrate stimulates the activity of the MmpL3 fraction with the substrate binding site accessible from the outer leaflet of the membrane.

The properties of the reconstituted CmpL1 differed from those of MmpL3. We found that CmpL1 proteoliposomes exhibited similar H^+ influx in both the pH 6.0 and the pH 7.0 buffers, whereas no significant proton flux could be detected in the pH 8.0 buffer (**Figure 3.6C**). This result suggested that either the majority of the CmpL1 reconstituted into the proteoliposomes is in an inside-out orientation, or that only the protein molecules in the inside-out orientation are functional. Surprisingly,

AcTre67 as well as other analogs did not stimulate the proton flux activity of CmpL1 in either of the tested buffers (**Figure 3.8C**).

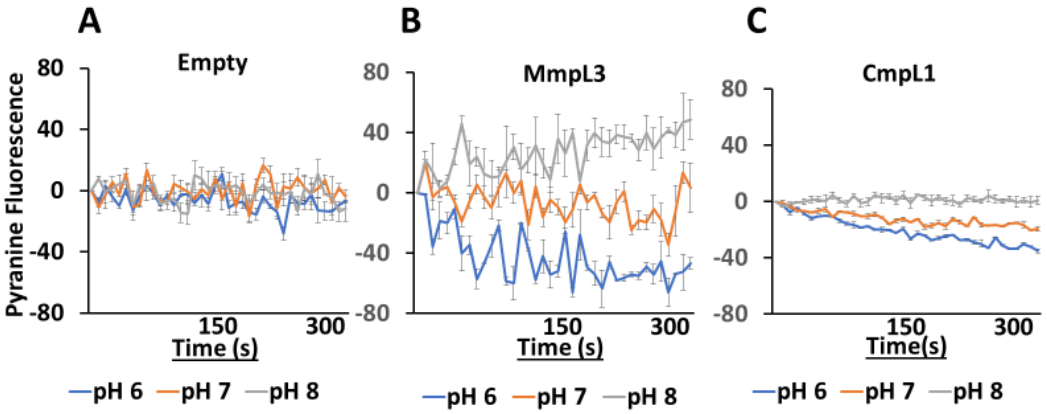

Figure 3.8 – MmpL3 and CmpL1 proton translocation activity in the presence of a substrate analog AcTre67.
This assay was carried out as detailed in **Figure 3.6**, with the exception that all vesicles were incubated with 50 nM **AcTre67** for five minutes prior to their addition to the different pH buffers. **A)** Empty control vesicles. **B)** Pyranine fluorescence of MmpL3 vesicles incubated with substrate analog. **C)** Reconstituted CmpL1 vesicles incubated with substrate analog. Grey Line: alkaline pH 8.0, Orange Line: neutral pH 7.0, Blue Line: acidic pH 6.0. Error bars are standard deviations (n = 3).

To quantify these observed results, the obtained experimental curves were fitted into a logarithmic equation, and the rates of fluorescence change per second were extracted and plotted with the standard deviation from three independent experiments. Comparing the rates of the test conditions grouped together by pH (**Figure 3.9**) we see that MmpL3 can transport H^+ without the presence of the substrate, however this activity is stimulated and increased in the presence of the substrate in both directions. CmpL1 was able to transport H^+ into the

vesicles at both acidic and neutral pH, but there was no observed stimulatory effect of the substrate addition on the H^+ transport ability. Side-by-Side comparison of the vesicles +/- substrate shows a clear stimulatory activity of **AcTre67** in MmpL3, with higher rates of transport of H^+ into and out of the proteoliposomes, while CmpL1 shows no effect of the substrate addition.

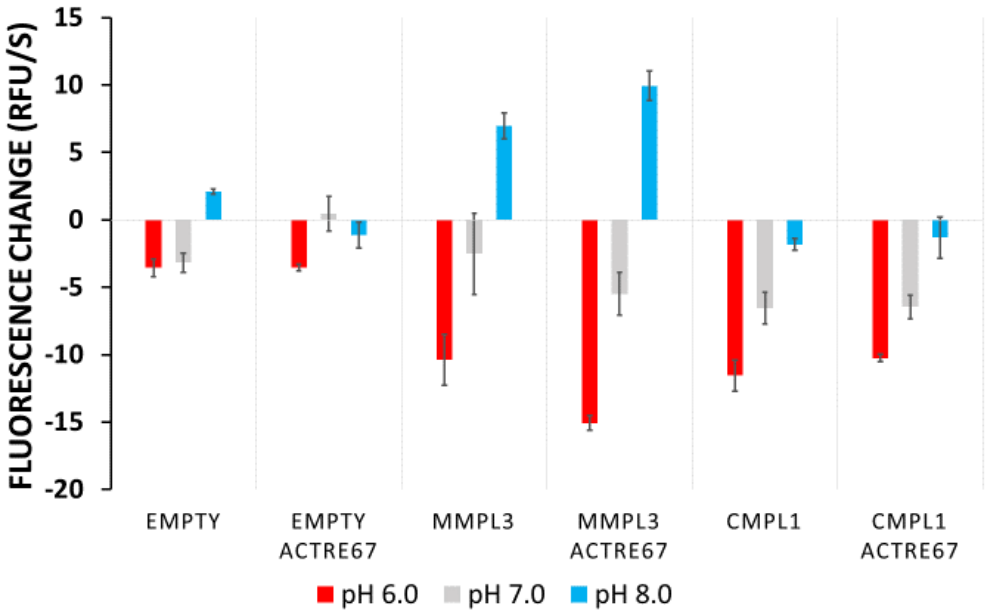

Figure 3.9 – Rates of proton transport of MmpL3 and CmpL1 in the presence of a substrate AcTre67.
Experimental data of fluorescence response as a function of time were fitted to a logarithmic equation, and the slopes were extracted as the Rate of Transport of H^+ across the lipid bilayer in RFU/second, with error bars as SD (n=3). Extravesicular buffer conditions are grouped by color- Red: acidic pH 6.0, Grey: neutral pH 7.0, and Blue: alkaline pH 8.0.

In effort to find a better functional substrate for CmpL1 than **AcTre67**, we tested the activity of a series of analogs with a similar trehalose head group but varied in acyl tail length. As CmpL1 only

exhibited H^+ flux in the acidic extravesicular buffer, we tested the activity of these substrates for activity with CmpL1 and MmpL3 in the pH 6.0 buffer as detailed above, with the results shown in **Figure 3.10**. The C16 tail of **AcTre67** had the least activity of all the substrates in CmpL1 with no significant transport activity of the intermediate length substrates (C10 / C12 / C14), however the shortest substrate C4, had a modest stimulatory effect on CmpL1 activity **(Figure 3.10A)**. MmpL3 performed with the highest activity with the C16 tail of **AcTre67**, yet showed significantly less H^+ flux with the new shorter-tailed substrates. The intermediate length substrates appear to inhibit H^+ flux through MmpL3 as the rates of transport fall well below the non-substrate treated control, with the shorter C4 substrate having no significant transport or inhibitory activity **(Figure 3.10B)**.

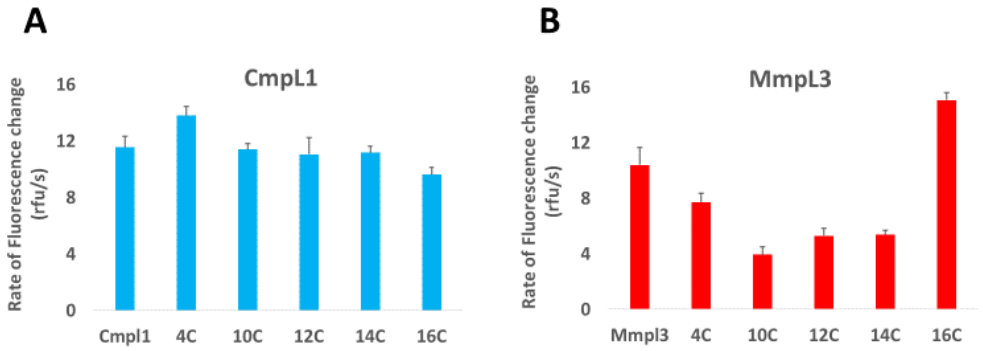

Figure 3.10 - The effect of TMM analogs on the proton transport activity of the transporters.

Proteoliposomes were incubated with a series of substrate analogs and assayed for transport activity in pH 6.0 buffer. Rates of proton transport were normalized to passive H^+ flux in untreated vesicles. **A)** CmpL1 (Blue bars) exhibited no significant effect of the intermediate or longer substrates but its transport activity was stimulated upon the addition of the shortest C4 substrate. **B)** MmpL3 (Red bars) showed significant transport activity with the C16 tailed substrate, and inhibition of H^+ flux with the intermediate length C10-14 carbon tails. Error bars are SD (n=3).

Section 3.2.4 – Interaction of AcTre67 with CmpL1 and MmpL3

Because **AcTre67** (C16) was developed as a mimic for TMM in mycobacteria, it was possible that the lack of transport activity measured with CmpL1 is due to it not being able to interact with the transporter. Therefore, in order to see whether this substrate mimic would specifically interact with the mycolic acid transporters, we utilized a Surface Plasmon Resonance (SPR) assay and tested MmpL3 and CmpL1 for specific binding with **AcTre67**.

For this assay, purified CmpL1 and MmpL3 were immobilized in separate flow cells of a CM5 Series S chip (GE Healthcare) and increasing concentrations of analyte (**AcTre67**) were injected over the chip. As anticipated, **AcTre67** does specifically interact with MmpL3 as shown in **Figure 3.11A**, and no binding activity was observed with CmpL1 in this assay **Figure 3.11B**. A possible explanation for this is the natural size discrepancy in TMM versus TMCM (trehalose mono-coryne mycolate), where the mycobacterial mycolic acid species are generally longer in both the α-branch and mero-chain as compared to the shorter mycolic acids found in corynebacterial species. This hypothesis is yet to be tested.

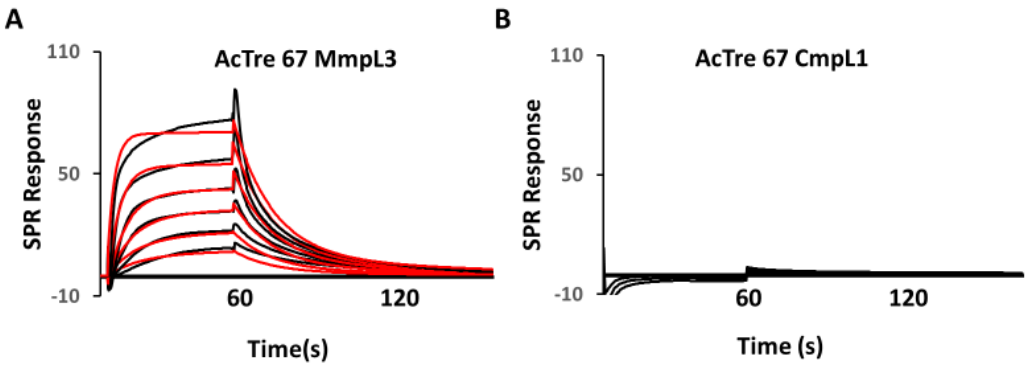

Figure 3.11 – Direct interaction of AcTre67 with MmpL3

SPR sensorgrams of the direct interaction of injected AcTre67 with MmpL3 and CmpL1 immobilized on an CM5 Series S chip. Experimental curves (black) were obtained for an AcTre67 concentration series of 400μM (top concentration) and serial two-fold diluted down to 12.5μM (bottom concentration). **A)** Curves were globally fit to a simple 1:1 binding model which yielded an experimental K_D of 6.8μM for MmpL3. **B)** No binding interaction of AcTre67 (C16) was detected with CmpL1.

Chapter 4 – Direct interaction and inhibition of mycolic acid transporters by small molecule compounds.

4.1 Introduction

With the ultimate goal to inhibit mycolic acid transport pharmaceutically in order to finally eliminate these persistent human diseases, the next major gaps in knowledge that needed to be addressed are: how to know if the compounds developed as MmpL3 inhibitors are directly interacting with their target, and what is the molecular mechanism of their action? To answer these questions, we purified MmpL3 and CmpL1 and immobilized the proteins for use in a Surface Plasmon Resonance (SPR) instrument, which allowed us to monitor specific interactions of small molecules with the protein directly. Additionally, by using transporters reconstituted into proteoliposomes, the complicating off-target effects from the whole cell are removed, and we can identify inhibitory activity specific to a compound's interaction with MmpL3. In this chapter we report our results on the development of a compound screening assay to identify potential mycolic acid transport inhibitors, and the direct binding of those inhibitory compounds to MmpL3 and CmpL1. We then describe whether transport activity of a substrate analog could be stopped by the presence of suspected MmpL3 inhibitors in a reconstituted proteoliposome. Building the ability to inhibit mycolic acid transport across the Corynebacterium-Mycobacterium-Nocardia family will help lead the development of much needed broad-spectrum anti-CMN family treatment options.

4.2 Results

4.2.1 – *In Vivo* Activity of Mycolic Acid Inhibitors against CmpL1 and MmpL3.

Previous studies showed that two of the four CmpL proteins, CmpL1 and CmpL4, are functionally redundant in the export of trehalose mono-corynemycolate (TMCM), and that only the double knockout mutant in genes encoding these proteins is non-viable[143]. We next used a panel of structurally diverse MmpL3 [126] inhibitors **(Figure 4.1)**, as well as a series of novel indole-2-carboxamide (**IC**) inhibitors, pyrrole-2-carboxamides (**PC**), and imidazole-2-carboxamides (**ImC**), to identify those with narrow and broad specificity against these transporters. For this purpose, we used *C. glutamicum* WT ATCC 13032 and triple knockout mutants LY108 (*ΔcmpL1*, *ΔcmpL2, ΔcmpL3*) and LY109 (*ΔcmpL2*, *ΔcmpL3, ΔcmpL4*) producing only CmpL4 or CmpL1, respectively.

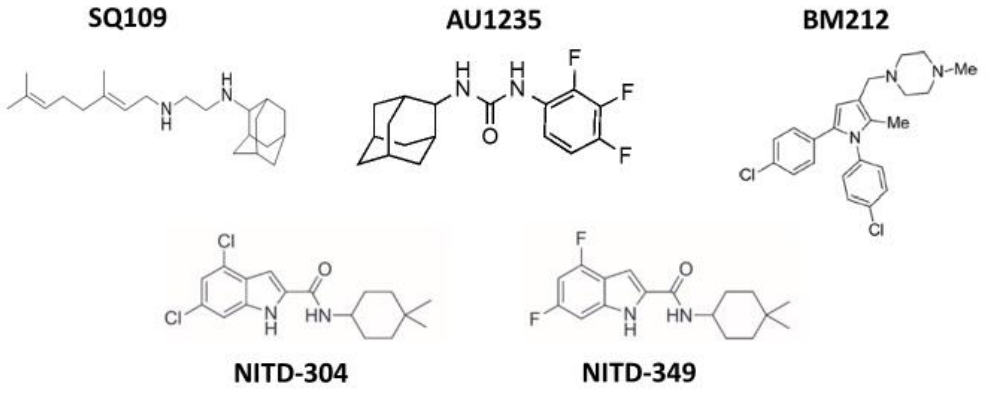

Figure 4.1 – Published MmpL3 Inhibitors

Compounds that have been pharmaceutically developed as MmpL3 inhibitors. Compounds were identified during screening for *in vitro* activity

and assigned as inhibitors of MmpL3 based on spontaneous resistance mutations mapping to MmpL3.

Minimum inhibitory concentrations (MIC) of the inhibitors were measured using a serial two-fold broth dilutions for WT *C. glutamicum* ATCC 13032, LY108 (CmpL4 dependent), LY109 (CmpL1 dependent), and *M. tuberculosis* H37Rv mc^2 (**Table 1**). **SQ109** and **BM212** compounds inhibited the growth of all tested strains, pointing to their broad, transporter-independent activity. In contrast, the tetrahydropyrazolo[1,5-a]pyrimidine-3-carboxamide **THPP-1**, as well as **NITD-304** and **NITD-349** and most of the other compounds from the **IC** series, inhibited growth of *M. tuberculosis* at low micromolar concentrations but had no activity against the *C. glutamicum* strains (MIC values over 500 μM). However, one pyrrole-2-carboxamide (**PC88**) and three representatives of the **IC** series **IC4**, **IC21** and **IC52 (Figure 4.2)** inhibited the growth of *C. glutamicum* LY109 strain at low and mid micromolar concentrations. These compounds have similar nitrogen containing backbones as inhibitors **SQ109** and **AU1235** which were observed in the crystal structure of MmpL3 occupying the inhibitor binding site. Due to the conservation of binding sites between MmpL3 and CmpL1 **(Figure 8)**, it is expected that these novel **IC** inhibitors bind to the same site in both MmpL3 and CmpL1.

Thus, in addition to *Mtb* MmpL3, these compounds specifically target CmpL1, albeit with different efficiencies. Both **IC4** and **IC21** show nanomolar MICs against H37Rv mc^2 and hence MmpL3, and are the best inhibitors of *C. glutamicum* LY109 and hence CmpL1 with MICs of 4 μM and 32 μM, respectively (**Table 4.1**). **IC52** has MIC of 32 μM against CmpL1, yet no measured inhibitory activity against *Mtb* MmpL3, whereas **PC88** is active against both at micromolar concentrations.

Taken together, these results show that the analyzed inhibitors vary in their target specificities, with most of the inhibitors effective only against

Mtb and MmpL3. **SQ109** and **BM212** have broad specificity, and in addition to MmpL3 act against both CmpL4 and CmpL1. A few are specifically active against CmpL1 and MmpL3, while only **IC52** seems to be more specific to CmpL1. Since CmpL1 and CmpL4 are interchangeable in their physiological functions, these results further suggest that the mechanism of action of these inhibitors is sensitive to the structural features of transporters.

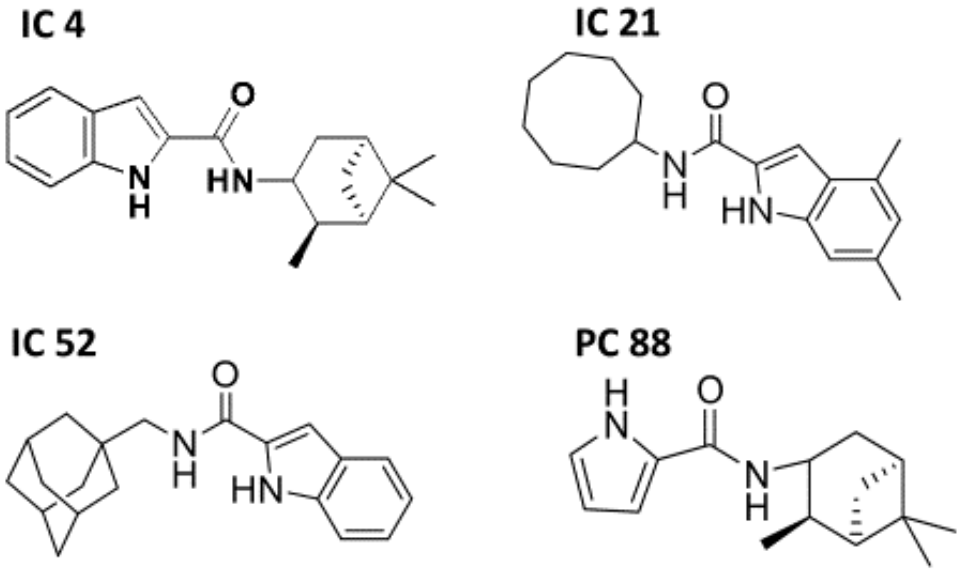

Figure 4.2 - Novel indole-2-carboxamide Inhibitors

Novel inhibitory compounds with activity against *M. tuberculosis* which were identified to have selective activity against *C. glutamicum* mutants dependent upon CmpL1 for viability. Novel **IC** and **PC** inhibitors in this thesis were generated by the North lab at Creighton University. **AU1235**, **BM212**, **SQ109**, **NITD304**, **NITD349**, and **THPP-1** were donated by the Jackson lab at Colorado State University.

Compound	*Mtb* H37Rv mc^{2}6206	*C. glutamicum* ATCC13032	*C. glutamicum* LY108	*C. glutamicum* LY109
IC2	1.02	>500	>500	>500
IC4	0.05	>500	>500	**4**
IC5	1.32	>500	>500	>500
IC10	>38.7	>500	>500	>500
IC12	19.50	>500	>500	>500
IC21	0.07	>500	>500	**31.2**
IC 41	1.09	>500	>500	>500
IC 42	> 17.45	>500	>500	>500
IC43	> 15.98	>500	>500	>500
IC46	0.48	>500	>500	>500
IC 50	0.12	>500	>500	>500
IC52	>16.21	>500	>500	**31.2**
IC65	6.17	>500	>500	>500
PC88	8.12	>500	>500	**65.2**
IC90	54.02	>500	>500	>500
PC91	32.50	250	250	250
IC92	12.34	>500	>500	>500
PC96	155.23	>500	>500	>500
SQ109	1.82	125	62.5	62.5
BM212	19.36	30	30	30
NITD304	0.01	>500	>500	>500
NITD349	0.03	>500	>500	>500
THPP-1	5.38	>500	>500	>500
AU1235	1.2	>500	>500	>500

Table 4.1. **Minimum Inhibitory Concentrations (MIC) of MmpL3 inhibitors in *M. tuberculosis* and *C. glutamicum***. Two-fold serial broth dilution assays were repeated on three independent dates, and reported values are in micromolar concentrations.

4.2.2 Direct Interaction of Inhibitors with Targets

Inhibitors acting specifically on MmpL3 and CmpL1 are expected to directly bind to the target proteins. We next used the SPR assay defined in

Chapter 2.4, to compare binding mechanisms and affinities of inhibitors with broad and narrow target specificities. We used this approach to analyze the direct interaction of several pharmaceutically pursued MmpL3 inhibitors with purified MmpL3 and purified CmpL1. For this purpose, both CmpL1 and MmpL3 proteins were purified from *C. glutamicum* LY108 carrying pAN6:CmpL1 and *M. smegmatis* mc^2 155(ΔMmpL3) carrying pMVGH1:MmpL3(tb) respectively and immobilized onto adjacent flow cells of the same CM5 Series S sensor chip (GE Healthcare). We found that the **AU1235**, **SQ109**, and **BM212** inhibitors all bound both MmpL3 and CmpL1 with micromolar affinities (**Table 4.2**). Interestingly, these inhibitors bound to CmpL1 with nearly identical binding mechanisms and affinities (**Figure 4.3**). These results are in agreement with the broad target specificities of these compounds.

Inhibitor	k_a, M^{-1} s^{-1}		k_d, s^{-1}		K_D, μM		χ^2	
	MmpL3	CmpL1	MmpL3	CmpL1	MmpL3	CmpL1	MmpL3	CmpL1
SQ109	$(1.8 \pm 0.07) \times 10^2$	$(4.9 \pm 0.03) \times 10^2$	$(6.51 \pm 0.01) \times 10^{-2}$	$(8.80 \pm 0.02) \times 10^{-2}$	362	180	6.07	28.8
AU1235	$(9.43 \pm 0.18) \times 10^2$	$(3.46 \pm 0.09) \times 10^3$	$(8.53 \pm 0.08) \times 10^{-2}$	$(4.84 \pm 0.06) \times 10^{-1}$	90.4	140	28.6	30.8
BM212	$(2.14 \pm 0.3) \times 10^3$	$(5.59 \pm 0.3) \times 10^3$	(1.3 ± 0.02)	$(3.4 \pm 0.08) \times 10^{-1}$	606	60.8	1.41	11.94
IC 21	$(6.1 \pm 0.3) \times 10^2$	$(3.12 \pm 0.11) \times 10^2$	$(8.7 \pm 0.09) \times 10^{-1}$	$(6.22 \pm 0.06) \times 10^{-1}$	1400	1900	63.6	140
IC 52	$(4.96 \pm 0.27) \times 10^2$	$(8.35 \pm 0.2) \times 10^1$	$(7.29 \pm 0.08) \times 10^{-1}$	$(7.13 \pm 0.05) \times 10^{-1}$	1400	850	119	136

IC 4	$(6.9 \pm 0.12) \times 10^{2}$	$(1.36 \pm 0.02) \times 10^{2}$	$(4.55 \pm 0.08) \times 10^{-1}$	$(4.75 \pm 0.68) \times 10^{-2}$	659	349	40.3	115

Table 4.2. Kinetic profiles of compounds interacting with MmpL3 and CmpL1. Binding data was obtained via Surface Plasmon Resonance (SPR) by sequential injection of increasing compound concentration, and sensorgrams were globally fit to a 1:1 binding model.

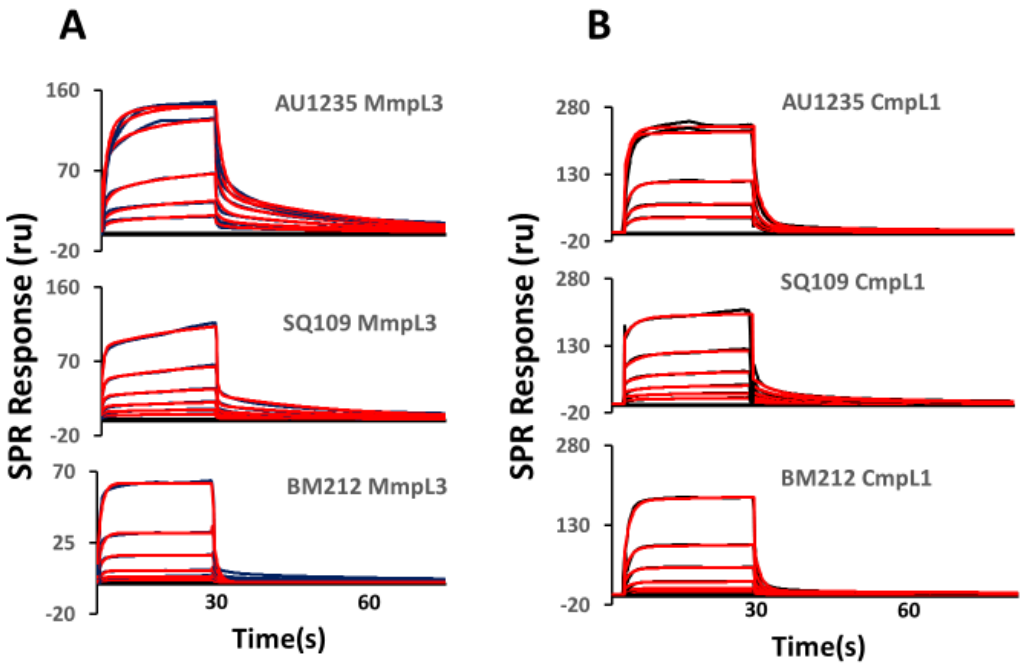

Figure 4.3 - Binding of MmpL3 inhibitors to MmpL3 and CmpL1. **A)** Binding interactions of MmpL3 inhibitors with purified MmpL3. **B)** Binding interactions of MmpL3 inhibitors with purified CmpL1. Compounds were injected at a 30 µl/min flowrate in sequentially increasing two-fold concentrations. The top concentration of **AU1235** and **SQ109** injected was 400 µM while the top concentration of **BM212** injected was 60 µM (based on max solubility at 5% DMSO experimental conditions.) Black lines are experimental data, while Red Lines are curves global fit to a 1:1 binding model. Rates and affinities can be found in **Table 4.2**.

We next analyzed binding affinities of **IC4**, **IC21**, and **IC52** with the lowest MICs against LY109 to MmpL3 and CmpL1 proteins. All three compounds bound to both transporters. For both CmpL1 and MmpL3, we again found nearly identical binding profiles for these compounds (**Figure 4.4)**. Surprisingly, **IC52** binds to both CmpL1 and MmpL3 with similar kinetics, yet MIC measurements suggested a somewhat better specificity to CmpL1. We then analyzed the interactions of transporters with the **IC52** structural analogs **IC5** and **IC46**, which are active against *Mtb* MmpL3 but have no growth inhibitory activities against *C. glutamicum* strains. We found that **IC5**, **IC52**, and **IC46** exhibit remarkably different binding activities (**Figure 4.5**). Removal of the methylene linker prior to the adamantyl group in **IC5** almost completely removes binding interaction with MmpL3. Although adding two methyl groups on the indole ring in **IC46** also negatively impacts the maximal binding response (RU) when compared to **IC52**, the compound has similar affinities to both MmpL3 and CmpL1. Thus, there is no direct correlation between binding interactions with MmpL3 and CmpL1 and growth-inhibitory activities of compounds *in vivo.*

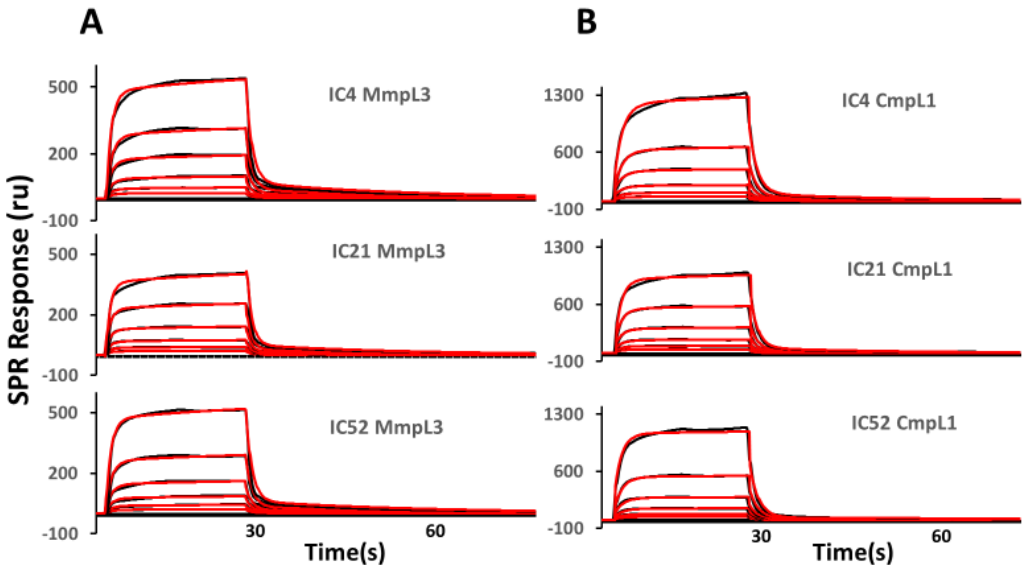

Figure 4.4 - Binding of novel IC compounds to transporters with selective *in vivo* activity against CmpL1. **A)** Binding interactions of novel **IC** inhibitors with purified MmpL3. **B)** Binding interactions of novel **IC** inhibitors with purified CmpL1. All compounds were injected at a 30 µl/min flow rate in sequentially increasing two-fold concentrations, with the top concentration injected at 400 µM for all **IC** inhibitors. Black lines are experimental data, while Red Lines are curves global fit to a 1:1 binding model. Rates and affinities can be found in **Table 4.2**.

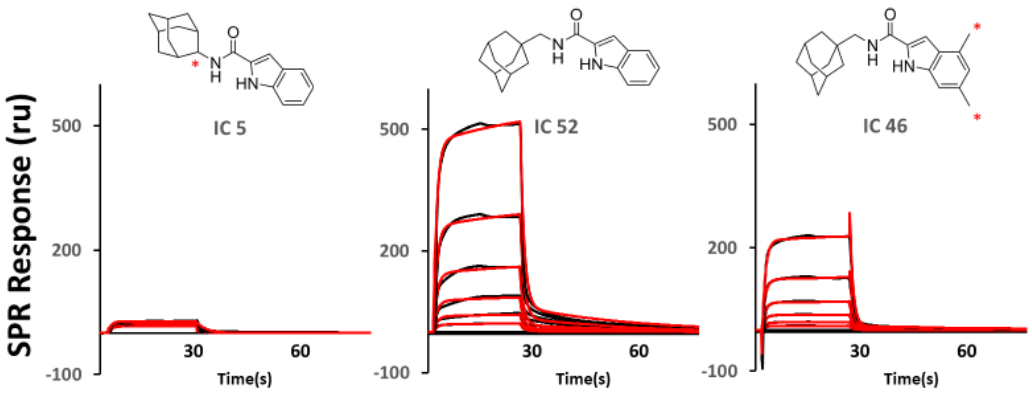

Figure 4.5 - Binding activity of structurally similar compounds to transporters.

In this assay compounds with similar chemical scaffolds were monitored for binding activity with MmpL3. Compounds were injected at a 30 µl/min flowrate in sequentially increasing twofold concentrations, from 12.5 µM to 400 µM. Black lines are experimental readings, while Red Lines are curves global fit to a 1:1 binding model.

4.2.3 - Inhibition of Proton Transport Activity

Next, we sought to test if our small molecule inhibitors which showed direct interaction with CmpL1 and MmpL3, as well as activity against both coryne- and myco- bacteria, could functionally inhibit substrate transport in CmpL1 and MmpL3. To test this hypothesis, we first incubated protein reconstituted into proteoliposomes with substrate **AcTre67**, then added them to buffers containing an inhibitor and measured the fluorescence change as described in **Chapter 3**. Control protein-free vesicles incubated with **AcTre67** and treated with the inhibitors **IC21, IC52,** and **IC4** show no significant H^+ flux in the testing conditions, therefore the MmpL3 and CmpL1 results were normalized to the control vesicles. MmpL3 experiences inhibition of H^+ movement with all three inhibitors at pH 6.0, while only showing inhibition with **IC52** at pH 8.0 and showing no inhibition at pH 8.0 with both **IC21** and **IC4 (Figure**

4.6A). CmpL1 vesicles show a slight inhibition of H^+ flux at pH 6.0 with all three inhibitors, and H^+ flux was observed out of the vesicles at pH 8.0 in the inhibitor treated vesicles. **(Figure 4.6B**)

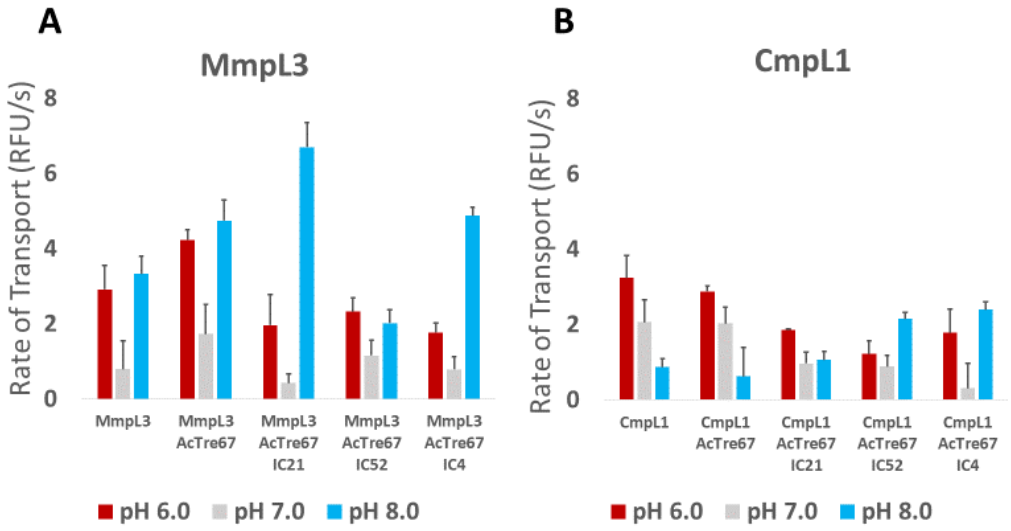

Figure 4.6 - Differential proton transport inhibition in opposite protein orientations.

A) MmpL3 vesicles incubated with **AcTre67** for five minutes then assayed for transport inhibition in different pH buffers (Red Bars – pH 6.0, Grey bars – pH 7.0, Blue bars – pH 8.0). **B)** CmpL1 vesicles treated as described in **A**. Rates of transport were obtained by fitting experimental fluorescence change over time curves to a logarithmic equation and extracting the slope. Error bars are SD (n=3).

To analyze the dose-dependency of this inhibition, we pre-incubated MmpL3- and CmpL1-containing proteoliposomes, and empty control vesicles equilibrated in the pH 7.0 buffer, with the substrate **AcTre67** and then mixed them into buffers containing increasing concentrations of inhibitor and measured the change in pyranine fluorescence and hence proton flux as described earlier. The control empty vesicles pre-incubated with **AcTre67** and then exposed to the inhibitors **IC21**, **IC52,** and **IC4** show no significant proton flux under the

testing conditions, suggesting that neither the substrate nor the inhibitors affect the integrity of the phospholipid bilayer of the vesicles (**Figure 4.7 – Black Lines**).

In contrast to the control experiment, the proton-translocating activity of MmpL3 was inhibited by all three inhibitors (**Figure 4.7 – Red Lines**). In the pH 6.0 buffer, **IC4** and **IC21** inhibited proton-translocating activity of MmpL3 in a concentration-dependent manner. Furthermore, at a concentration of 100 nM, **IC4** reduced the proton flux in MmpL3-containing proteoliposomes to the background level of the control empty vesicles. In contrast, even at the highest tested concentration of 100 nM, the rate of proton flux decreased by 4-fold in the presence of **IC21** when compared to the no inhibitor control, but it was still above the empty vesicle control. Finally, the inhibitory effect of **IC52** was the same at the three tested concentration reducing the rate of proton flux by 3-fold. This result suggests that not all MmpL3 molecules are inhibited by **IC52** under these conditions. Surprising, only **IC52** exhibited an inhibitory activity when the assays were carried out in the pH 8.0 buffer, whereas neither **IC21** nor **IC4** inhibited the reconstituted MmpL3 in the pH 8.0 buffer **(Figure 4.6A**). Furthermore, **IC21** appears to stimulate the proton efflux from the proteoliposomes. This result suggests that either the activity of inhibitors is sensitive to pH due to the presence of ionizable groups on the inhibitor backbone, or that the inhibitors have an affinity for a specific orientation of MmpL3 in the reconstituted proteoliposomes.

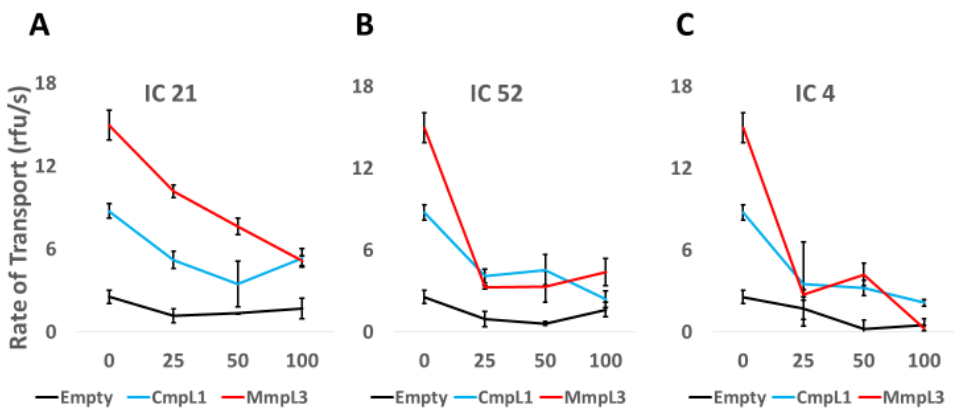

Figure 4.7 – Dose dependent inhibition of proton translocating activities of MmpL3 and CmpL1.

A) Control empty vesicles (black line), CmpL1 proteoliposomes (blue line), and MmpL3 proteoliposomes (red line) were incubated with **AcTre67** for 5 min and then added to the pH 6.0 buffer containing **IC21** at two-fold increasing concentrations. Fluorescence of entrapped pyranine was monitored for five minutes at 25^{o}C. Rates of transport were calculated and plotted as a function of inhibitor concentration. Error bars are SD (*n* = 3). **B)** The same as in **A** but buffer was supplemented with **IC52. C)** The same as in **A** but buffer was supplemented with **IC4**.

4.2.4 – Mechanism of Resistance to MmpL3 Inhibitors

A major hurdle for any antibiotic research is the emergence of resistance, and resistance to MmpL3 inhibition has, unsurprisingly, already been observed. Several spontaneous mutants exhibiting resistance to novel MmpL3 inhibitors have been clinically isolated and the mutant polymorphisms primarily localize around the transmembrane region of MmpL3 (**Figure 4.8**). A single point mutation in MmpL3 identified by the Mary Jackson group at Colorado State University, G253E has been shown to confer resistance to all the currently described MmpL3 inhibitors (**Table 4.3**), the mechanism which is of great interest.

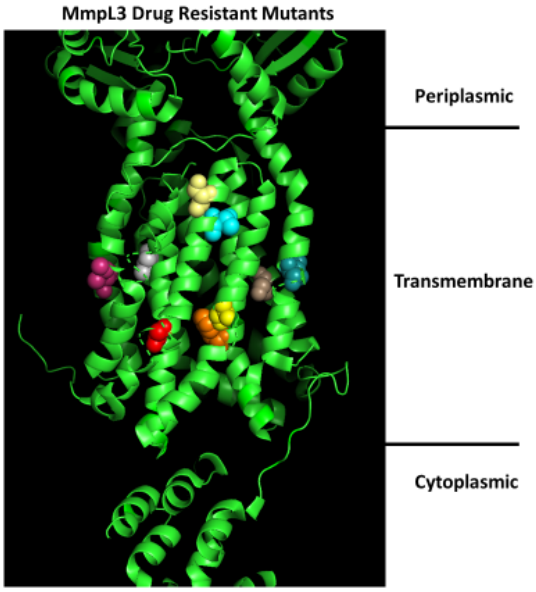

M. tuberculosis	*M. smegmatis*	Color
L189R	I194	Warm Pink
G253E	G258	Red
S288T	S293	Yellow
S309C	S314	Pale Yellow
T311I	T316	Cyan
Q372R	Q377	[Not shown]
L567R	I572	Deep Teal
S591I	S596	Wheat
F644C	F649	Orange
V684G	V689	White
V684A	V689	White

Figure 4.8 – Point mutations in MmpL3 map to the Transmembrane Region. Isolated point mutations from *M. tuberculosis* which convey resistance to MmpL3 inhibitors were aligned to the crystal structure of MmpL3 from *M. smegmatis*. Mutated residues in *Mtb* MmpL3 (left column) were aligned to their respective residues in *M. smegmatis* (center column) and represented as colored spheres on the crystal structure for M. smegmatis MmpL3, with the exception of Q372R which was located in an unresolved loop and not included in the crystal structure. All mutations occur within the α-helices that form the transmembrane spanning region of MmpL3.

Mutant	THPP1	SQ109	BM212	AU1235	NITD-304	NITD-349
L189R	8x	8x		4x	4x	4x
G253E	4x	4x		8x	8x	8x
S288T		8x	4x	8x	8x	8x
S309C	8x	8x		4x	8x	8x
T311I	4x			4x		
Q372R					8x	8x
L567R	4x	4x			8x	8x
S591I	8x	8x	4x	8x	4x	8x
F644C	8x	4x				
V684G				8x	4x	4x
V684A				4x	8x	8x

Table 4.3 – Resistance profiles of clinically isolated MmpL3 mutants. Comprising the table are MIC fold changes of the inhibitors when compared to wildtype MmpL3. Red boxes indicate an eight-fold or higher increase in MIC, Orange boxes are a four-fold or higher increase, and Grey boxes are a negligible two-fold or lower change in MIC. MmpL3 mutants and MIC data from *Mtb* strains generated by the Mary Jackson research group at Colorado State University.

To investigate how the MmpL3(G253E) singular point mutation could confer resistance to such different chemical scaffolds, we purified MmpL3(WT) and the MmpL3(G253) mutant in tandem and assayed them for compound binding. For this assay, we immobilized proteins on AR2G biosensors for use in biolayer interferometry (BLI). MmpL3(WT) yielded binding interactions with inhibitors **IC4**, **IC21**, and **SQ109** under BLI conditions, which was in agreement with our SPR results for the same inhibitors **(Figure 4.9A - Left)**. The G253E mutant exhibited an impaired binding interaction with **IC4** inhibitor, and no measurable interaction with inhibitors **IC21** and **SQ109 (Figure 4.9A - Right)**. There were no measurable differences in binding with any of the other tested inhibitors, which indicated that the G253E substitution somehow selectively interferes with the inhibition interaction of MmpL3.

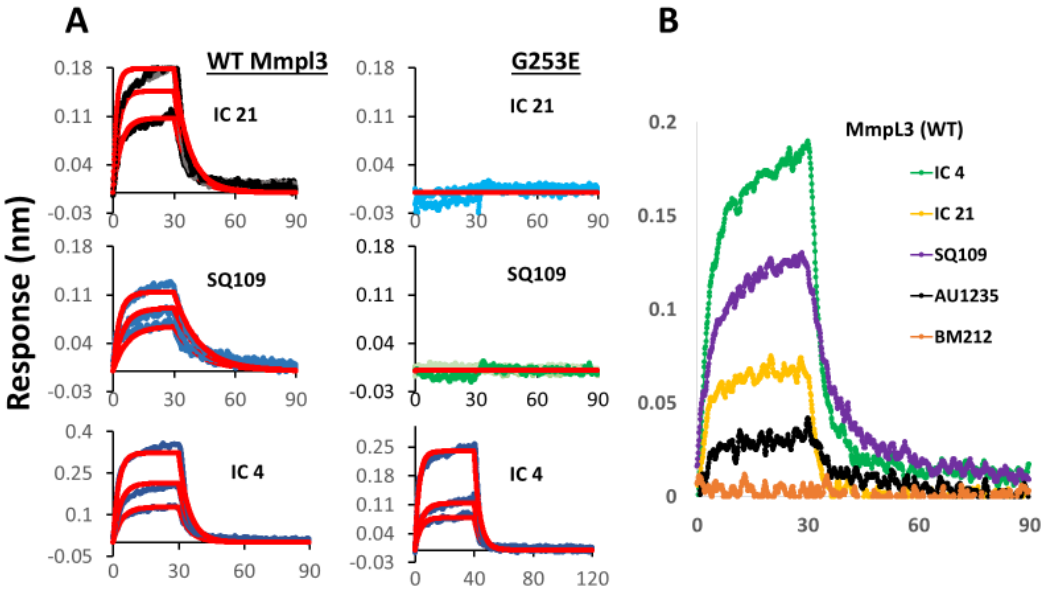

Figure 4.9 – Biolayer Interferometry sensorgrams of inhibitor interaction with MmpL3(WT) and (G253E) resistant mutants.

A) Inhibitor binding comparison of WT MmpL3 (**Left**) with resistant G253E mutant (**Right**). Compounds were tested at 50/100/200µM concentrations (black, blue and green lines) and were fit to a 1:1 binding model (red lines). **B)** Normalized BLI response for inhibitors interacting with WT MmpL3, all inhibitors tested at 200µM with the exception of BM212 which was assayed at 60 µM (the maximum solubility at the 5% DMSO test conditions.)

4.2.5 – Conformational Change in MmpL3(G253E)

Our data in **Figure 4.9** showed that the G253E mutation either abolished or impaired interaction with several different inhibitors but did not reveal an obvious mechanism as to how. We had already observed **(Figure 4.3 & Figure 4.4)** that the maximal response for many of the inhibitors obtained from SPR was of a higher magnitude than could be explained by the mass of the inhibitor interacting with the protein alone.

The maximal response from SPR is directly proportional to the amount of immobilized protein (Ligand) and the mass ratio of analyte and ligand[153,154]. Therefore, in order to generate signals of the larger R_{max} we observed, either many molecules of inhibitor would need to bind to each protein (Binding Valency >1), or more likely, upon inhibitor binding the protein undergoes a conformation change which in turn generates our higher R_{max} we observed.

To test our conformational change hypothesis, we performed a partial proteolysis of both MmpL3(WT) and MmpL3(G253E). In this assay, we exposed purified protein to an increasing concentration of trypsin in the presence or absence of excess inhibitor compounds **(Figure 4.10)**. Resolving the proteolytic pattern through SDS-PAGE and silver-staining revealed a fragmentation pattern that was mostly similar for both WT and G253E, except that the G253E mutant accumulated additional bands at 90 kDa and 75 kDa which were not present in the WT protein. This result strongly supported our hypothesis that the G253E mutation conveys resistance to MmpL3 inhibitors through an alternative stable conformation. We did not observe any effect due to the addition of excess inhibitor, however this could be explained by the fast on and off rates measured through both BLI and SPR. Conformational change due to inhibitor binding would be very short-lived, making it difficult to capture enough of the induced conformer to proteolytically digest in the limited experimental time window.

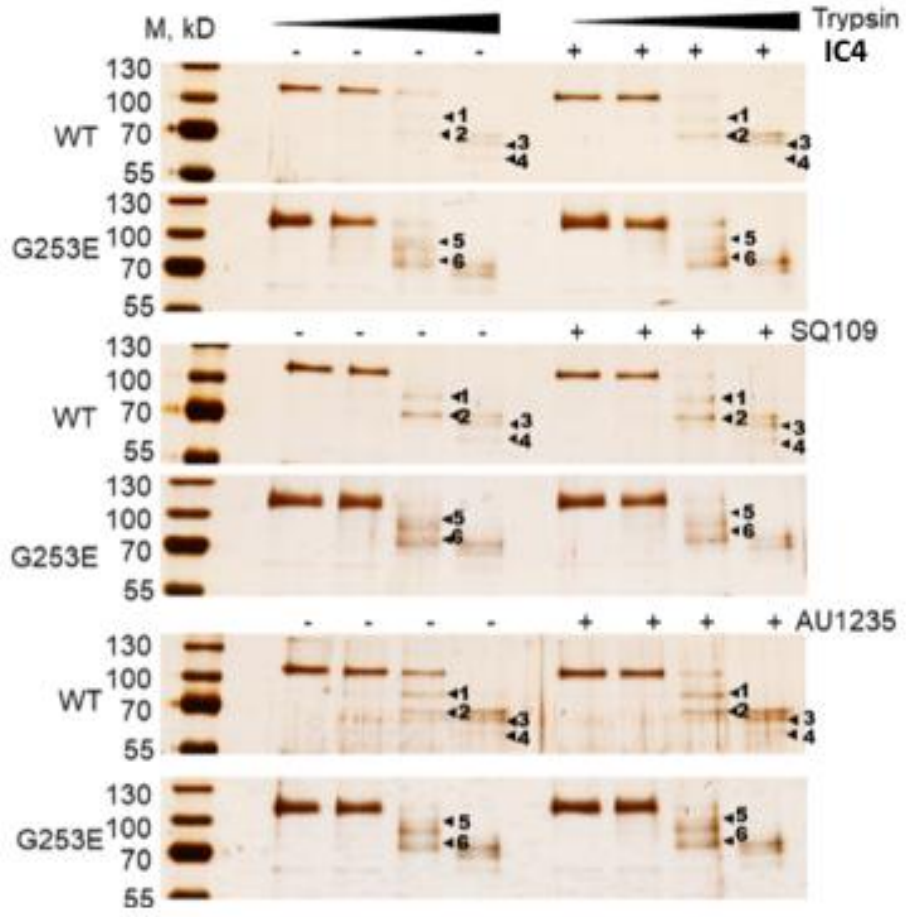

Figure 4.10 – Proteolytic Profiles of MmpL3 (WT) and (G253E). Present in the figure are the proteolytic profiles of WT MmpL3 and MmpL3(G253E) in the absence and presence of three inhibitors: **IC4** (Top pair), **SQ109** (Middle Pair), and **AU1235** (Bottom Pair). Protein concentration was standardized to 100nM for all experiments, (-) indicates no inhibitor DMSO control, (+) indicates the incubation of excess inhibitor (200μM). After incubation a ten-fold trypsin gradient was added. Figures are 12% SDS-PAGE separations visualized by silver-stain. WT MmpL3 accumulated 4 distinct proteolytic fragments: 78 kDa (1), 69 kDa (2), 65 kDa (3), and 59 kDa (4). MmpL3(G253E) also produces bands 2-4, but importantly contains 90 kDa (5) and a 75 kDa (6) band strongly suggesting an alternative stable conformation of MmpL3 imparted by this mutation. Tryptic fragment molecular sizes were calculated in ImageJ.

Chapter 5 – Participating partners, an initial exploration of the MmpL3 Interactome.

5.1 - Introduction

Bacterial cell division is an essential and highly regulated process [155,156], which requires the duplication of the entire bacterial genome and its proper localization into each of the identical daughter cells. As the cells begin to divide, new membranes need to be properly synthesized and incorporated at the dividing septa. In the CMN family there is an absolute reliance on mycolic acids being properly incorporated to form the protective outer membrane[157]. We hypothesized that mycolic acid export and incorporation into the cell wall would proceed as a function of multiple interacting enzymes around MmpL3, forming an 'MmpL3 Interactome'. To test this hypothesis, a way to identify potential protein interactions with MmpL3 was needed. The Mary Jackson group at Colorado State University used the bacterial adenylate cyclase two-hybrid (BACTH) system to identify protein-protein interactions, both in solution and with integral membrane proteins. This system takes advantage of the adenylate cyclase from *Bordetella pertussis* which consists of two fragments (T18 and T25) which do not function when spatially separated, however when fused to proteins which interact the close proximity induces the formation of cAMP. The presence of cAMP can then activate a β-galactosidase reporter which allows for simple identification of interacting partners[158-160].

For this purpose, *M. tuberculosis* MmpL3 was fused at either the N-terminal or C-terminus with either the T18 or T25 fragment, generating the MmpL3 'baits'. These bait were then screened against the *Mtb* Gateway Clone Set (BEI) for interaction with every open reading-frame in the *Mtb* genome, resulting in 19 hits showing interaction with MmpL3[161]. Of these identified hits, we selected proteins which covered diverse cellular functions to further purify and assess for direct interaction via SPR.

Among these proteins, CrgA interacts with FtsZ and is involved in mycobacterial cell division[162] and LprC is an unessential lipoprotein of unknown function[163]. Rv0207c was identified initially as part of a heme-acquisition gene cluster[164] whose specific function is unknown, however Rv0207c was of interest as it is adjacent to MmpL3 on the *Mtb* genome. MviN is a lipid II flippase involved in peptidoglycan synthesis[165], and AftD is an arabinosyltransferase involved in the polymerization of arabinogalactan[166,167]. Both MviN and AftD carry out essential roles in forming components of the CMN family cell wall core. Neither Pks13 nor Ag85 reported as a hit in the BACTH assay, yet they were still further pursued due to the essential roles they play in the formation of mycolic acids and their integration into the mycomembrane, respectively.

This chapter reports the results of the recombinant expression and purification of CrgA, pks13, LprC, Rv0207c, and MviN from *E. coli*. The purified proteins along with the secreted Antigen 85 complex (purchased from BEI) and AftD (provided by Marcia group) were analyzed for the binding interactions with MmpL3 using SPR. As mycolic acid synthesis is a highly conserved process it logically follows that mycolic acid incorporation should also be an essential conserved process, and therefore our initial exploration of the MmpL3 interactome could be used to identify more potential therapeutic targets across the CMN family.

5.2 – Results

5.2.1 - Purification of suspected interacting partners

The proteins identified in **Table 5.1** were chosen for individual purification based on the BACTH results for their eventual use in SPR binding experiments. While pks13 was not identified as a possible interactor in that assay, its essential role in the formation of mycolic acids made it of interest for interaction studies with MmpL3.

Protein	MW (kDa)	pI	Function
CrgA	11.4	11.83	Cell division organization
pks13	186	4.83	Condensase of mycolic acid
LprC	32.9	6.5	unknown
Rv0207c	26.2	4.47	unknown
MviN	143.5	7.5	Lipid II flippase

Table 5.1 – Proteins purified for assessment of interaction with MmpL3.
All were found to be membrane associated or integral membrane proteins.

Owing to the diverse physical properties of each of these targets, one singular strategy was not sufficient to accomplish the purification of all five proteins. Recombinant expression of targets was confirmed for all proteins in *Escherichia coli*; CrgA, Pks13, and Rv0207c were purified from *E. coli* Rosetta (BL21) harboring pET29a:*crgA*, pET26b:*pks13*, and pET29a:*rv0207c* respectively, while LprC and MviN were purified from *E. coli* BL21(C43) carrying plasmid pET14b:*lprC* and pET29a:*mviN*. Complete methods are detailed in **Chapter Two**. Briefly, membrane isolation and subsequent solubilization were carried out differentially, with LprC and Rv0207c requiring additional passage through a cation-exchange resin prior to affinity purification. All protein constructs carry a C-terminal 6x Histidine affinity tag, were loaded onto a copper charged His-binding resin, washed, and eluted similarly with the purification results shown in **Figure 5.1.**

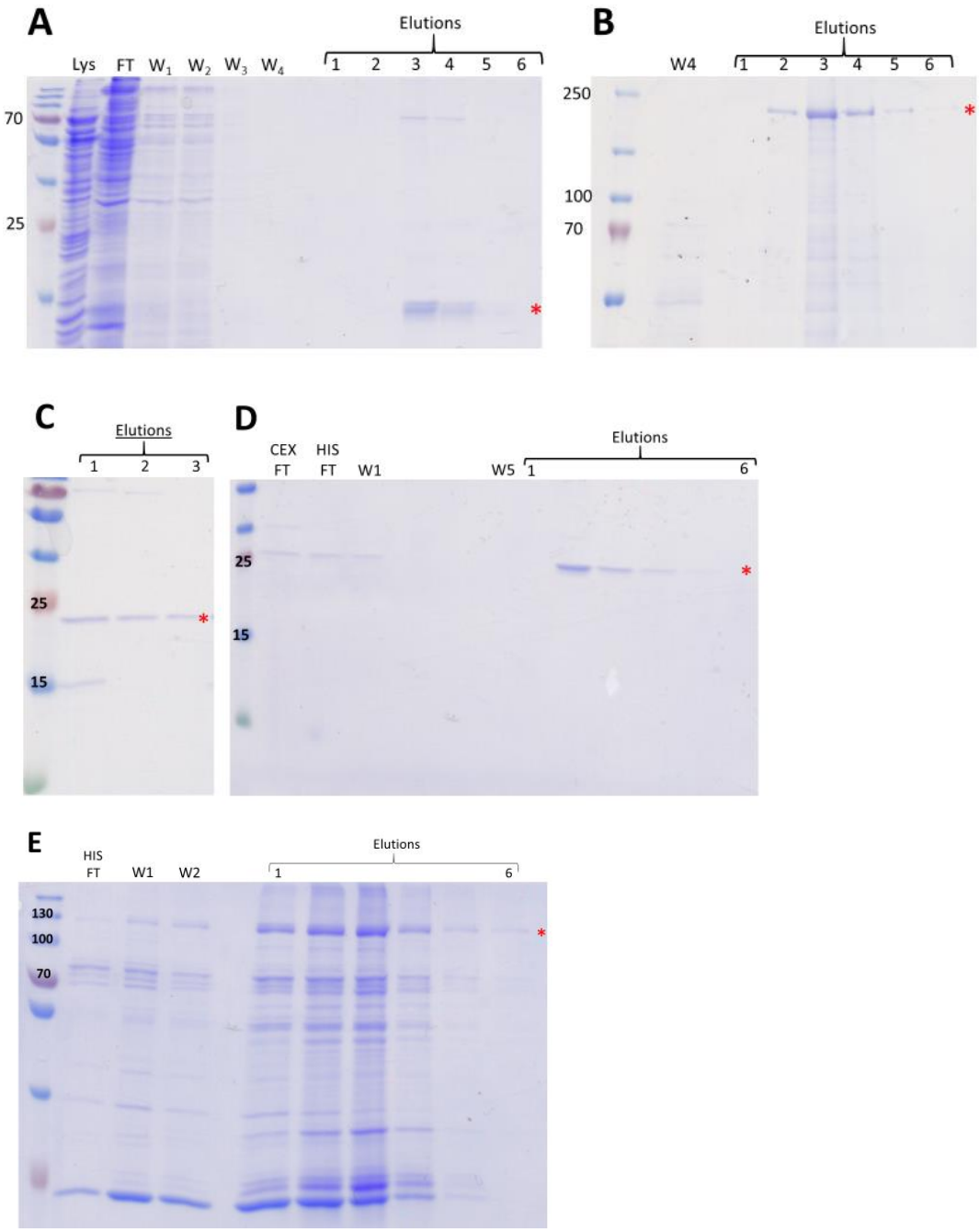

Figure 5.1 - Purification of suspected MmpL3 interactors.

A) 16% SDS-PAGE of the His affinity purified CrgA visualized by Coomassie blue. Lys: solubilized membrane fraction, FT: flow-through the His-bind column, W1-W4: 5CV 20mM imidazole wash fractions, Elutions (1-6) obtained with 400mM imidazole yielding 574 µg/ml. Purified protein indicated with Red asterisk. Indicated MW bands at 25 kDa and 70 kDa.

B) 8% SDS-PAGE of the His affinity purified Pks13 visualized by Coomassie blue. W4: Final 5CV 20mM imidazole wash fraction, Elutions (1-6) obtained with 400mM imidazole yielding 2.1 mg/ml Purified protein indicated with Red asterisk. Indicated MW bands at 25 kDa and 70 kDa. **C)** 16% SDS-PAGE of the His affinity purified LprC visualized by Coomassie blue. Elutions (1-3) obtained with 400mM imidazole yielding 1.2 mg/ml. Purified protein indicated with Red asterisk. Indicated MW bands at 15 kDa and 25 kDa. **D)** 16% SDS-PAGE of the His affinity purified Rv0207c visualized by Coomassie blue. CEX FT: flow-through from SP Sepharose cation exchange column, HIS FT: flow-through from His-bind affinity column, W1-5: 5CV wash fractions containing 20mM imidazole, Elutions (1-6) obtained with 400mM imidazole yielding 665 µg/ml. Purified protein indicated with Red asterisk. Indicated MW bands at 15 kDa and 25 kDa. **E)** 12% SDS-PAGE of the His affinity purified MviN visualized by Coomassie blue. HIS FT: flow-through of His-bind affinity column, W1-2: 5CV wash fractions containing 20mM imidazole, Elutions (1-6) obtained with 400mM yielding 1.8 mg/ml. Purified protein indicated with Red asterisk. Indicated MW bands at 70kDa, 100 kDa, and 130 kDa.

5.2.2 – Direct interaction of proteins with MmpL3

We next sought to assay binding of our purified proteins to MmpL3 using SPR. In addition to our five purified proteins, we acquired AftD which was a positive hit identified during the BACTH screening, and the antigen 85 complex. All proteins were either diluted, or centrifuge concentrated as appropriate, to achieve a 10 µM concentration and were then diluted 2-fold down to form a concentration series of injected analytes. No specific interaction with MmpL3 was detected for MviN, LprC, Pks13, or the Ag85 complex **(Figure 5.2A)**, revealing that the interaction suspected for LprC and MviN were false positives, and that Ag85 and pks13 were true negatives. Binding interactions were detected for AftD, Rv0207c, and CrgA **(Figure 5.2B)**, with similar binding affinities for AftD and Rv0207c

(172 nM and 152 nM respectively) and a higher affinity interaction for CrgA (47 nM). The binding results for CrgA, Rv0207c, and AftD were in agreement with the BACTH association hits. The confirmed interactions with CrgA and AftD associate MmpL3 with cell-division and arabinogalactan synthesis, respectively; the confirmed interaction with Rv0207c is reasonable given their adjacent genetic location, however the functional significance of this interaction remains unclear and is the subject of future research.

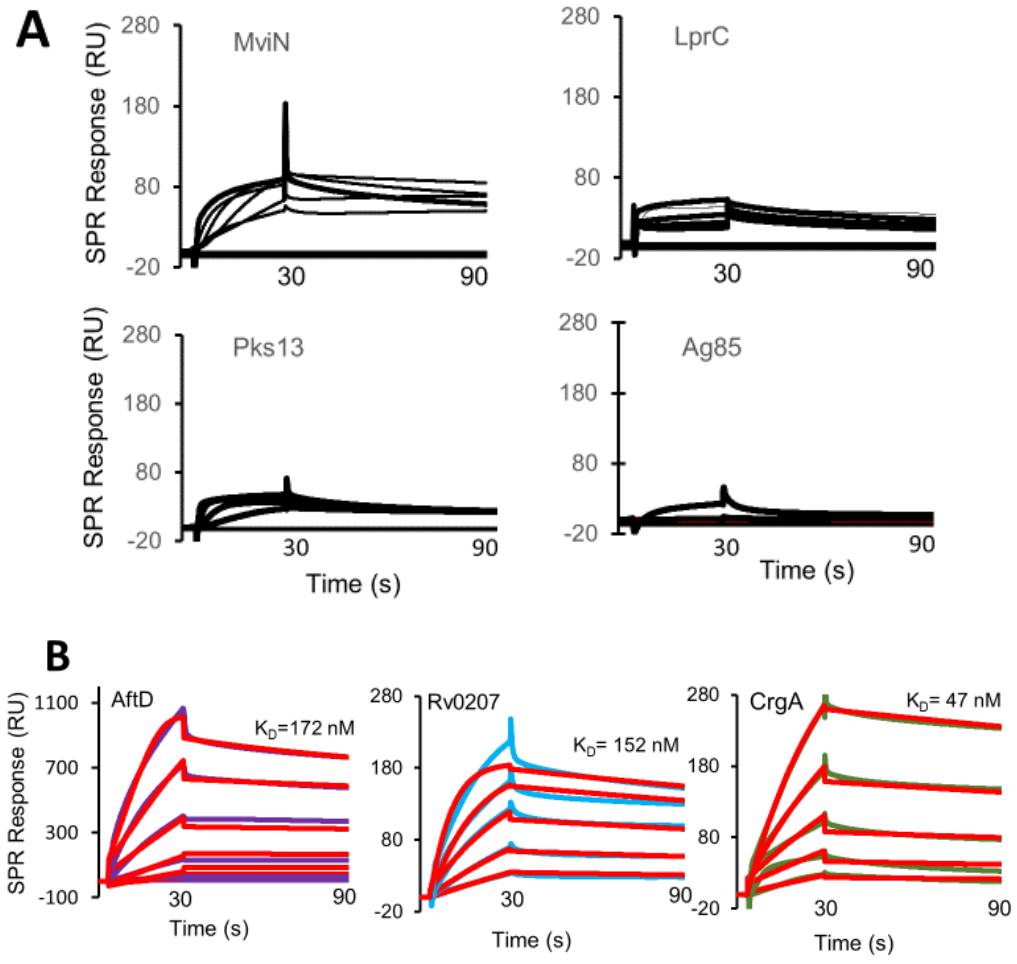

Figure 5.2 – Binding interactions of the suspected MmpL3 Interactome. All proteins were concentrated to a top concentration of 10µM and serial two-fold diluted down to 0.625µM for our injected concentration series. Proteins were injected at a 15 µl/min flow-rate and

were allowed to associate for 30 seconds, then dissassociation was measured for an additional 60 seconds. **A)** No binding interactions detected for MviN, LprC, Pks13, or the Ag85 Complex. **B)** Sensorgrams of binding partners AftD, Rv0207c, and CrgA (purple–blue–green lines, respectively) were globally fit to a 1:1 binding model (red lines). Sensorgrams for interacting proteins were global fit to a simple 1:1 binding model, and affinity constants were calculated in the mid to low nanomolar range and indicated on the plots.

Chapter 6 - Discussion

The studies partaken in this work have demonstrated a functional overlap in the mycolic acid transporters of distant relatives within the CMN family, with evidence supporting the possibility of development of broad spectrum anti-CMN family drugs. As the mycolic acid synthesis and processing pathway is highly conserved in this family, targeting not only the synthesis of mycolic acids but also their essential transport out of the cell, will allow for a more effective and broader spectrum treatment. As *C. glutamicum* CmpL1 is a functional homolog of *M. tuberculosis* MmpL3, we gained mechanistic understanding in the interaction of these transporters with various novel inhibitors and substrates using a combined approach of surface plasmon resonance and biochemical reconstitution.

The biochemical reconstitution of MmpL3 and CmpL1 into proteoliposomes provided the first insight into the mechanistic action of mycolic acid transport, confirming that the function is dependent upon H^+ translocation. It was observed in the crystal structure published of MmpL3[141] that there were molecules of a detergent bound in a hydrophobic pocket which could potentially function as an exit site during mycolic acid efflux/flipping. To begin exploring potential substrate binding activities of MmpL3, we attempted to mimic the native substrate Trehalose Mono-Mycolate (TMM) with compound **AcTre67**, which possesses a palmitic acid esterified to a trehalose head group. To test whether the length of the fatty tail was involved in substrate recognition, we assayed a series of analogous substrate mimics with shorter hydrophobic tails, and we observed a trend of improving CmpL1 substrate transport activity with the shorter tailed molecules. With MmpL3 the smaller substrate analogs all exhibit worse transport than the longer **AcTre67** compound, which suggests that there is a preferred acyl tail length for the different transporters. However, recognition of substrate by mycolic acid transporters is likely based off a different mechanism than simply the size of the attached lipid, otherwise we would expect the smaller acyl tails to

function similarly to the longer substrates. While **AcTre67** was chosen as a substrate analog for TMM due to the similar chemical structure to the 6-DDTre detergent observed in the published crystallized structure of MmpL3 from *M. smegmatis*[141], it is not an exact replacement as it is lacking the mycolic motif which is unique and formed in the natural substrate during the condensation of the alpha and mero-chain fatty acids, as well as the acetylation on this mycolic motif which seems essential for *in vivo* transport recognition[104]. Further mechanistic activity studies with substrates that more closely mimic this mycolic motif are needed.

Novel indole-2-carboxamide (**IC**) compounds designed as MmpL3 inhibitors and possessing potent anti-tubercular properties were shown to have selective activity against *C. glutamicum* strains dependent upon CmpL1 for viability. This result not only allows the early elimination of compounds that demonstrate activity in *M. tuberculosis* through off-target or non-specific effects, but also establishes a framework for the development of compounds which can selectively target members across the CMN family. We were able to demonstrate, via SPR, the effects of minor changes to chemical scaffolds which impede the interaction of compound with the targets, which suggests a discrete structural vulnerability in the homologous transporters. **IC5**, **IC46**, and **IC52** all demonstrate good activity *in vivo* against *M. tuberculosis* with low μM MIC's and based only on this inhibitory activity, would indicate that **IC52** is the least potent. However, based on the SPR binding data we collected, the modifications present on **IC5** and **IC46** seem to enhance an unknown off-target inhibitory effect. Finally, by comparing the *M. tuberculosis* MmpL3 activity data to *C. glutamicum* CmpL1, we can quickly eliminate the off target compounds and can isolate those that perform their activity solely through the inhibition of CmpL1, and by proxy, MmpL3.

The data reported in this dissertation have shown that mycolic acid transport inhibitors do directly interact with the transporters. It had been previously known that after inhibitor incubation, labeled mycolic acids build

up in the inner leaflet of the cytoplasmic membrane[109]. Through our published results[126] we now understand that the inhibitors prevent H^+ translocation necessary for lipid transport by directly interacting with the transporters and blocking the H^+ antiport pathway. The reconstitution of these transporters themselves yielded some mechanistic insight into how the inhibitors preform their function, as early in the reconstitution process the lipid-detergent-protein mixture is diluted below the CMC of detergent which causes the protein to be stabilized in a lipid bilayer, and the bilayer itself forms into vesicle. Vesicle formation is a spontaneous process, and the eventual proteoliposomes can form in two opposite orientations: with the periplasmic protein loops extending either into or outside the vesicles. When this happens, we would expect a H^+ antiport mechanism to demonstrate the ability to pump H^+ into or out of vesicles depending on which direction the concentration gradient was directed, which is what we directly observed with MmpL3. At pH 6.0 we observe H^+ flux into the vesicle which would describe the expected wildtype orientation of the protein with the periplasmic loops extending away from the vesicle, and when treated with inhibitors this transport is impaired with **IC21**, **IC52**, and **IC4**. However, at pH 8.0 we observe H^+ flux out of the vesicle which describes the opposite orientation of the protein, and when treated with inhibitors in similar fashion revealed different activity patterns. **IC21** and **IC4** no longer inhibit transport in this orientation, while **IC52** demonstrates an unchanged inhibitory activity. This result suggests that **IC52** can access its binding site more readily from either side of the membrane; whereas there is a preferred MmpL3 orientation for binding access for both **IC4** and **IC21**, specifically when the compounds are finding their target site when approaching the protein from the periplasmic face.

A well-documented aspect of bacterial cell wall synthesis is the coordinated activity of multiple enzymes working in concert. As mycolic acids are such an essential building block of the mycobacterial cell wall, and these large hydrophobic lipids must traverse the periplasm to their site

of incorporation, we hypothesized that there must be other proteins interacting with MmpL3 for mycolic acid transport. A genome wide screen for interacting proteins revealed surprisingly few hits among the known enzymes involved in mycolic acid biosynthesis, instead yielding a few proteins involved in varying aspects of cell wall synthesis or lipid metabolism. We discovered a high affinity interaction with AftD, an essential integral membrane protein which functions as an arabinosyltransferase for the biogenesis of lipoarabinomannan and the arabinogalactan matrix. We also uncovered similarly high affinity interactions with CrgA, a small membrane protein involved in the recruitment or stability of the bacterial divisome, and Rv0207c which has no known function but is located immediately downstream to MmpL3 on the *Mtb* genome. We published our results on these protein-MmpL3 interactions[161], which will hopefully lead to more therapeutic targets located at the newly described interacting interfaces.

Our studies also demonstrate a lack of interaction with the Antigen 85 complex, which was surprising as we believed they could possibly function as mycolic acid acyl carriers, shuttling the mycolic acid from the outer leaflet of the inner membrane to its destination before catalytically transferring it to either arabinogalactan or converting it to TDM. A plausible explanation for how TMM gets to its periplasmic destination would be that TMM excretion is carried out predominately at the septa of dividing cells, where membrane is being synthesized *de novo*, and would explain why MmpL3 localizes to these positions in the membrane[126].

Despite the recent advances in understanding how mycolic acids are produced and transported in mycobacteria, there remain several unanswered questions. Whether MmpL3 functions as a homotrimer akin to an RND efflux pump of Gram-negative bacteria is an active pursuit of our research group, or if it truly carries out its activity as a monomeric lipid flippase. Another unanswered question is how MmpL3 can recognize its

substrate given the large saturated hydrophobic nature of TMM; why an acetylation signal on the TMM is necessary for export, and at what stage the acetyl group is removed from the mature TMM, as perhaps there are still unknown essential enzymes in the emerging MmpL3 interactome. Since the viability of mycobacteria largely depends on the proper spacio-temporal biogenesis of the myco-membrane, answering these outstanding questions could reveal more pharmaceutically relevant therapeutic targets and improve the prognosis of tuberculosis diagnosis in the face of increasingly emerging drug resistant TB.

References

1 Servin, J. A., Herbold, C. W., Skophammer, R. G. & Lake, J. A. Evidence Excluding the Root of the Tree of Life from the Actinobacteria. *Molecular Biology and Evolution* **25**, 1-4, doi:10.1093/molbev/msm249 (2007).

2 Schubert, K. *et al.* The Antituberculosis Drug Ethambutol Selectively Blocks Apical Growth in CMN Group Bacteria. *mBio* **8**, e02213-02216, doi:10.1128/mBio.02213-16 (2017).

3 Barka, E. A. *et al.* Taxonomy, Physiology, and Natural Products of Actinobacteria. *Microbiology and molecular biology reviews : MMBR* **80**, 1-43, doi:10.1128/MMBR.00019-15 (2015).

4 TDR. Priorities for tuberculosis research: A report of the Disease reference group report on TB, leprosy and Buruli ulcer. Report No. ISBN 978 92 4 150597 0, 74 (World Health Organization, 2013).

5 Microbe Profile: Mycobacterium tuberculosis: Humanity's deadly microbial foe. **164**, 437-439, doi:https://doi.org/10.1099/mic.0.000601 (2018).

6 Ndlovu, H. & Marakalala, M. J. Granulomas and Inflammation: Host-Directed Therapies for Tuberculosis. *Front Immunol* **7**, 434, doi:10.3389/fimmu.2016.00434 (2016).

7 Guirado, E. & Schlesinger, L. S. Modeling the Mycobacterium tuberculosis Granuloma - the Critical Battlefield in Host Immunity and Disease. *Frontiers in immunology* **4**, 98-98, doi:10.3389/fimmu.2013.00098 (2013).

8 Shukla, S. *et al.* Mycobacterium tuberculosis Lipoprotein LprG Binds Lipoarabinomannan and Determines Its Cell Envelope Localization to Control Phagolysosomal Fusion. *PLOS Pathogens* **10**, e1004471 (2014).

9 Jamwal, S. V. *et al.* Mycobacterial escape from macrophage phagosomes to the cytoplasm represents an alternate adaptation mechanism. *Scientific Reports* **6**, 23089, doi:10.1038/srep23089 (2016).

10 Queval, C. J., Brosch, R. & Simeone, R. The Macrophage: A Disputed Fortress in the Battle against Mycobacterium tuberculosis. *Frontiers in Microbiology* **8**, 2284 (2017).

11 Tak, U. *et al.* The tuberculosis necrotizing toxin is an NAD+ and NADP+ glycohydrolase with distinct enzymatic properties. *Journal of Biological Chemistry* **294**, 3024-3036 (2019).

12 Ehlers, S. & Schaible, U. The Granuloma in Tuberculosis: Dynamics of a Host–Pathogen Collusion. *Frontiers in Immunology* **3**, 411 (2013).

13 Awuh, J. A. & Flo, T. H. Molecular basis of mycobacterial survival in macrophages. *Cell Mol Life Sci* **74**, 1625-1648, doi:10.1007/s00018-016-2422-8 (2017).

14 Kiazyk, S. & Ball, T. B. Latent tuberculosis infection: An overview. *Canada communicable disease report = Releve des maladies transmissibles au Canada* **43**, 62-66, doi:10.14745/ccdr.v43i34a01 (2017).
15 Lee, S. H. Tuberculosis Infection and Latent Tuberculosis. *Tuberculosis and respiratory diseases* **79**, 201-206, doi:10.4046/trd.2016.79.4.201 (2016).
16 Singh, P. & Cole, S. T. Mycobacterium leprae: genes, pseudogenes and genetic diversity. *Future microbiology* **6**, 57-71, doi:10.2217/fmb.10.153 (2011).
17 Suzuki, K. *et al.* Current status of leprosy: Epidemiology, basic science and clinical perspectives. *The Journal of Dermatology* **39**, 121-129, doi:10.1111/j.1346-8138.2011.01370.x (2012).
18 Suzuki, K. *et al.* Infection during infancy and long incubation period of leprosy suggested in a case of a chimpanzee used for medical research. *Journal of clinical microbiology* **48**, 3432-3434, doi:10.1128/JCM.00017-10 (2010).
19 Lee, M.-R. *et al.* Mycobacterium abscessus Complex Infections in Humans. *Emerging infectious diseases* **21**, 1638-1646, doi:10.3201/2109.141634 (2015).
20 Nessar, R., Cambau, E., Reyrat, J. M., Murray, A. & Gicquel, B. Mycobacterium abscessus: a new antibiotic nightmare. *Journal of Antimicrobial Chemotherapy* **67**, 810-818, doi:10.1093/jac/dkr578 (2012).
21 Ratnatunga, C. N. *et al.* The Rise of Non-Tuberculosis Mycobacterial Lung Disease. *Frontiers in Immunology* **11**, 303 (2020).
22 Hashemi-Shahraki, A. *et al.* Genetic diversity and antimicrobial susceptibility of Nocardia species among patients with nocardiosis. *Scientific Reports* **5**, 17862, doi:10.1038/srep17862 (2015).
23 Fujikura, Y. *et al.* A case of Nocardia asteroides infection in a patient with HIV/AIDS diagnosed by endobronchial ultrasound-guided transbronchial needle aspiration (EBUS-TBNA). *Internal medicine (Tokyo, Japan)* **51**, 1413-1417, doi:10.2169/internalmedicine.51.6961 (2012).
24 Torres, H. A. *et al.* Nocardiosis in Cancer Patients. *Medicine* **81** (2002).
25 Hadfield, T. L., McEvoy, P., Polotsky, Y., Tzinserling, V. A. & Yakovlev, A. A. The Pathology of Diphtheria. *The Journal of Infectious Diseases* **181**, S116-S120, doi:10.1086/315551 (2000).
26 Rappuoli, R. & Malito, E. in *Corynebacterium diphtheriae and Related Toxigenic Species: Genomics, Pathogenicity and Applications* 225-238 (Springer Netherlands, 2014).
27 Sharma, N. C. *et al.* Diphtheria. *Nature Reviews Disease Primers* **5**, 81, doi:10.1038/s41572-019-0131-y (2019).
28 Strollo, S. E., Adjemian, J., Adjemian, M. K. & Prevots, D. R. The Burden of Pulmonary Nontuberculous Mycobacterial Disease in the United States. *Annals of the American Thoracic Society* **12**, 1458-1464, doi:10.1513/AnnalsATS.201503-173OC (2015).

29 Lange, C. *et al.* Drug-resistant tuberculosis: An update on disease burden, diagnosis and treatment. *Respirology* **23**, 656-673, doi:10.1111/resp.13304 (2018).
30 Silhavy, T. J., Kahne, D. & Walker, S. The bacterial cell envelope. *Cold Spring Harbor perspectives in biology* **2**, a000414-a000414, doi:10.1101/cshperspect.a000414 (2010).
31 Coico, R. Gram Staining. *Current Protocols in Microbiology* **00**, A.3C.1-A.3C.2, doi:10.1002/9780471729259.mca03cs00 (2006).
32 Beeby, M., Gumbart, J. C., Roux, B. & Jensen, G. J. Architecture and assembly of the Gram-positive cell wall. *Molecular microbiology* **88**, 664-672, doi:10.1111/mmi.12203 (2013).
33 Demchick, P. & Koch, A. L. The permeability of the wall fabric of Escherichia coli and Bacillus subtilis. *Journal of bacteriology* **178**, 768-773, doi:10.1128/jb.178.3.768-773.1996 (1996).
34 Koch, A. L. Length Distribution of the Peptidoglycan Chains in the Sacculus of Escherichia coli. *Journal of Theoretical Biology* **204**, 533-541, doi:https://doi.org/10.1006/jtbi.2000.2039 (2000).
35 Sauvage, E. & Terrak, M. Glycosyltransferases and Transpeptidases/Penicillin-Binding Proteins: Valuable Targets for New Antibacterials. *Antibiotics (Basel, Switzerland)* **5**, 12, doi:10.3390/antibiotics5010012 (2016).
36 Auer, G. K. & Weibel, D. B. Bacterial Cell Mechanics. *Biochemistry* **56**, 3710-3724, doi:10.1021/acs.biochem.7b00346 (2017).
37 Brown, S., Santa Maria, J. P., Jr. & Walker, S. Wall teichoic acids of gram-positive bacteria. *Annual review of microbiology* **67**, 313-336, doi:10.1146/annurev-micro-092412-155620 (2013).
38 Pasquina, L. W., Santa Maria, J. P. & Walker, S. Teichoic acid biosynthesis as an antibiotic target. *Current opinion in microbiology* **16**, 531-537, doi:10.1016/j.mib.2013.06.014 (2013).
39 Swoboda, J. G., Campbell, J., Meredith, T. C. & Walker, S. Wall teichoic acid function, biosynthesis, and inhibition. *Chembiochem : a European journal of chemical biology* **11**, 35-45, doi:10.1002/cbic.200900557 (2010).
40 Beveridge, T. J. Structures of Gram-Negative Cell Walls and Their Derived Membrane Vesicles. *Journal of Bacteriology* **181**, 4725 (1999).
41 Duong, F., Eichler, J., Price, A., Rice Leonard, M. & Wickner, W. Biogenesis of the Gram-Negative Bacterial Envelope. *Cell* **91**, 567-573, doi:10.1016/S0092-8674(00)80444-4 (1997).
42 Vergalli, J. *et al.* Porins and small-molecule translocation across the outer membrane of Gram-negative bacteria. *Nature Reviews Microbiology* **18**, 164-176, doi:10.1038/s41579-019-0294-2 (2020).
43 Galdiero, S. *et al.* Microbe-host interactions: structure and role of Gram-negative bacterial porins. *Current protein & peptide science* **13**, 843-854, doi:10.2174/138920312804871120 (2012).

44 Nikaido, H. & Takatsuka, Y. Mechanisms of RND multidrug efflux pumps. *Biochimica et biophysica acta* **1794**, 769-781, doi:10.1016/j.bbapap.2008.10.004 (2009).
45 Nikaido, H. Prevention of drug access to bacterial targets: permeability barriers and active efflux. *Science* **264**, 382, doi:10.1126/science.8153625 (1994).
46 Zgurskaya, H. I., Weeks, J. W., Ntreh, A. T., Nickels, L. M. & Wolloscheck, D. Mechanism of coupling drug transport reactions located in two different membranes. *Front Microbiol* **6**, 100, doi:10.3389/fmicb.2015.00100 (2015).
47 Blair, J. M. A. & Piddock, L. J. V. Structure, function and inhibition of RND efflux pumps in Gram-negative bacteria: an update. *Current Opinion in Microbiology* **12**, 512-519, doi:https://doi.org/10.1016/j.mib.2009.07.003 (2009).
48 Masi, M., Réfregiers, M., Pos, K. M. & Pagès, J.-M. Mechanisms of envelope permeability and antibiotic influx and efflux in Gram-negative bacteria. *Nature Microbiology* **2**, 17001, doi:10.1038/nmicrobiol.2017.1 (2017).
49 Zgurskaya, H. I., Löpez, C. A. & Gnanakaran, S. Permeability Barrier of Gram-Negative Cell Envelopes and Approaches To Bypass It. *ACS infectious diseases* **1**, 512-522, doi:10.1021/acsinfecdis.5b00097 (2015).
50 Grzegorzewicz, A. E. *et al.* Assembling of the Mycobacterium tuberculosis Cell Wall Core. *The Journal of biological chemistry* **291**, 18867-18879, doi:10.1074/jbc.M116.739227 (2016).
51 Zuber, B. *et al.* Direct visualization of the outer membrane of mycobacteria and corynebacteria in their native state. *Journal of bacteriology* **190**, 5672-5680, doi:10.1128/JB.01919-07 (2008).
52 Maitra, A. *et al.* Cell wall peptidoglycan in Mycobacterium tuberculosis: An Achilles' heel for the TB-causing pathogen. *FEMS Microbiology Reviews* **43**, 548-575, doi:10.1093/femsre/fuz016 (2019).
53 Petit, J. F., Adam, A., Wietzerbin-Falszpan, J., Lederer, E. & Ghuysen, J. M. Chemical structure of the cell wall of Mycobacterium smegmatis. I — Isolation and partial characterization of the peptidoglycan. *Biochemical and Biophysical Research Communications* **35**, 478-485, doi:https://doi.org/10.1016/0006-291X(69)90371-4 (1969).
54 Mahapatra, S., Scherman, H., Brennan, P. J. & Crick, D. C. N Glycolylation of the Nucleotide Precursors of Peptidoglycan Biosynthesis of Mycobacterium spp. Is Altered by Drug Treatment. *Journal of Bacteriology* **187**, 2341, doi:10.1128/JB.187.7.2341-2347.2005 (2005).
55 Raymond, J. B., Mahapatra, S., Crick, D. C. & Pavelka, M. S. Identification of the namH Gene, Encoding the Hydroxylase Responsible for the N-Glycolylation of the Mycobacterial Peptidoglycan. *Journal of Biological Chemistry* **280**, 326-333 (2005).

56 Wietzerbin, J. *et al.* Occurrence of D-alanyl-(D)-meso-diaminopimelic acid and meso-diaminopimelyl-meso-diaminopimelic acid interpeptide linkages in the peptidoglycan of Mycobacteria. *Biochemistry* **13**, 3471-3476, doi:10.1021/bi00714a008 (1974).
57 Glauner, B., Höltje, J. V. & Schwarz, U. The composition of the murein of Escherichia coli. *Journal of Biological Chemistry* **263**, 10088-10095 (1988).
58 Alderwick, L. J., Harrison, J., Lloyd, G. S. & Birch, H. L. The Mycobacterial Cell Wall--Peptidoglycan and Arabinogalactan. *Cold Spring Harbor perspectives in medicine* **5**, a021113-a021113, doi:10.1101/cshperspect.a021113 (2015).
59 Baumgart, M., Schubert, K., Bramkamp, M. & Frunzke, J. Impact of LytR-CpsA-Psr Proteins on Cell Wall Biosynthesis in Corynebacterium glutamicum. *Journal of bacteriology* **198**, 3045-3059, doi:10.1128/JB.00406-16 (2016).
60 Harrison, J. *et al.* Lcp1 Is a Phosphotransferase Responsible for Ligating Arabinogalactan to Peptidoglycan in Mycobacterium tuberculosis. *mBio* **7**, e00972-00916, doi:10.1128/mBio.00972-16 (2016).
61 Chiaradia, L. *et al.* Dissecting the mycobacterial cell envelope and defining the composition of the native mycomembrane. *Scientific Reports* **7**, 12807, doi:10.1038/s41598-017-12718-4 (2017).
62 Hunter, R. L., Venkataprasad, N. & Olsen, M. R. The role of trehalose dimycolate (cord factor) on morphology of virulent M. tuberculosis in vitro. *Tuberculosis (Edinb)* **86**, 349-356, doi:10.1016/j.tube.2005.08.017 (2006).
63 Backus, K. M. *et al.* The three Mycobacterium tuberculosis antigen 85 isoforms have unique substrates and activities determined by non-active site regions. *J Biol Chem* **289**, 25041-25053, doi:10.1074/jbc.M114.581579 (2014).
64 Wiker, H. G. & Harboe, M. The antigen 85 complex: a major secretion product of Mycobacterium tuberculosis. *Microbiological reviews* **56**, 648-661 (1992).
65 Bailo, R., Bhatt, A. & Ainsa, J. A. Lipid transport in Mycobacterium tuberculosis and its implications in virulence and drug development. *Biochem Pharmacol* **96**, 159-167, doi:10.1016/j.bcp.2015.05.001 (2015).
66 Kaur, D., Guerin, M. E., Skovierová, H., Brennan, P. J. & Jackson, M. Chapter 2: Biogenesis of the cell wall and other glycoconjugates of Mycobacterium tuberculosis. *Advances in applied microbiology* **69**, 23-78, doi:10.1016/S0065-2164(09)69002-X (2009).
67 Cashmore, T. J. *et al.* Identification of a Membrane Protein Required for Lipomannan Maturation and Lipoarabinomannan Synthesis in Corynebacterineae. *Journal of Biological Chemistry* **292**, 4976-4986, doi:10.1074/jbc.M116.772202 (2017).

68 Garcia-Vilanova, A., Chan, J. & Torrelles, J. B. Underestimated Manipulative Roles of Mycobacterium tuberculosis Cell Envelope Glycolipids During Infection. *Frontiers in Immunology* **10**, 2909 (2019).
69 Forrellad, M. A. *et al.* Virulence factors of the Mycobacterium tuberculosis complex. *Virulence* **4**, 3-66, doi:10.4161/viru.22329 (2013).
70 Manca, C. *et al.* Virulence of a Mycobacterium tuberculosis clinical isolate in mice is determined by failure to induce Th1 type immunity and is associated with induction of IFN-α/β. *Proceedings of the National Academy of Sciences* **98**, 5752, doi:10.1073/pnas.091096998 (2001).
71 Reed, M. B. *et al.* A glycolipid of hypervirulent tuberculosis strains that inhibits the innate immune response. *Nature* **431**, 84-87, doi:10.1038/nature02837 (2004).
72 Jankute, M. *et al.* The role of hydrophobicity in tuberculosis evolution and pathogenicity. *Scientific reports* **7**, 1315-1315, doi:10.1038/s41598-017-01501-0 (2017).
73 Cambier, C. J. *et al.* Mycobacteria manipulate macrophage recruitment through coordinated use of membrane lipids. *Nature* **505**, 218-222, doi:10.1038/nature12799 (2014).
74 Rousseau, C. *et al.* Production of phthiocerol dimycocerosates protects Mycobacterium tuberculosis from the cidal activity of reactive nitrogen intermediates produced by macrophages and modulates the early immune response to infection. *Cellular Microbiology* **6**, 277-287, doi:10.1046/j.1462-5822.2004.00368.x (2004).
75 Camacho, L. R. *et al.* Analysis of the Phthiocerol Dimycocerosate Locus ofMycobacterium tuberculosis : EVIDENCE THAT THIS LIPID IS INVOLVED IN THE CELL WALL PERMEABILITY BARRIER. *Journal of Biological Chemistry* **276**, 19845-19854 (2001).
76 Mitra, A., Speer, A., Lin, K., Ehrt, S. & Niederweis, M. PPE Surface Proteins Are Required for Heme Utilization by Mycobacterium tuberculosis. *mBio* **8**, e01720-01716, doi:10.1128/mBio.01720-16 (2017).
77 Wang, Q. *et al.* PE/PPE proteins mediate nutrient transport across the outer membrane of Mycobacterium tuberculosis. *Science* **367**, 1147, doi:10.1126/science.aav5912 (2020).
78 Danilchanka, O., Pavlenok, M. & Niederweis, M. Role of porins for uptake of antibiotics by Mycobacterium smegmatis. *Antimicrob Agents Chemother* **52**, 3127-3134, doi:10.1128/aac.00239-08 (2008).
79 Faller, M., Niederweis, M. & Schulz, G. E. The Structure of a Mycobacterial Outer-Membrane Channel. *Science* **303**, 1189, doi:10.1126/science.1094114 (2004).
80 Niederweis, M. Mycobacterial porins--new channel proteins in unique outer membranes. *Mol Microbiol* **49**, 1167-1177, doi:10.1046/j.1365-2958.2003.03662.x (2003).

81 Song, H., Sandie, R., Wang, Y., Andrade-Navarro, M. A. & Niederweis, M. Identification of outer membrane proteins of Mycobacterium tuberculosis. *Tuberculosis (Edinb)* **88**, 526-544, doi:10.1016/j.tube.2008.02.004 (2008).
82 Andersen, C., Hughes, C. & Koronakis, V. Protein export and drug efflux through bacterial channel-tunnels. *Current Opinion in Cell Biology* **13**, 412-416, doi:https://doi.org/10.1016/S0955-0674(00)00229-5 (2001).
83 Zgurskaya, H. I., Krishnamoorthy, G., Ntreh, A. & Lu, S. Mechanism and Function of the Outer Membrane Channel TolC in Multidrug Resistance and Physiology of Enterobacteria. *Frontiers in microbiology* **2**, 189-189, doi:10.3389/fmicb.2011.00189 (2011).
84 Bonhivers, M. *et al.* FhuA, an Escherichia coli outer membrane protein with a dual function of transporter and channel which mediates the transport of phage DNA. *Biochimie* **80**, 363-369, doi:https://doi.org/10.1016/S0300-9084(00)80004-8 (1998).
85 Bonhivers, M. *et al.* Stability Studies of FhuA, a Two-Domain Outer Membrane Protein from Escherichia coli. *Biochemistry* **40**, 2606-2613, doi:10.1021/bi001725i (2001).
86 Krishnamoorthy, G. *et al.* Breaking the Permeability Barrier of Escherichia coli by Controlled Hyperporination of the Outer Membrane. *Antimicrobial Agents and Chemotherapy* **60**, 7372, doi:10.1128/AAC.01882-16 (2016).
87 Senaratne, R. H. *et al.* Expression of a gene for a porin-like protein of the OmpA family from Mycobacterium tuberculosis H37Rv. *Journal of bacteriology* **180**, 3541-3547 (1998).
88 Marrakchi, H., Laneelle, M. A. & Daffe, M. Mycolic acids: structures, biosynthesis, and beyond. *Chem Biol* **21**, 67-85, doi:10.1016/j.chembiol.2013.11.011 (2014).
89 Nataraj, V. *et al.* Mycolic acids: deciphering and targeting the Achilles' heel of the tubercle bacillus. *Mol Microbiol* **98**, 7-16, doi:10.1111/mmi.13101 (2015).
90 Elad, N. *et al.* Structure of Type-I Mycobacterium tuberculosis fatty acid synthase at 3.3 Å resolution. *Nature Communications* **9**, 3886, doi:10.1038/s41467-018-06440-6 (2018).
91 Holton, S. J., King-Scott, S., Eddine, A. N., Kaufmann, S. H. E. & Wilmanns, M. Structural diversity in the six-fold redundant set of acyl-CoA carboxyltransferases in Mycobacterium tuberculosis. *FEBS Letters* **580**, 6898-6902, doi:https://doi.org/10.1016/j.febslet.2006.11.054 (2006).
92 Wong, H. C., Liu, G., Zhang, Y. M., Rock, C. O. & Zheng, J. The solution structure of acyl carrier protein from Mycobacterium tuberculosis. *J Biol Chem* **277**, 15874-15880, doi:10.1074/jbc.M112300200 (2002).
93 Zimhony, O. *et al.* AcpM, the meromycolate extension acyl carrier protein of Mycobacterium tuberculosis, is activated by the 4'-

phosphopantetheinyl transferase PptT, a potential target of the multistep mycolic acid biosynthesis. *Biochemistry* **54**, 2360-2371, doi:10.1021/bi501444e (2015).

94 Veyron-Churlet, R., Guerrini, O., Mourey, L., Daffé, M. & Zerbib, D. Protein–protein interactions within the Fatty Acid Synthase-II system of Mycobacterium tuberculosis are essential for mycobacterial viability. *Molecular Microbiology* **54**, 1161-1172, doi:10.1111/j.1365-2958.2004.04334.x (2004).

95 Veyron-Churlet, R. *et al.* The Biosynthesis of Mycolic Acids in Mycobacterium tuberculosis Relies on Multiple Specialized Elongation Complexes Interconnected by Specific Protein–Protein Interactions. *Journal of Molecular Biology* **353**, 847-858, doi:https://doi.org/10.1016/j.jmb.2005.09.016 (2005).

96 Cantaloube, S., Veyron-Churlet, R., Haddache, N., Daffe, M. & Zerbib, D. The Mycobacterium tuberculosis FAS-II dehydratases and methyltransferases define the specificity of the mycolic acid elongation complexes. *PLoS One* **6**, e29564, doi:10.1371/journal.pone.0029564 (2011).

97 Lefebvre, C. *et al.* HadD, a novel fatty acid synthase type II protein, is essential for alpha- and epoxy-mycolic acid biosynthesis and mycobacterial fitness. *Scientific Reports* **8**, 6034, doi:10.1038/s41598-018-24380-5 (2018).

98 Kuhn, M. L. *et al.* Structure of the Essential Mtb FadD32 Enzyme: A Promising Drug Target for Treating Tuberculosis. *ACS infectious diseases* **2**, 579-591, doi:10.1021/acsinfecdis.6b00082 (2016).

99 Portevin, D. *et al.* A polyketide synthase catalyzes the last condensation step of mycolic acid biosynthesis in mycobacteria and related organisms. *Proc Natl Acad Sci U S A* **101**, 314-319, doi:10.1073/pnas.0305439101 (2004).

100 Gavalda, S. *et al.* The polyketide synthase Pks13 catalyzes a novel mechanism of lipid transfer in mycobacteria. *Chem Biol* **21**, 1660-1669, doi:10.1016/j.chembiol.2014.10.011 (2014).

101 Tzvetkov, M., Klopprogge, C., Zelder, O. & Liebl, W. Genetic dissection of trehalose biosynthesis in Corynebacterium glutamicum: inactivation of trehalose production leads to impaired growth and an altered cell wall lipid composition. *Microbiology* **149**, 1659-1673, doi:10.1099/mic.0.26205-0 (2003).

102 Bhatt, A., Brown, A. K., Singh, A., Minnikin, D. E. & Besra, G. S. Loss of a mycobacterial gene encoding a reductase leads to an altered cell wall containing beta-oxo-mycolic acid analogs and accumulation of ketones. *Chem Biol* **15**, 930-939, doi:10.1016/j.chembiol.2008.07.007 (2008).

103 Lea-Smith, D. J. *et al.* The reductase that catalyzes mycolic motif synthesis is required for efficient attachment of mycolic acids to arabinogalactan. *J Biol Chem* **282**, 11000-11008, doi:10.1074/jbc.M608686200 (2007).

104 Yamaryo-Botte, Y. *et al.* Acetylation of trehalose mycolates is required for efficient MmpL-mediated membrane transport in Corynebacterineae. *ACS Chem Biol* **10**, 734-746, doi:10.1021/cb5007689 (2015).
105 Rainczuk, A. K. *et al.* MtrP, a putative methyltransferase in Corynebacteria, is required for optimal membrane transport of trehalose mycolates. *Journal of Biological Chemistry* (2020).
106 Domenech, P., Reed, M. B. & Barry, C. E., 3rd. Contribution of the Mycobacterium tuberculosis MmpL protein family to virulence and drug resistance. *Infect Immun* **73**, 3492-3501, doi:10.1128/iai.73.6.3492-3501.2005 (2005).
107 Varela, C. *et al.* MmpL genes are associated with mycolic acid metabolism in mycobacteria and corynebacteria. *Chem Biol* **19**, 498-506, doi:10.1016/j.chembiol.2012.03.006 (2012).
108 Degiacomi, G. *et al.* Essentiality of mmpL3 and impact of its silencing on Mycobacterium tuberculosis gene expression. *Sci Rep* **7**, 43495, doi:10.1038/srep43495 (2017).
109 Xu, Z., Meshcheryakov, V. A., Poce, G. & Chng, S. S. MmpL3 is the flippase for mycolic acids in mycobacteria. *Proc Natl Acad Sci U S A* **114**, 7993-7998, doi:10.1073/pnas.1700062114 (2017).
110 Organization, W. H. in *Standard Treatment Regimens* Vol. 3 145 (2010).
111 Ford, C. B. *et al.* Mycobacterium tuberculosis mutation rate estimates from different lineages predict substantial differences in the emergence of drug-resistant tuberculosis. *Nature genetics* **45**, 784-790, doi:10.1038/ng.2656 (2013).
112 Argyrou, A., Vetting, M. W., Aladegbami, B. & Blanchard, J. S. Mycobacterium tuberculosis dihydrofolate reductase is a target for isoniazid. *Nature Structural & Molecular Biology* **13**, 408-413, doi:10.1038/nsmb1089 (2006).
113 Banerjee, A. *et al.* inhA, a gene encoding a target for isoniazid and ethionamide in Mycobacterium tuberculosis. *Science* **263**, 227, doi:10.1126/science.8284673 (1994).
114 Forbes, M., Kuck, N. A. & Peets, E. A. Mode of action of ethambutol. *Journal of bacteriology* **84**, 1099-1103 (1962).
115 Goude, R., Amin, A. G., Chatterjee, D. & Parish, T. The Arabinosyltransferase EmbC Is Inhibited by Ethambutol in Mycobacterium tuberculosis. *Antimicrobial Agents and Chemotherapy* **53**, 4138, doi:10.1128/AAC.00162-09 (2009).
116 Zhang, Y., Shi, W., Zhang, W. & Mitchison, D. Mechanisms of Pyrazinamide Action and Resistance. *Microbiology spectrum* **2**, 1-12, doi:10.1128/microbiolspec.MGM2-0023-2013 (2013).
117 Conditions that may affect the results of susceptibility testing of Mycobacterium tuberculosis to pyrazinamide. **51**, 42-49, doi:https://doi.org/10.1099/0022-1317-51-1-42 (2002).

118 Hu, Y., Coates, A. R. & Mitchison, D. A. Sterilising action of pyrazinamide in models of dormant and rifampicin-tolerant Mycobacterium tuberculosis. *The International Journal of Tuberculosis and Lung Disease* **10**, 317-322 (2006).
119 Pang, Y. *et al.* Study of the Rifampin Monoresistance Mechanism in Mycobacterium tuberculosis. *Antimicrobial Agents and Chemotherapy* **57**, 893, doi:10.1128/AAC.01024-12 (2013).
120 Wehrli, W. Rifampin: mechanisms of action and resistance.
121 Hoagland, D. T., Liu, J., Lee, R. B. & Lee, R. E. New agents for the treatment of drug-resistant Mycobacterium tuberculosis. *Adv Drug Deliv Rev* **102**, 55-72, doi:10.1016/j.addr.2016.04.026 (2016).
122 Li, W. *et al.* MmpL3 as a Target for the Treatment of Drug-Resistant Nontuberculous Mycobacterial Infections. *Frontiers in microbiology* **9**, 1547-1547, doi:10.3389/fmicb.2018.01547 (2018).
123 Li, W. *et al.* Novel insights into the mechanism of inhibition of MmpL3, a target of multiple pharmacophores in Mycobacterium tuberculosis. *Antimicrob Agents Chemother* **58**, 6413-6423, doi:10.1128/aac.03229-14 (2014).
124 Li, W. *et al.* Synergistic Interactions of MmpL3 Inhibitors with Antitubercular Compounds In Vitro. *Antimicrob Agents Chemother* **61**, doi:10.1128/aac.02399-16 (2017).
125 Li, W. *et al.* Therapeutic Potential of the Mycobacterium tuberculosis Mycolic Acid Transporter, MmpL3. *Antimicrob Agents Chemother* **60**, 5198-5207, doi:10.1128/aac.00826-16 (2016).
126 Li, W. *et al.* Direct Inhibition of MmpL3 by Novel Antitubercular Compounds. *ACS Infect Dis* **5**, 1001-1012, doi:10.1021/acsinfecdis.9b00048 (2019).
127 Franz, N. D. *et al.* Design, synthesis and evaluation of indole-2-carboxamides with pan anti-mycobacterial activity. *Bioorg Med Chem* **25**, 3746-3755, doi:10.1016/j.bmc.2017.05.015 (2017).
128 Protopopova, M. *et al.* Identification of a new antitubercular drug candidate, SQ109, from a combinatorial library of 1,2-ethylenediamines. *Journal of Antimicrobial Chemotherapy* **56**, 968-974, doi:10.1093/jac/dki319 (2005).
129 Sacksteder, K. A., Protopopova, M., Barry, C. E., 3rd, Andries, K. & Nacy, C. A. Discovery and development of SQ109: a new antitubercular drug with a novel mechanism of action. *Future microbiology* **7**, 823-837, doi:10.2217/fmb.12.56 (2012).
130 Tahlan, K. *et al.* SQ109 Targets MmpL3, a Membrane Transporter of Trehalose Monomycolate Involved in Mycolic Acid Donation to the Cell Wall Core of Mycobacterium tuberculosis. *Antimicrobial Agents and Chemotherapy* **56**, 1797, doi:10.1128/AAC.05708-11 (2012).

131 Boeree, M. J. *et al.* High-dose rifampicin, moxifloxacin, and SQ109 for treating tuberculosis: a multi-arm, multi-stage randomised controlled trial. *The Lancet Infectious Diseases* **17**, 39-49, doi:10.1016/S1473-3099(16)30274-2 (2017).
132 Grzegorzewicz, A. E. *et al.* Inhibition of mycolic acid transport across the Mycobacterium tuberculosis plasma membrane. *Nat Chem Biol* **8**, 334-341, doi:10.1038/nchembio.794 (2012).
133 Biava, M. *et al.* Antimycobacterial Agents. Novel Diarylpyrrole Derivatives of BM212 Endowed with High Activity toward Mycobacterium tuberculosis and Low Cytotoxicity. *Journal of Medicinal Chemistry* **49**, 4946-4952, doi:10.1021/jm0602662 (2006).
134 Deidda, D. *et al.* Bactericidal Activities of the Pyrrole Derivative BM212 against Multidrug-Resistant and Intramacrophagic Mycobacterium tuberculosis Strains. *Antimicrobial Agents and Chemotherapy* **42**, 3035, doi:10.1128/AAC.42.11.3035 (1998).
135 Nikaido, H. Structure and mechanism of RND-type multidrug efflux pumps. *Advances in enzymology and related areas of molecular biology* **77**, 1-60, doi:10.1002/9780470920541.ch1 (2011).
136 Murakami, S., Nakashima, R., Yamashita, E., Matsumoto, T. & Yamaguchi, A. Crystal structures of a multidrug transporter reveal a functionally rotating mechanism. *Nature* **443**, 173-179, doi:10.1038/nature05076 (2006).
137 Anes, J., McCusker, M. P., Fanning, S. & Martins, M. The ins and outs of RND efflux pumps in Escherichia coli. *Frontiers in Microbiology* **6**, 587 (2015).
138 Zhang, X. C., Liu, M. & Han, L. Energy coupling mechanisms of AcrB-like RND transporters. *Biophysics reports* **3**, 73-84, doi:10.1007/s41048-017-0042-y (2017).
139 Murakami, S., Nakashima R Fau - Yamashita, E., Yamashita E Fau - Yamaguchi, A. & Yamaguchi, A. Crystal structure of bacterial multidrug efflux transporter AcrB.
140 Takatsuka, Y. & Nikaido, H. Threonine-978 in the transmembrane segment of the multidrug efflux pump AcrB of Escherichia coli is crucial for drug transport as a probable component of the proton relay network.
141 Zhang, B. *et al.* Crystal Structures of Membrane Transporter MmpL3, an Anti-TB Drug Target. *Cell* **176**, 636-648 e613, doi:10.1016/j.cell.2019.01.003 (2019).
142 Belardinelli, J. M. *et al.* Structure-Function Profile of MmpL3, the Essential Mycolic Acid Transporter from Mycobacterium tuberculosis. *ACS Infect Dis* **2**, 702-713, doi:10.1021/acsinfecdis.6b00095 (2016).
143 Yang, L. *et al.* RND transporters protect Corynebacterium glutamicum from antibiotics by assembling the outer membrane. *Microbiologyopen* **3**, 484-496, doi:10.1002/mbo3.182 (2014).

144 Zgurskaya, H. I. & Nikaido, H. Bypassing the periplasm: reconstitution of the AcrAB multidrug efflux pump of Escherichia coli. *Proceedings of the National Academy of Sciences of the United States of America* **96**, 7190-7195, doi:10.1073/pnas.96.13.7190 (1999).
145 Picard, M. *et al.* in *Bacterial Multidrug Exporters: Methods and Protocols* 113-145 (Springer New York, 2018).
146 Rigaud, J.-L. & Lévy, D. in *Methods in Enzymology* Vol. 372 65-86 (Academic Press, 2003).
147 *Handbook of Corynebacterium glutamicum*. (CRC Press, 2005).
148 Schmidt, T. G. M. & Skerra, A. The Strep-tag system for one-step purification and high-affinity detection or capturing of proteins. *Nature Protocols* **2**, 1528-1535, doi:10.1038/nprot.2007.209 (2007).
149 Patching, S. G. Surface plasmon resonance spectroscopy for characterisation of membrane protein–ligand interactions and its potential for drug discovery. *Biochimica et Biophysica Acta (BBA) - Biomembranes* **1838**, 43-55, doi:https://doi.org/10.1016/j.bbamem.2013.04.028 (2014).
150 Lévy, D., Bluzat, A., Seigneuret, M. & Rigaud, J.-L. A systematic study of liposome and proteoliposome reconstitution involving Bio-Bead-mediated Triton X-100 removal. *Biochimica et Biophysica Acta (BBA) - Biomembranes* **1025**, 179-190, doi:https://doi.org/10.1016/0005-2736(90)90096-7 (1990).
151 Clement, N. R. & Gould, J. M. Pyranine (8-hydroxy-1,3,6-pyrenetrisulfonate) as a probe of internal aqueous hydrogen ion concentration in phospholipid vesicles. *Biochemistry* **20**, 1534-1538, doi:10.1021/bi00509a019 (1981).
152 Kano, K. & Fendler, J. H. Pyranine as a sensitive pH probe for liposome interiors and surfaces. pH gradients across phospholipid vesicles. *Biochimica et Biophysica Acta (BBA) - Biomembranes* **509**, 289-299, doi:https://doi.org/10.1016/0005-2736(78)90048-2 (1978).
153 Karlsson, R., Michaelsson, A. & Mattsson, L. Kinetic analysis of monoclonal antibody-antigen interactions with a new biosensor based analytical system. *Journal of Immunological Methods* **145**, 229-240, doi:https://doi.org/10.1016/0022-1759(91)90331-9 (1991).
154 Stenberg, E., Persson, B., Roos, H. & Urbaniczky, C. Quantitative determination of surface concentration of protein with surface plasmon resonance using radiolabeled proteins. *Journal of Colloid and Interface Science* **143**, 513-526, doi:https://doi.org/10.1016/0021-9797(91)90284-F (1991).
155 Harry, E., Monahan, L. & Thompson, L. in *International Review of Cytology* Vol. 253 27-94 (Academic Press, 2006).
156 Rothfield, L. I. & Justice, S. S. Bacterial Cell Division: The Cycle of the Ring. *Cell* **88**, 581-584, doi:10.1016/S0092-8674(00)81899-1 (1997).

157 Donovan, C. & Bramkamp, M. Cell division in Corynebacterineae. *Frontiers in microbiology* **5**, 132-132, doi:10.3389/fmicb.2014.00132 (2014).
158 Battesti, A. & Bouveret, E. The bacterial two-hybrid system based on adenylate cyclase reconstitution in Escherichia coli. *Methods* **58**, 325-334, doi:https://doi.org/10.1016/j.ymeth.2012.07.018 (2012).
159 Baulard, A. R. *et al.* In Vivo Interaction between the Polyprenol Phosphate Mannose Synthase Ppm1 and the Integral Membrane Protein Ppm2 from Mycobacterium smegmatis Revealed by a Bacterial Two-hybrid System. *Journal of Biological Chemistry* **278**, 2242-2248 (2003).
160 Karimova, G., Pidoux, J., Ullmann, A. & Ladant, D. A bacterial two-hybrid system based on a reconstituted signal transduction pathway. *Proceedings of the National Academy of Sciences* **95**, 5752, doi:10.1073/pnas.95.10.5752 (1998).
161 Belardinelli, J. M. *et al.* The MmpL3 interactome reveals a complex crosstalk between cell envelope biosynthesis and cell elongation and division in mycobacteria. *Scientific Reports* **9**, 10728, doi:10.1038/s41598-019-47159-8 (2019).
162 Das, N., Hung, I., Qin, H. & Cross, T. A. Initial Structural Studies of Mtb Membrane Protein "CrgA" in Membrane Mimetic Environment. *Biophysical Journal* **102**, 264a, doi:10.1016/j.bpj.2011.11.1455 (2012).
163 Ocampo, M., Curtidor, H., Vanegas, M., Patarroyo, M. A. & Patarroyo, M. E. Specific interaction between Mycobacterium tuberculosis lipoprotein-derived peptides and target cells inhibits mycobacterial entry in vitro. *Chem Biol Drug Des* **84**, 626-641, doi:10.1111/cbdd.12365 (2014).
164 Tullius, M. V. *et al.* Discovery and characterization of a unique mycobacterial heme acquisition system. *Proceedings of the National Academy of Sciences of the United States of America* **108**, 5051-5056, doi:10.1073/pnas.1009516108 (2011).
165 Gee, C. L. *et al.* A phosphorylated pseudokinase complex controls cell wall synthesis in mycobacteria. *Science signaling* **5**, ra7-ra7, doi:10.1126/scisignal.2002525 (2012).
166 Alderwick, L. J. *et al.* AftD functions as an α1 → 5 arabinofuranosyltransferase involved in the biosynthesis of the mycobacterial cell wall core. *Cell surface (Amsterdam, Netherlands)* **1**, 2-14, doi:10.1016/j.tcsw.2017.10.001 (2018).
167 Skovierova, H. *et al.* AftD, a novel essential arabinofuranosyltransferase from mycobacteria. *Glycobiology* **19**, 1235-1247, doi:10.1093/glycob/cwp116 (2009).